Computational stress and damage modelling for rolling contact fatigue

Cerullo, Michele

Publication date:
2014

Document Version
Publisher's PDF, also known as Version of record

Computational stress and damage modelling for rolling contact fatigue

PhD Thesis

$$(EIv'')'' = q - \rho A\ddot{v}$$

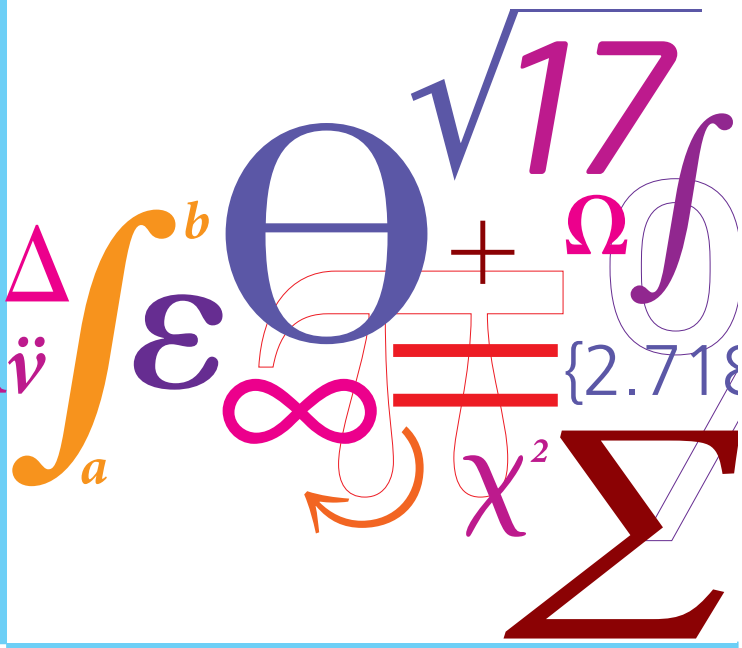

Michele Cerullo
DCAMM Special Report No. S169
September 2014

DTU Mechanical Engineering
Department of Mechanical Engineering

Computational stress and damage modelling for rolling contact fatigue

Michele Cerullo

DEPT. OF MECHANICAL ENGINEERING
Solid Mechanics
TECHNICAL UNIVERSITY OF DENMARK

Title of the thesis:
Computational stress and damage modelling for rolling contact fatigue

Ph.D. Student:
Michele Cerullo
E-mail: mcer@mek.dtu.dk

Supervisors:
Prof. Dr. Techn. Viggo Tvergaard
E-mail: viggo@mek.dtu.dk

Assoc. Prof. Christian Frithiof Niordson
E-mail: cn@mek.dtu.dk

Prof. Peder Klit
E-mail: klit@mek.dtu.dk

Address:
Department of Mechanical Engineering, Solid Mechanics
Technical University of Denmark
Nils Koppels Allé, Building 404, 2800 Kgs. Lyngby, Denmark

Preface

This thesis is submitted in partial fulfillment of the requirements for obtaining the degree of Ph.D in mechanical engineering at the Technical University of Denmark (DTU). The Ph.D project was carried out at the Department of Mechanical Engineering, Solid Mechanics, at DTU in the period 1st September 2011–30th September 2014. Supervisors on the project were Prof. Dr. Techn. Viggo Tvergaard, Associate Professor Christian Frithiof Niordson and Prof. Peder Klit.

The work is supported by the Strategic Research Center "REWIND - Knowledge based engineering for improved reliability of critical wind turbine components", Danish Research Council for Strategic Research, grant no. 10-093966.

I would like to express my gratitude to my supervisors for all their inspiring suggestions and for always been encouraging during the whole project. They always found time for discussing the results and their support was really essential for me.

I also would like to thank my PhD colleagues for all the talks and for the nice atmosphere they created at work.

A special thank goes to my colleague and friend Danial, with whom I had a lot of scientific discussions and, most of all, I shared many funny moments and smiles that made long days (and sometimes nights) in the office more enjoyable. "Mersi" my friend.

Moving to another country and coming in contact with another culture is always difficult. For this reason I would like to thank all my (B.E.S.T.) friends. Although far physically, you have always been with me, in my heart, in joyful and dark moments.

Many thanks also go to my friends from "Casa Napoli", Antonio and Andrea: it has been a pleasure sharing with you these years of fun, nice dinners and suffering TV football matches.

I would like to thank my girlfriend Claudia, who has always listened to me, encouraging and supporting me during my PhD. She is my Sun and my strength and I would have not made it without her.

Finally I would like to thank my parents for their love and for teaching me the values that stand at the basis of my life and my work. The love you gave me reflects in the passion I put in everything I do. Thank you, I really love you.

Kgs. Lyngby, September 30th 2014

Michele Cerullo

Abstrakt (In Danish)

Kontaktudmattelse i radiale rullelejer er undersøgt ved hjælp af et 2D plan tøjnings finite element-program. Dang Vans multiaksiale udmattelseskriterie er først brugt i et makroskopisk studie, der modellerer en rullebane for at undersøge området hvor udmattelsesrevner har størst sandsynlighed for at opstå. En Hertz og en elastisk-hydrodynamisk smørings trykfordeling er påført rullebanen for at modellere kontakten mellem rullen og ringen, og resultaterne er sammenlignet ud fra Dang Van-kriteriet. Effekten af hærdningsbehandling af ringoverfladen og af kompressions residualspændinger er ydermere analyseret. Spændingshistorikken i et materialepunkt ved dybden, hvor Dang Van-skadeskoefficienten er maksimal, er herefter gemt og brugt i efterfølgende mikromekanisk analyse. Spændingshistorikken er påført som periodiske randbetingelser i et repræsentativt volumenelement, der indeholder en enkelt inklusion i den bærende stål-matrix. Indvirkningen af indeslutningens volumenfraktion, materiale, og orientering er undersøgt. Udmattelsesrevnevæksten af en allerede eksisterende revne, opstået i matricen, er til sidst undersøgt for en aluminiumoxid indeslutning ved hjælp af kohæsive elementer og skademekanik. Resultater for forskellige belastningstilfælde og forskellige revneorienteringer er sammenlignet.

Abstract

Rolling contact fatigue in radial roller bearings is studied by means of a 2D plane strain finite element program. The Dang Van multiaxial fatigue criterion is firstly used, in a macroscopic study modeling the bearing raceway, to investigate the region where fatigue cracks are more likely to nucleate. A Hertzian and an elastohydrodynamic lubricated pressure distribution are applied on the bearing raceway to model the contact between the roller and the ring, and the results are compared in light of the Dang Van criterion. The beneficial effects of a hardening treatment of the ring surface and of compressive residual stresses are also analyzed. The stress history of a material point at the depth where the maximum Dang Van damage factor is reached is then recorded and used in a subsequent micro-mechanical analysis. The stress history is applied as periodic boundary conditions in a representative volume element where a single inclusion is embedded in a bearing steel matrix. The effects of different inclusion volume fractions, material particles and inclusion orientations are examined. The fatigue crack growth of a pre-existing crack nucleated in the matrix is finally investigated for an alumina inclusion by means of cohesive elements and damage mechanics. Results for different load conditions and different crack orientations are compared.

Publications

The following publications are part of the thesis.

[P1] M. Cerullo, Application of Dang Van criterion to rolling contact fatigue in wind turbine roller bearings: Proceedings of the 13th International Conference on Fracture, Beijing, China, 16-21 June 2013. Published on a USB stick.

[P2] M. Cerullo, Application of Dang Van criterion to rolling contact fatigue in wind turbine roller bearings under elastohydrodynamic lubrication conditions, P I Mech eng C-J Mec, 2014, 228 (12) 2079–2089. DOI 10.1177/ 0954406213516946.

[P3] M. Cerullo, V. Tvergaard. Micromechanical study of the effect of inclusions on fatigue failure in a roller bearing (Accepted in International Journal of Structural Integrity).

[P4] M. Cerullo. Sub-surface fatigue crack growth at alumina inclusions in AISI 52100 roller bearings. XVII International Colloquium on Mechanical Fatigue of Metals (ICMFM17), Procedia Engineering 2014 Vol. 74 pag. 333–338. DOI: 10.1016/j.proeng.2014.06.274.

Contents

Chapter 1

Introduction

1.1 Background

When two bodies in motion are in contact and the relative velocity of the surfaces of the two bodies is zero in the point of contact, the two bodies are said to be in rolling contact [1]. In real cases, due to deformability of the bodies, the point or the line of contact becomes an area of contact, and slip or partial slip can occur. Typical examples of elements subject to rolling contact are roller and ball bearings, cams, gears and railways. Failure in these structural elements is usually material fatigue, that may develop either on the surface or in a subsurface region, due to the high number of repeated loadings [2–4]. Rolling contacts are characterized by a small area of contact and for this reason high stresses can be reached, usually of the order of a few giga pascal. The state of stress, which is governed by Hertzian theory [5], is multiaxial and involves a small volume of material. Typical contact widths, in fact, can be a few hundredths of millimeters, and maximum Von Mises stress is reached below the surface, according to Hertz theory, at approximately 0.5 and 0.78 times the Hertzian half contact width, depending on wheather it is point contact (sphere-sphere or sphere-plane) or line contact (cylinder-cylinder or cylinder-plane).

In order to increase the efficiency of the structural elements and also to prevent wear due to the repeated contact between the surfaces, a lubricant, such as circulating oil or grease, has to be used. The lubricant, subject to high pressure in the contact region, may increase its viscosity considerably, acting almost as a solid. This, together with the relative speed of the two bodies in contact, results in a loss of symmetry in the classic elliptical Hertzian pressure distribution, causing spikes that depend, among other things, on the load and on the relative speed [6]. The lubrication regime, if lubricant is

kept clean and a sufficient film thickness is guaranteed, is referred to as the elastohydrodynamic lubrication regime (EHL). The highly localized pressure spikes, which can be much higher than the corresponding Hertzian peak stress, can be detrimental for the fatigue life of the material, but in practical design and studies they are often neglected, in favour of the simpler Hertz distribution.

Modeling rolling contact fatigue (RCF) is a challenging task, as fatigue life and mechanisms are really dependent on parameters such as the load, the roughness, the lubricant temperature, the residual stress state, the steel cleanliness, etc. For this reason a first systematic approach to design bearings against failure dates back to the 1940s, with the pioneering work of Lundberg and Palmgren [7, 8]. Since then, due to the increasing usage and demand for reliability, many studies and theories, both analytical, empirical and numerical, have been proposed to interprete and model the complex phenomena that cause failure in these mechanical subsystems. Though today a better understanding has been reached, still scatter in fatigue life and open questions are debated.

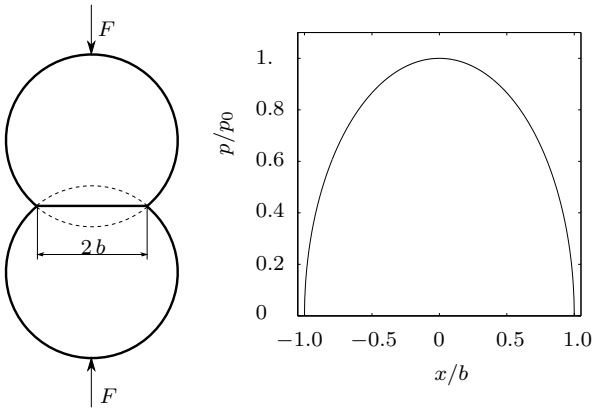

(a) (b)

Figure 1.1: (a) An example of contact between two cylinders (out of scale) and (b) the corresponding Hertzian pressure distribution.

1.2 Rolling contact fatigue

Two main mechanisms are identified as modes of failure in RCF. In the first case a small crack initiates on the contact surface, at some irregularity such as a dent or a scratch. The crack then propagates with a low angle toward the core of the material till it reaches a critical lenght at which it branches

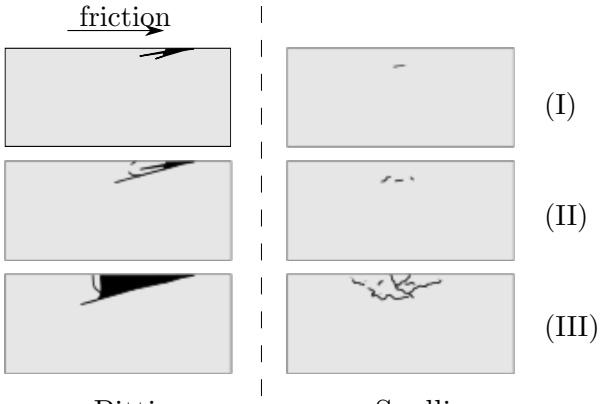

Figure 1.2: Mechanism of (a) surface initiated pitting and (b) subsurface initiated spalling.

toward the surface causing a piece of material to flake out, see Fig. 1.2a . This mechanism is usually called pitting or micro-pitting [2–4] and it is typical of structural elements such as gears and poorly lubricated or highly loaded bearings. If the load is not too high, the surfaces are relatively smooth and the lubricant is kept sufficiently clean, cracks are more likely to nucleate in the subsurface region, close to the depth at which the maximum shear stress is reached. In this case the crack often initiates at nonmetallic inclusions, that act as stress risers. Once the crack has nucleated, it propagates towards the surface of the material causing the failure of the structural element. This mechanism is referred to as spalling [2–4], Fig. 1.2b.

In rolling contact the stress components are non proportional and out of phase and a large hydrostatic pressure is usually present, see Fig. 1.3. Principal axes and planes of maximum shear stress are continuosly changing and, as said before, an extremely small stressed volume is involved. This higly localized nature leads to an enhanced effect of microstructural features (grain sizes, hydrogen content, defects, material inclusions) on the fatigue life and scatter in the data [4, 9–20]. A typical bearing steel, commonly used for bearing applications and for research investigations is the 100Cr6, the AISI/SAE 52100, or the equivalent japanese JIS-SUJ2. This is a high-carbon chromium low alloy steel for which the approximate composition is reported in Table 1.1. It is characterized by a high tensile strength, high resistance to wear and high hardness, especially if tempered or quenced ($\sim 600\ HV$ or above). Different compositions and shapes of inclusions are usually present in the AISI 52100, as alumina (Al_2O_3), TiN or MnS. Other inclusions may

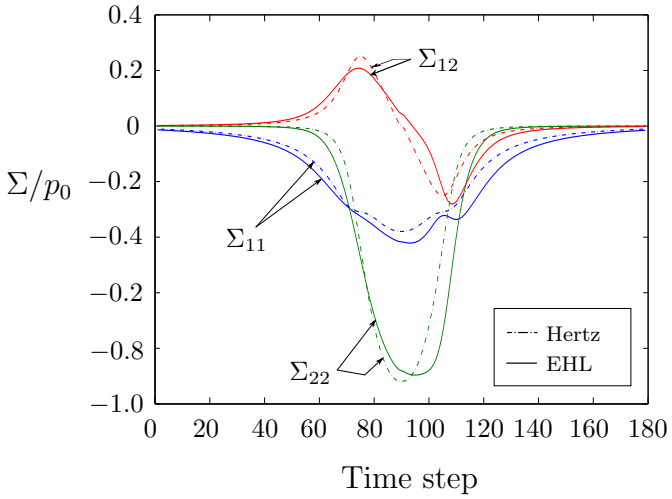

Figure 1.3: A typical rolling contact stress history in a subsurface point [21]. Both Hertzian and elastohydrodynamic lubrication cases are plotted.

also be present, and a complete and detailed overview can be found in [9]. Alumina and TiN are usually found as isolated defects, in spherical and cubic shape, respectively. Manganese sulphide (MnS) inclusions usually have an ellipsoidal shape, and can be found isolated or in clusters [22, 23].

The effect of inclusions on the fatigue life is maybe one of the most important factors in the fatigue life of a bearing steel, and, in general, of any steel operating in the very high cycle fatigue (VHCF) regime, i.e. for a number of cycles N greater than 10^{11}. It is well known, in fact, that fatigue life and mechanisms may vary a lot according to the stress level applied and that a dual step S–N curve characteristic may appear in the ultra long life regime [24–27]. At stress levels higher than the conventional fatigue limit, in fact, failure is more likely to be expected close to the surface of the material, while at a stress level close to or below the fatigue limit, which is also the case for bearings, failure usually occurs at small internal defects. The latter mechanism becomes dominant in the very high cycle regime, while a coexistence of

C	Si	Mn	P	S	Cu
0.99	0.23	0.34	0.014	0.014	1.45
Cr	Ni	Ti	Al	N (ppm)	O (ppm)
1.45	0.02	0.001	0.025	45	8

Table 1.1: Weight percentage composition of bearing steel SUJ2, equivalent to SAE 52100 [9].

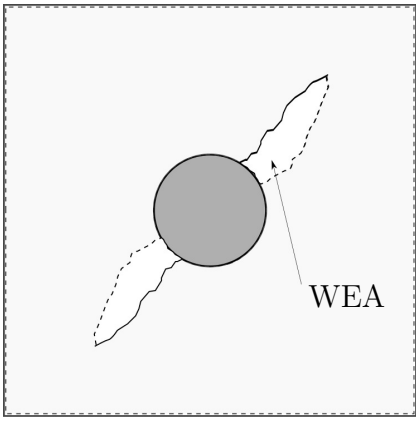

Figure 1.4: Schematic representation of a butterfly defect with white etching cracks. It is possible to note the two white etching areas forming the "wings" of the butterfly: each of them is delimited by a crack (continous line) and another boundary (dashed line).

surface and subsurface failures is present in the range between 10^6–10^9 cycles [24–28]. Inclusions or pores may act as stress concentration sites, and cracks may nucleate around these defects and then propagate to the surface. In the VHCF regime microstructural changes are often observed around inclusions, where an area, known as fish-eye, fine granular area (FGA) or optically dark area (ODA), may develop for low stress amplitudes [9, 13, 16, 17, 25, 26]. Particular features, known as white etching cracks (WECs), as they appear white after being etched in nital, are chacteristics of cracks nucleated at inclusions in materials subjected to rolling contact [3, 13, 16, 17, 19, 29–34]. Cracks, nucleated at the matrix-inclusion interface, appear in couples, i.e. with two "wings" on opposite sides of the inclusion, and inclined at an angle approximately oriented at 45° with respect to the rolling surface, see Fig. 1.4. The martensitic structure in the WECs does not appear anymore and, instead, an amorphous-like ultra-fine and free of carbide material is observed. It is not clear wheater or not this formation preceeds or follows the crack nucleation, and many theories have been proposed for their formation, and a review on the topic was written by Evans [13]. It is evident anyway that they are intimately related to the alteration induced in the microstructure due to the RCF process. The residual stresses around the inclusions, which are a result of the solidification process and are caused by the mismatch in the thermal expansion coefficients of the inclusion and the matrix, are also an important issue that should be addressed, but results in literature are not conclusive [9, 18, 35]. However the overall macroscopic residual stress state in the bearing rings is believed to significantly affect the fatigue life and the crack propagation after the initiation, and several results are reported in

literature [34–36].

1.2.1 Wind turbine gearbox bearings

A typical mechanical subsystem that may experience rolling contact fatigue is wind turbine gearboxes. This is of a particular interest for this PhD project which is part of a bigger project called "REWIND", that is aimed to improve the reliability of wind turbines.

As the drivetrain of a wind turbine has a low rotational speed, around $13-20\,rpm$, a multi-stage gearbox, usually a mix of a parallel and a planetary gear, is needed to increase the speed up to the generator speed (around $1600\,rpm$) [37]. It has been seen [38, 39] that one of the important reasons[1] for corrective maintenance of a wind turbine is failure due to rolling contact fatigue in one of the bearings in the gear box [40]. Therefore, the interest in the reliability of gearboxes has grown over the last years [41, 42]. Though failure rates in electrical systems and other subassemblies in a wind turbine are in fact higher, or at least comparable with faults in the gearbox, recent studies [43, 44] show that the downtime, in terms of hours lost per failure, is much higher for the latter. This, rather than the failure rate, is therefore one of the main reasons for the industry's focus on these subsystems.

In the gearbox, the bearings used are mostly roller bearings, due to the high loads involved. The majority of wind turbine gearbox failures appear in the intermediate and high–speed shaft bearings [31], while failure is more unlikely to be observed in the planet bearings. Even if the lubricant is kept clean and the bearing is properly lubricated, roller bearings sometimes experience rolling contact fatigue that appears as a crack starting below the surface of the inner race [4, 33]. Even if more rare, pitting can also be found, as seen in [37]. Once nucleated, this crack quickly propagates to the surface, resulting in particles of material flaking and leading to the failure of the bearing. Roller bearings for wind turbine applications operate in the fully elastic range and are subjected to a very high number of load cycles, with an expected life of 20 years [45]. However, practical experience shows a high life scatter in these machinery elements, with failures that sometimes occur after a few years [31]. The failure of these elements is thought to be due mainly to inhomogeneities and nonmetallic inclusions, that act as sites for crack nucleation under rolling contact fatigue. The cracks usually nucleate around inclusions, where the material experiences high stress concentration and typical butterfly defects and WECs are observed [13, 17, 37].

[1] We here refer to causes related to mechanical failure.

1.3 Models and Design against RCF

As explained in the previous section, RCF is a complex phenomenon, and, as a result, the design of a structural element under rolling contact does not represent an easy task, and often simplifying assumptions have to be made. Among all, in many criteria the material is considered as homogeneous, i.e. free of defects, which actually play a key role in the fatigue life. According to Sadeghi [4], models in literature can be classified as probabilistic or deterministic models. The first ones are based mainly on the results of experimental testings, while the deterministic models are theoretical, and for this reason less sensitive to testing variables, but also often based on simplifying assumptions. Here a brief summary of the models proposed in literature is reported.

The current ISO standards [46] for roller bearings are based on a modification of the the Lundberg–Palmgren (L-P) model [7, 8], that after many decades is still the frame of many other models proposed. The L-P model predicts, in millions of cycles, the life L_{10} with 10% probability of failure as

$$L_{10} = \left(\frac{C}{P}\right)^p \tag{1.1}$$

where p is a coeffient that depends on the contact (it is equal to 3 for ball bearings and 10/3 for roller bearings), P is an equivalent load and C represents the dynamic load rating, obtained as function of the geometry and the material. Equation 1.1 is obtained by manipulating the expression for the probability of survival, which is inversely related to the maximum orthogonal shear stress and the number of loading cycles. The model completely neglects the possibility to have surface failure in the ring and also the presence of lubricant. However it is probably still the most used one.

An extension of the L-P model was proposed in the 80s by Ioannides and Harris [47] where the concept of a stress threshold, similar to a fatigue limit, was introduced. Though this model has also been widely applied, bearings seem to show a finite life even for extremely small loads, as predicted by the L-P theory. Different multiaxial fatigue criteria have been proposed [48–51], and some, e.g. the Dang Van criterion, has been used in particular for rolling contact applications. This criterion and its further modifications have been widely used in the last decades in the automotive industry, and, as also other multiaxial criteria, it introduces in the formulation the instantaneous hydrostatic pressure, in analogy to what happens in the 1D case, with the Goodman diagram that make use of a mean stress. In the formulation used here [52], the Dang Van criterion also correctly predicts the experimental observation of the independence of the fatigue limit in torsion from the mean

shear stress [53]. In spite of many applications, some studies have shown that the Dang Van criterion might be unconservative, predicting safer operating conditions than other criteria [52, 54–56], as for instance the Liu [48] or the Papadopoulos criteria [49]. This has been shown in particular for rolling contact problems as railways and bearings, where the Dang Van criterion predicts an over-optimistic behavior for high negative hydrostatic stresses [52, 54–56]. Desimone et al. [52] proposed for this reason a modification to the Dang Van safe locus, accounting for this issue and predicting a less sensitive behavior with respect to negative values of the hydrostatic stress. However it should be noted that none of these criteria, proposed for defect-free materials, account for the presence of defects in the material. This "virtual defect-free approach" may lead to scatter and uncorrect design, expecially in the high cycle regime, where the fatigue limit is strongly influenced by the inclusions.

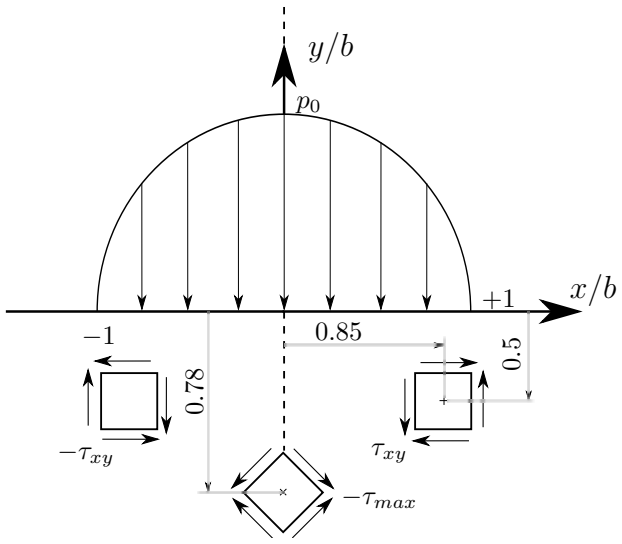

Figure 1.5: Line contact shear stresses in material subsurface according to Hertzian theory and for a maximum pressure p_0. The semi-half contact width is indicated with b and τ_{max} and τ_{xy} represent the maximum shear stress and the maximum orthogonal shear stress. The latter one is at the basis of the L–P model.

Chen et al. [57] reported that the depths at which first crack initiated at inclusions in bearing steel GCr15 (similar to SAE52100) and subject to rolling contact were in the range between 0.45 b and 0.7 b, where b is the Hertzian half-contact lenght. This is suggesting that either the maximum shear stress or the orthogonal shear stress, that according to Hertzian theory are reached at $0.78b$ and $0.5b$ [13], respectively, could be the driving force, see Fig. 1.5. On this assumption Sadeghi and others have carried out extended FE studies

to numerically model subsurface spalling under rolling contact, by means of damage mechanics, cohesive models and statistics [58–65]. Using Voronoi tessellation to mimic the grain microstructure in the material, fatigue crack initiation and propagation was modelled and good agreement to experimental evidence was found. It was also shown that, according to the simulations, a significant amount of fatigue life was spent in crack propagation, though some results showed the opposite [59]. Recently an extended study [66] including crystal anisotropy showed that maximum shear stresses were reached at grain boundaries, supporting the assumption of intergranular crack propagation made in previous studies.

1.4 Structure of the thesis

This thesis covers research on Rolling Contact Fatigue (RCF) in roller bearings for windmill applications and it is part of the bigger project REWIND, which is aimed to improve reliability for wind turbine critical components. The study is an initial step toward a better understanding of failure of these components and toward a safer design.

The research is summarized here, while it is elaborated in the appended papers written during the author's PhD work. These papers will be denoted by [P1] –[P4] in the following.

Chapter 2 is dedicated to the numerical modelling of RCF. The Dang Van criterion is introduced from the theoretical point of view, and its numerical implementation is explained. In the second part of the chapter the model for fatigue crack propagation is outlined.

Chapter 3 reports on the results obtained during the author's work. First a macromechanical study of a roller bearing under different load conditions is presented, and studied in light of the Dang Van fatigue criterion. Subsequently a micro-mechanical approach is discussed, where a single inclusion is embedded in a periodic unit cell subject to a characteristic stress history. Irreversable cohesive elements and LEFM are then employed to study fatigue crack growth in the matrix, where a pre-existing crack is assumed.

Chapter 4 finally sums up the thesis.

Chapter 2

Numerical modeling

2.1 The principle of virtual work

The numerical analyses in [P1] -[P3] are performed using the finite element approximation based on the principle of virtual work. The principle describes equilibrium in terms of the equality between internal and external virtual work. If body forces are neglected

$$\int_V \sigma_{ij}\delta u_{j,i}dV = \int_S T_i\delta u_i dS \tag{2.1}$$

where V denotes the volume, S the surface, T_i the traction, σ_{ij} the stresses and u_i the displacements. All the integrations are performed in the undeformed configuration. The notation for differentiation, $\partial()/\partial x_i = ()_{,i}$, where x_i are the Cartesian coordinates, applies.

For the numerical analysis in [P4] the incremental form of the principle of virtual work is adopted

$$\int_V \dot{\sigma}_{ij}\delta\dot{u}_{j,i}dV + \int_{S_t}(\dot{T}_n\delta\dot{u}_n + \dot{T}_t\delta\dot{u}_t)dS = \int_S \dot{T}_i\delta\dot{u}_i dS \tag{2.2}$$

where S_t represent the interface surface and T_n,T_t,u_n,u_t the normal and tangential components of the traction and opening displacements, respectively.

2.2 The rolling contact model

In order to investigate fatigue due to rolling contact in a roller bearing, a 2-D plane strain finite element model has been formulated: part of the initial geometry of the inner ring of the roller bearing is illustrated in Fig. 2.1a. Only an angular sector of the solid, with angular width $\alpha = 5°$, has been

modeled so that the computational time could be reduced. Far away from the surface, the region analyzed is terminated by a circular arc boundary with radius r. Along the sides,the solid is free to slide in the radial direction, being constrained in the direction perpendicular to the sides. A cartesian coordinate system $Oxyz$ is used, with the origin O in the center of the shaft, the axis z pointing out of the paper, and the axes x and y horizontally and vertically aligned, respectively. As a 2-D model is studied, no edge effects in the direction perpendicular to the plane of the model are accounted for.

The inner ring and the shaft have been considered as one body of external radius $R = R_s + t_k$, where R_s is the shaft radius and t_k is the thickness of the inner ring. This assumption is equivalent to neglecting contact stresses related to the mounting and any local stress concentrations at the interface between the ring and the shaft. The roller radius R_{roll} and length L had also to be introduced to model the pressure distribution acting on the inner race. The contact of the roller with the bearing raceway is simulated, in fact, by substituting the roller with the equivalent contact pressure distribution. Thus no contact algorithm was used here and instead two different pressure distributions were used to investigate the problem, see Fig. 2.2.

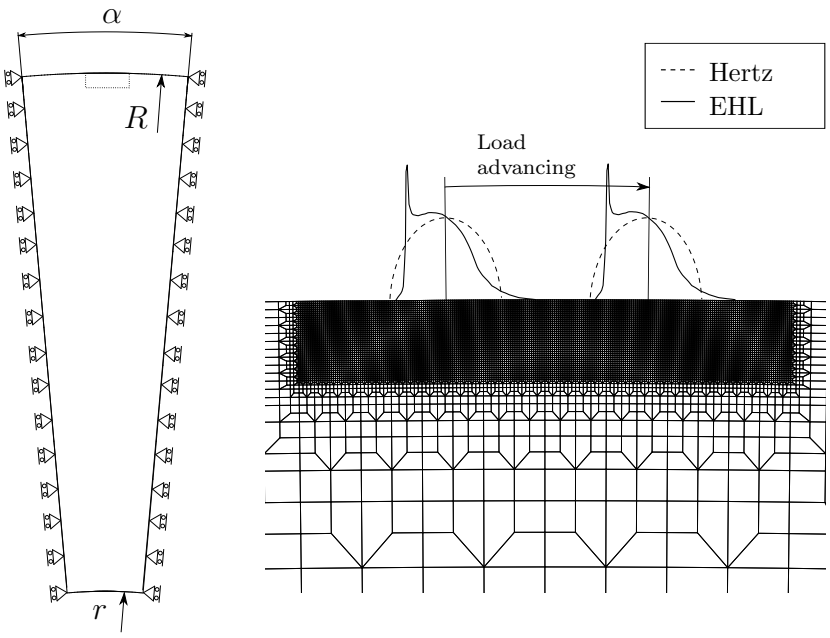

Figure 2.1: (a) Geometry used to model the problem in [P1] –[P2] : R represents the outer radius of the inner ring, r the radius limiting the lower bound of the region analyzed, and α the angle of the region analyzed. In (b) an example of the mesh used in the computations is shown: the extreme refined mesh region was necessary to resolve the extremely narrow peak of the EHL pressure distribution.

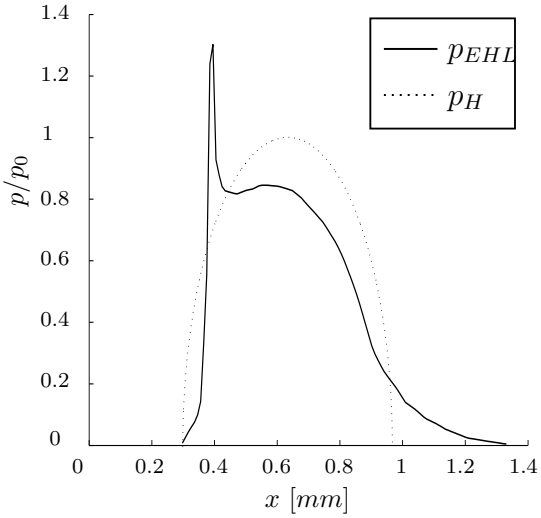

Figure 2.2: The two different normal pressure distributions used in the simulations, p_H and p_{EHL}. The two distributions are here plotted on an equivalent flat half space, according to the Hertzian model, where x_p in Eq. (2.3) is the center of the Hertzian pressure distribution.

A first distribution p_H is taken to be the static Hertzian pressure distribution for a line contact

$$p_H(x,y) = p_0 \left[1 - \left(\frac{x-x_p}{b}\right)^2 - \left(\frac{y-y_p}{b}\right)^2\right]^{(1/2)} \tag{2.3}$$

In Eq.(2.3), p_0 is the maximum value of the pressure, x_p and y_p the coordinates of the center of the contact area, b the semi-width of the contact area under the roller and x and y the coordinates of a generic point on the surface in the contact area. It should be noted that in the original Hertz model, no vertical coordinate is included and an equivalent half space is introduced. However, here it was choosen to map the Hertzian distribution on a round surface. The value of p_0 is related to the force acting on the roller by the relation

$$p_0 = \sqrt{\frac{q}{\pi}\frac{\Delta}{\rho}} \tag{2.4}$$

where $\Delta = (\frac{1-\nu_1^2}{E_1} + \frac{1-\nu_2^2}{E_2})^{-1}$ is function of Young's moduli E_i and Poisson's ratios ν_i of the roller and the inner race, here assumed of the same material. The constant $\rho = (\frac{1}{R} + \frac{1}{R_{roll}})^{-1}$ is a function of the curvature radii and $q = F/L$ is the force per unit length acting on the roller.

The second pressure distribution used in calculations, p_{EHL}, was inspired by [67], where a numerical program was developed to study different EHL

contact problems. Under EHL conditions, the high pressure causes the viscosity of the lubricant to increase exponentially: thus the lubricant becomes able to carry both normal and shear load and causes deformations in the two bodies in contact. As the normal load used in [67] is too small compared to typical loads for bearings in a wind turbine gear box, the original normal pressure distribution[1] has been scaled, ensuring that the total load, F, expressed in terms of the integral of the pressure over the contact area, is the same for the two distributions:

$$F = \int_{A_H} p_H \, ds = \int_{A_{EHL}} p_{EHL} \, ds \tag{2.5}$$

Thus, no separate solution has been obtained here for the EHL contact problem, but the p_{EHL} distribution applied here is considered useful for an indicative parametric study. Also, the particular profile obtained, has a more pronounced pressure spike, which is typical for high speeds, as those expected in high speed shaft roller bearings, that rotate up to 1500–1800 rpm. The shear load distribution, that depends, among others, on the normal load, on the viscosity of the lubricant and on the relative velocity of bodies, accounts for the friction in the contact. In order to take this into account, in some calculations a simplified assumption, indicated by tribological calculations currently carried out at the Technical University of Denmark. [68], was used for the shear stress distribution: $p_t = 0.1\, p_{EHL}$. The proportionality of p_t is equivalent to consider a uniform value of the friction coefficient throughout the contact. In these calculations this shear load distribution has thus been applied to the surface of the inner ring in contact, together with the normal distribution p_{EHL}. The resulting friction traction on the inner ring is oriented in the direction of the x axis. The load on the roller was here considered constant and the contact continuous, without any vibration effects.

The pressure distributions, that simulate the contact, are assumed to move along the surface, in a region where the mesh is uniform. The element size is then smoothly increased from this region to the edges, by a step up process. The material is considered isotropic, with Young's modulus $E = 210\ GPa$ and Poisson's ratio $\nu = 0.3$.

The FE mesh, with 12388 elements and 37561 nodes, consists of zones with different refinement and several steps up in order to decrease the number of elements and, at the same time, guarantee a sufficiently accurate solution in the subsurface region. The ratio of the half contact width b and the dimension dim_{el} of the elements in the uniform mesh region was taken to be $b/dim_{el} = 34$.

[1] Figure 4b in [67].

To validate the model, the results obtained in the computations were compared with the analytical solution for the Hertzian problem of two parallel cylinders in contact. From [1] the principal stresses at $x = 0$ can be written as

$$\begin{aligned} \sigma_x &= -\, p_0 \left[\frac{1 + 2(y/b)^2}{\sqrt{1 + (y/b)^2}} - 2|y/b| \right] \\ \sigma_y &= -\, p_0 \, \frac{1}{\sqrt{1 + (y/b)^2}} \\ \sigma_z &= \nu \, (\sigma_x + \sigma_y) \end{aligned} \tag{2.6}$$

while the maximum shear stress is

$$\tau_{max} = \begin{cases} (\sigma_z - \sigma_x)/2 & \text{for } 0 \leq |y/b| \leq 0.436. \\ (\sigma_z - \sigma_y)/2 & \text{for } |y/b| \geq 0.436. \end{cases} \tag{2.7}$$

In Eqs. (2.6)–(2.7) the coordinate system is centered in the point of contact, with x pointing to the right, y pointing downwards, and z aligned with the axes of the rollers. Results, which show a good correlation, are displayed in Fig. 2.3, where analytical solutions are plotted with continuous lines and the solution computed is represented by dots. Also it can be seen that the peak of the maximum shear stress, i.e. the Tresca shear stress, is reached at 0.78 b, in agreement with theory.

2.2.1 Load distribution of radial roller bearing

In Fig. 2.4 a schematic representation of the load distribution among the rolling elements in a rolling bearing subject to an external radial load F_r is depicted. It is known [69–71] that the radial load distribution in a rolling bearing can be approximated by

$$Q(\phi_j) = Q_{max} \left[1 - \frac{1}{2\varepsilon}(1 - \cos(\phi_j) \right]^t \tag{2.8}$$

where $Q(\phi_j)$ is the rolling element load at location $\phi_j = j\, 2\pi/Z$, Z is the number of rolling elements, Q_{max} is the maximum rolling element load and ε is given by

$$\varepsilon = \frac{1}{2} \left(1 - \cos(\phi_0)\right) \tag{2.9}$$

with ϕ_0 the angle corresponding to half of the angular load extension. The constant t in Eq. (2.8) is a parameter that can be chosen equal to 1.1 for roller bearings. The angle ϕ is computed from the vertical, assuming positive values in clockwise direction($j = 1, 2, \dots$) and negative values in the counter

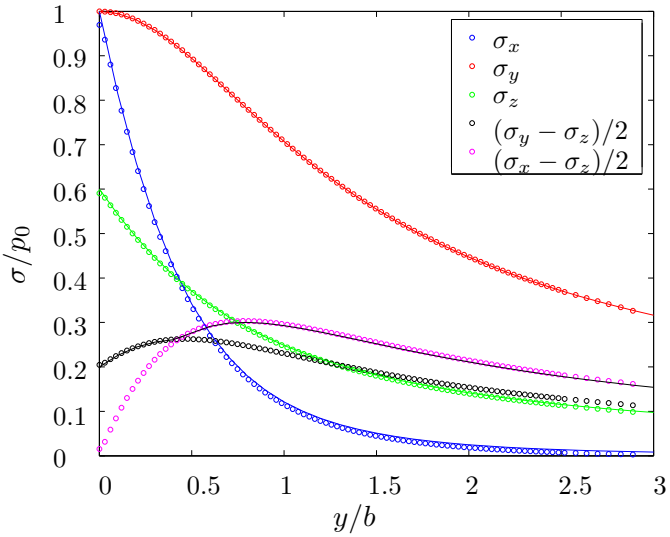

Figure 2.3: Principal stresses and maximum shear stress as function of the depth y from the contact surface. Stresses are normalized by the maximum contact pressure p_0 and the depth by the half-contact width b. The continous lines are the analytical solution from the Hertzian model and the dots represent results obtained in the computations.

clockwise direction ($j = -1, -2, \dots$), see Fig. 2.4. A value of $j = 0$ is assigned to the rolling element subject to the maximum load Q_{max}. For the static equilibrium the radial load must be equal to the sum of the vertical components of the rolling element loads

$$F_r = \sum_{\phi=-\phi_j}^{\phi=-\phi_j} Q(\phi)\cos(\phi) \tag{2.10}$$

that can be also written as

$$F_r = ZQ_{max}J_r(\varepsilon) \tag{2.11}$$

where $J_r(\varepsilon)$ is the radial integral proposed by Sjövall [70]

$$J_r(\varepsilon) = \frac{1}{2\pi}\int_{-\phi_0}^{\phi_0}\left[1 - \frac{1}{2\varepsilon}\left(1 - \cos(\phi)\right)\right]^t \cos(\phi)\, d\phi \tag{2.12}$$

From Eq. (2.12) it is possible to determine the maximum load Q_{max} once F_r and $J_r(\varepsilon)$ are known. In fig. 2.5 the radial integral $J_r(\varepsilon)$ for a roller bearing is plotted for different values of ε. It is noted that $0 < \varepsilon < 0.5$ ($\phi_0 < 90°$) corresponds to positive clearance, $\varepsilon = 0.5$ ($\phi_0 = 90°$) corresponds to zero clearance and $0.5 < \varepsilon < 1$ ($90° < \phi_0 < 180°$) corresponds to negative

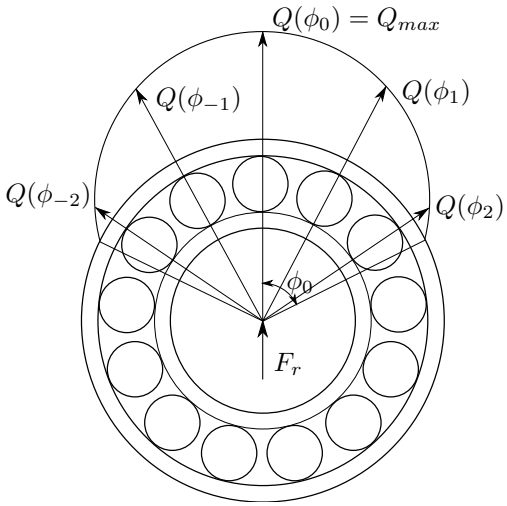

Figure 2.4: The radial load distribution in a roller bearing.

clearance, i.e. interference. In the following, some calculations have been carried out to study the effect of the variable load on the inner race. It was assumed $\varepsilon = 0.5$ ($\phi_0 = 90°$) and a number of 7 rolling elements loaded ($j = -3, -2, \ldots, 2, 3$), but any other values could have been chosen, given the bearing geometry and the interference fit. Different sets of maximum pressure p_0 were investigated, $p_0 = 0.8\ GPa$, $p_0 = 1\ GPa$, $p_0 = 1.2\ GPa$ and $p_0 = 1.4\ GPa$ and it was assumed that they were the value of the Hertzian pressure reached at $\phi = 0°$ ($j = 0$), corresponding to the maximum rolling element load Q_{max}. The pressure was related to the value of Q_{max} using Eq. (2.4) and the radial loads $Q(\phi_j)$ were calculated and imposed, so that it was possible to simulate the real stress history experienced by a material point in a roller bearing. The stress history was recorded in the material points at the depths of maximum shear stress ($0.78b|_{Q_{max}}$), maximum orthogonal shear stress ($0.5b|_{Q_{max}}$) and maximum Dang Van damage factor (see Sec. 2.3). The stress histories were then subsequently used in a micromechanical study, see Sec. 3.2 and Sec. 3.3.1.

2.3 The Dang Van criterion

The Dang Van criterion [50, 51] is a stress based multiaxial fatigue criterion that relates the variation of the stress state in a material point to a critical parameter λ that should not be reached:

$$f[\sigma_{ij}(t)] \leq \lambda \tag{2.13}$$

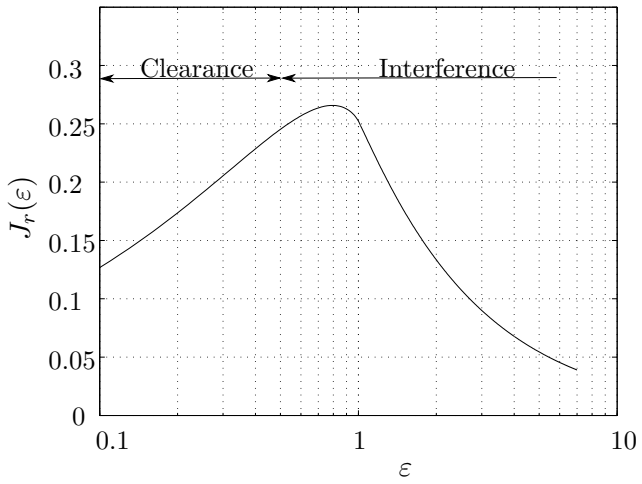

Figure 2.5: The radial integral $J_r(\varepsilon)$ plotted against the variable ε.

The critical value λ is usually a function of the fatigue limit in pure torsion, τ_w, and the fatigue limit in pure bending, σ_w and its choice is essential in a multiaxial criterion since it establishes which are the most important stress components, assumed to influence failure.

The Dang Van criterion assumes that even if at macro scale the stress state remains in the elastic regime, at grain scale the material can show some plasticity initially. For this reason, a residual stress tensor can exist such that the macroscopic stress tensor gives a state of stress under the yield limit. According to Melan's theorem on shakedown, this residual stress tensor must be time–invariant.

The criterion can be thus formulated as:

$$\tau_{max}(t) + \alpha_{DV}\sigma_H(t) \leq \tau_w \tag{2.14}$$

where

$$\alpha_{DV} = 3\left(\frac{\tau_w}{\sigma_w} - \frac{1}{2}\right) \tag{2.15}$$

is a constant that depends on the material fatigue limits previously mentioned, $\sigma_H(t)$ is the instantaneous hydrostatic component of the stress tensor and $\tau_{max}(t)$ is the instantaneous value of the Tresca-like shear stress

$$\tau_{max}(t) = \frac{\hat{s}_I(t) - \hat{s}_{III}(t)}{2} \tag{2.16}$$

The stress deviator is obtained by the usual definition:

$$s_{ij}(t) = \sigma_{ij}(t) - \delta_{ij}\sigma_H(t) \tag{2.17}$$

Then a constant tensor, s_{ij}^m, is calculated as that particular s_{ij}^* that solves the minmax problem

$$\min_{s_{ij}^*} \max_t [(s_{ij}(t) - s_{ij}^*)(s_{ij}(t) - s_{ij}^*)] \tag{2.18}$$

The shifted deviator tensor can then be defined as

$$\hat{s}_{ij}(t) = s_{ij}(t) - s_{ij}^m \tag{2.19}$$

The principal values of the shifted tensor appear in Eq. (2.16). The problem in Eq. (2.18) is solved iteratively using a move limit approach:

$$\min_{s_{ij}^*} \max_t [(s_{ij}(t) - s_{ij}^*)(s_{ij}(t) - s_{ij}^*)] = \min_{s_{ij}^*} [\max_t \ \Phi\,] \tag{2.20}$$

with

$$\Phi = \Phi\left(t, s_{ij}(t), s_{ij}^*\right) \tag{2.21}$$

Choosing an arbitrary starting value for s_{ij}^*, for example the average deviatoric stress tensor in the stress history for that material point, then for every iteration we identify the maximum value of Φ. Let t_m be the time step at which max Φ happens, then the value of s_{ij}^* is updated

$$s_{ij}^* = s_{ij}^* + ds_{ij}^* \tag{2.22}$$

with

$$ds_{ij}^* = \gamma\ \left(s_{ij}(t_m) - s_{ij}^*\right) \tag{2.23}$$

which can be interpreted as a modified steepest descend method. If at one step Φ increases, γ is reduced to $0.25\,\gamma$. The iteration is stopped if the norm of the difference between s_{ij}^* at the current iteration step k and at the previous step falls into a tolerance range:

$$\|s_{ij}^*|_k - s_{ij}^*|_{k-1}\| < \varepsilon_{toll} \tag{2.24}$$

Although a superimposed hydrostatic tension has an effect on the fatigue life in normal cyclic loading [53], several studies [72, 73] have shown that a superimposed mean static torsion has little or no effect on the fatigue limit of metals subjected to cyclic torsion. The independency of the mean shear stress is correctly predicted through the minimization process in Eq. (2.18), see also [52, 53]. The Dang Van proposal is equivalent to request, in the $\sigma_H(t)$ - $\tau_{max}(t)$ plane, that all the representative points of the stress state, fall below the line intersecting the $\tau_{max}(t)$ axis at τ_w with a negative slope of α: if all of the points fulfill this requirement, the criterion predicts

a safe life for the component (see Figure 2.6). The original Dang Van safe locus predicts a detrimental effect of tensile hydrostatic stress while an over-optimistic positive effect is expected under compressive hydrostatic stress. The negative effect of tensile mean stress is well known in literature from classic Haigh diagrams, that also show a flat response for negative stress ratios [74, 75]. For this reason it is not too conservative to choose a different safe locus in the Dang Van plane to be in agreement with this response, for example a bilinear limit curve, as proposed in [52]. The safe locus could be therefore identified in two segments, one with a null slope and the other one with a negative slope equal to α_{DV} (Figure 2.6). For $\sigma_H(t) \geq \sigma_A$ the safe region is identical to the original Dang Van region, while for smaller values of $\sigma_H(t)$, the cut-off with the flat curve replaces the Dang Van limit curve by a curve more on the safe side. Values of $\sigma_A = \sigma_w/3$ and of $\tau_A = \sigma_w/2$ have been proposed in [52], on the basis of experimental results obtained on high-strength steel smooth specimens. It is possible, if experiments are available to support that, to choose a different set of values for (σ_A, τ_A), but here the same choice has been made as that in [52]. If the ratio of the fatigue limits, τ_w/σ_w, was equal to 0.5, the value α_{DV} in Eq. (2.14) would be zero, which is far from reality, as steels usually show ratios between 0.57 and 0.8 [53].

In the following sections, both the original safe locus and a new one with the mentioned cut-off will be used, and results are compared. For τ_w a value of 360 MPa has been imposed [76] and a ratio $\tau_w/\sigma_w = 1/\sqrt{3} \approx 0.577$. With this assumption the value of the constant α_{DV} used in the calculations is approximately 0.232. For a material point subjected, at time t, to $\sigma_H(t)$

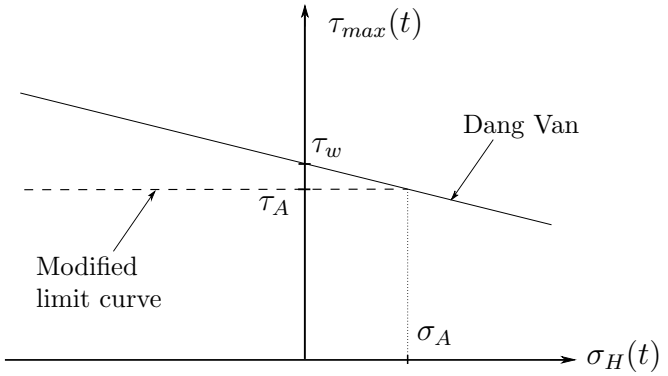

Figure 2.6: The Dang Van safe locus: the dashed line represents the alternative limit curve, for $\sigma_H(t) < \sigma_A$, here assumed equal to $\sigma_w/3$, as proposed in [52].

and $\tau_{max}(t)$, the ratio between $\tau_{max}(t)$ and the corresponding limit value for that $\sigma_H(t)$ is here used to define the damage factor $n(t)$. Points on the

limit curve, then, result in a unit damage factor while points inside the safe region have a damage factor smaller than one. As previously mentioned, two different safe loci are here used: one with a linear limit curve and another one with a bilinear limit curve. Consequently, a damage factor is here defined as

$$n(t) = \frac{\tau_{max}(t)}{\tau_w - \alpha_{DV}\,\sigma_H(t)} \tag{2.25}$$

if referred to the original Dang Van's safety region or

$$n(t) = \begin{cases} \frac{\tau_{max}(t)}{\tau_w - \alpha_{DV}\,\sigma_H(t)} & \text{if } \sigma_H > \sigma_A \\ \\ \frac{\tau_{max}(t)}{\tau_A} & \text{if } \sigma_H \leq \sigma_A \end{cases} \tag{2.26}$$

when the bilinear limit curve is used. As mentioned above, σ_A and τ_A are here chosen equal to $\sigma_w/3$ and $\sigma_w/2$, respectively.

2.4 Periodic Boundary Conditions

In [P3] the macroscopic stresses found in [P2] are applied to a representative volume element (RVE) to investigate the influence of inclusions. This separate micromechanical approach is necessary as modelling an inclusion in the macro-mechanical model proposed in [P1] -[P2] would make the computation prohibitively expensive. Thus, a RVE is used instead, and stresses are applied as periodic boundary conditions. The unit cell is assumed to be so small relative to the bearing geometry that the use of periodic boundary conditions gives a good approximation. The unit cell is considered to be made of an AISI 52100 bearing steel matrix, in which an inclusion is embedded. Two different types of inclusions are studied here, an Al_2O_3 inclusion and a TiN inclusion. The first type of inclusion is usually found in spherical or ellipsoidal shape and here it has been modeled with a circular shape (Fig. 2.7a), as a 2D plane strain calculation is carried out. The second inclusion type, made of TiN, is found in cubic shape, and it is here modeled as a square shaped inclusion (Fig. 2.7b). A small round off at the square corners of the inclusion is introduced to prevent an excessive stress concentration. The values of $E_i/E_m = 1.8523$ and $E_i/E_m = 1.5095$ have been used as ratios between the inclusion and the matrix Young's moduli, for alumina and titanium nitride, respectively. The Poisson's ratio ν_i is taken to be 0.25 for alumina and 0.192 for titanium nitride. The matrix has a Young's Modulus $E_m = 210\ GPa$ and a Poisson's ratio $\nu_m = 0.3$. Different volume fractions have been considered for both types of inclusions. For TiN also the influence

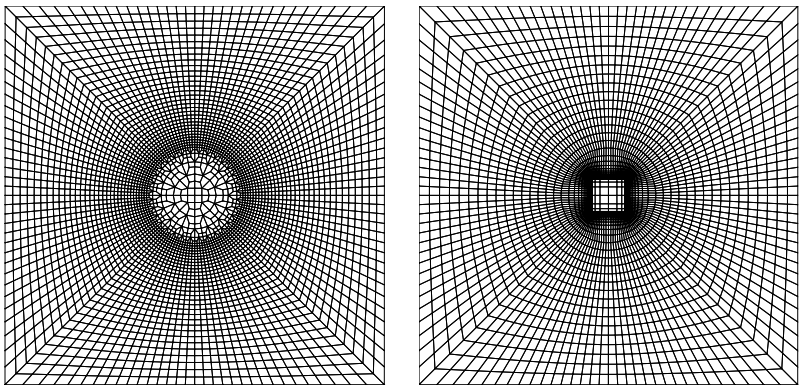

(a) (b)

Figure 2.7: Example of the different meshes used to model the RVE. (a) Model for Al_2O_3 , with volume fraction $V_f = 0.01$ (b) Model for TiN, with $V_f = 0.001$.

of the orientation of the inclusion relative to the surface of the inner ring has been studied. The orientation of the inclusion is specified by the angle ϕ between the axis x_i of the inclusion coordinate system and the axis x_m of the global coordinate system (Fig. 2.8). The axis x_m is parallel to the tangent of the inner race surface in the nearest contact point, and it is oriented in the rolling direction.

Periodic boundary conditions on the unit cell in Fig. 2.9 are applied, as described in [77]. Along the left and right edges of the cell the BC's are:

$$\begin{array}{rcl} u^1(\xi_1) - u^1_A = u^1(\xi_2) - u^1_B & , & u^2(\xi_1) - u^2_A = u^2(\xi_2) - u^2_B \\ T^1(\xi_1) = -T^1(\xi_2) & , & T^2(\xi_1) = -T^2(\xi_2) \end{array} \tag{2.27}$$

where ξ_1 and ξ_2 are length coordinates in Fig. 2.9. Along the top and the bottom of the unit cell the BC's are

$$\begin{array}{rcl} u^1(\eta_1) - u^1_A = u^1(\eta_2) - u^1_D & , & u^2(\eta_1) - u^2_A = u^2(\eta_2) - u^2_D \\ T^1(\eta_1) = -T^1(\eta_2) & , & T^2(\eta_1) = -T^2(\eta_2) \end{array} \tag{2.28}$$

where η_1 and η_2 are defined in Fig. 2.9. The displacements of the four corner nodes are denoted u^i_A , u^i_B , u^i_C and u^i_D. In order to prevent rigid body motion, the two displacements u^i_A are chosen equal to zero, and also $u^2_B = 0$. Finally, periodicity requires that $u^i_C = u^i_D + u^i_B$, and therefore only the three displacements u^1_B , u^1_C and u^2_C are free to be prescribed.

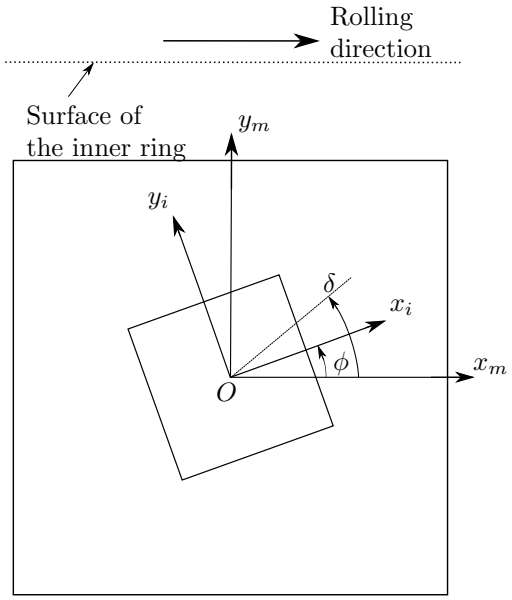

Figure 2.8: Orientation of the RVE with respect to the contact point on the inner race surface. The angle δ will be used to specify the point where the maximum damage factor is reached. The angle ϕ only applies to the study of TiN inclusions and defines the orientation of the inclusion with respect to the rolling direction.

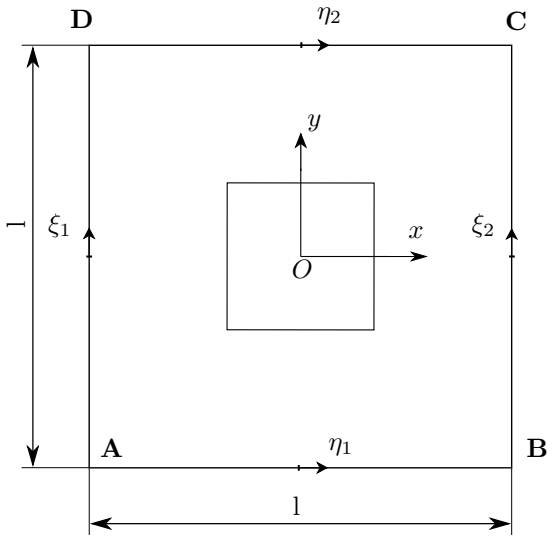

Figure 2.9: Coordinates for the unit cell analyzed.

Equations (2.27)-(2.28) are approximately satisfied using a standard penalty method

$$\begin{aligned} T^i(\xi_2) &= k\big(u^i(\xi_2) - u^i(\xi_1) - u^i_B + u^i_A\big) = -T^i(\xi_1) \\ T^i(\eta_2) &= k\big(u^i(\eta_2) - u^i(\eta_1) - u^i_D + u^i_A\big) = -T^i(\eta_1) \end{aligned} \tag{2.29}$$

where the stiffness k is chosen large enough to get a good approximation.

In order to apply the macroscopic stress history to the RVE, a superposition method has been used here to relate the macroscopic stresses to the three unknown displacements:

$$\begin{cases} \lambda_{11}\, u^1_B + \lambda_{12}\, u^1_C + \lambda_{13}\, u^2_C = \Sigma_{11} \\ \lambda_{21}\, u^1_B + \lambda_{22}\, u^1_C + \lambda_{23}\, u^2_C = \Sigma_{22} \\ \lambda_{31}\, u^1_B + \lambda_{32}\, u^1_C + \lambda_{33}\, u^2_C = \Sigma_{12} \end{cases} \tag{2.30}$$

The relation between the stresses and the three displacements is assumed to be linear.

The coefficients λ_{ij} have been evaluated by imposing alternatively a small value for one of the three independent variables, e.g. $0.001\, l$, and at the same time a null value for the other two. For each of the three cases, the macroscopic stresses Σ_{11}, Σ_{22} and Σ_{12} are calculated by integrating the traction vectors along the edges. The unknowns in Eq. (2.30) reduce to only three and therefore a column vector in the matrix of the coefficients can be evaluated for each case, calculating the coefficient λ_{ij} as the ratio of the macro stress component and the non zero displacement imposed. After three calculations, all the coefficients λ_{ij} are known, and it is possible to solve the system (2.30). For each time step the three displacements corresponding to the macroscopic stress component are thus calculated from Eq. (2.30) and these displacements are imposed in the finite element problem.

2.5 The Roe-Siegmund cohesive model

The Roe-Siegmund cohesive model [78] was choosen here to study fatigue crack propagation in the material. This model, orignally intended to model low cycle fatigue in adhesives [78, 79], has also been used to model fatigue crack growth in metals [80–83]. In some of these works extra-terms were also incorporated to account, for example, for the triaxiality. Here, however, the original formulation was chosen.

According to the Roe-Siegmund model the traction separation law is given by a modification of the Xu–Needleman law. The two components of the

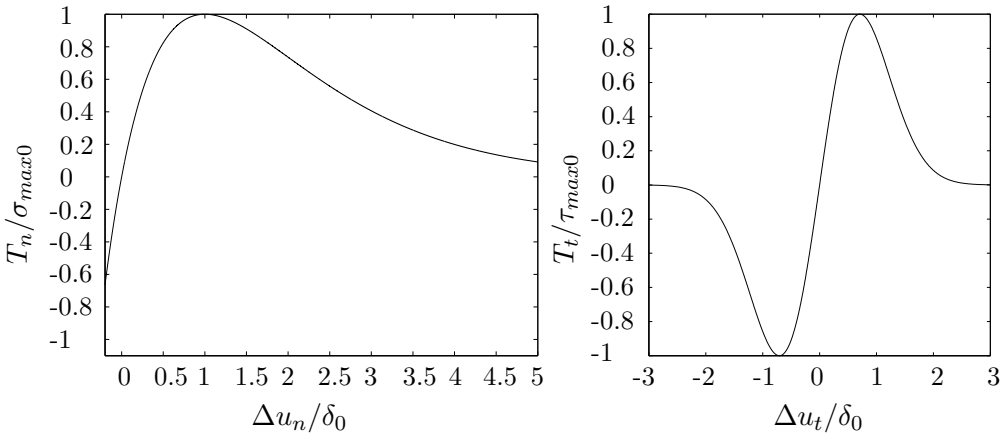

(a) (b)

Figure 2.10: (a) Normal and (b) tangential separation behavior.

cohesive surface traction, T_n and T_t, are given by:

$$\begin{aligned} T_n =& \sigma_{max} e \exp\Big(-\frac{\Delta u_n}{\delta_0}\Big)\Big\{\frac{\Delta u_n}{\delta_0}\exp\Big(-\frac{\Delta u_t^2}{\delta_0^2}\Big) + (1.0-q)\frac{\Delta u_n}{\delta_0} \\ & \Big[1.0-\exp\Big(-\frac{\Delta u_t^2}{\delta_0^2}\Big)\Big]\Big\} \\ T_t =& 2\sigma_{max} e q \frac{\Delta u_t}{\delta_0}\Big(1.0+\frac{\Delta u_n}{\delta_0}\Big)\exp\Big(-\frac{\Delta u_n}{\delta_0}\Big)\exp\Big(-\frac{\Delta u_t^2}{\delta_0^2}\Big) \end{aligned} \tag{2.31}$$

where Δu_n and Δu_t represent the normal and the tangential components of the displacement jump across the cohesive surface, $\Delta = \Delta u_n\,\mathbf{n} + \Delta u_t\,\mathbf{t}$. In Eq. (2.31) e is the Napier's constant, δ_0 is the critical opening, for which $T_n = \sigma_{max,0}$ and q represents the ratio between shear ($\Delta u_n = 0$) and normal ($\Delta u_t = 0$) cohesive surface energies under monotonic loading. The traction law is depicted in Fig. 2.10. Fatigue crack growth is modeled by introducing a damage parameter D [84], which can assume a value between 0 (initial state: undamaged material) and 1 (failure). Thus, in the undamaged element, when $D = 0$, the element has full strength, while for $D = 1$, it has no more load carrying capacity. If damage has evolved, the current cohesive strengths are defined as

$$\begin{aligned} \sigma_{max} &= \sigma_{max,0}(1-D) \\ \tau_{max} &= \tau_{max,0}(1-D) \end{aligned} \tag{2.32}$$

where $\tau_{max,0} = \sqrt{2e}q\sigma_{max,0}$. The unloading path follows a linear relationship with a slope equal to the slope of the traction separtion curve at zero

separation. Thus the unloading/reloading relations are given by

$$\begin{aligned} T_n &= T_{n,max} + \kappa\,(\Delta u_n - \Delta u_{n,max}) \\ T_t &= T_{t,max} + \kappa\,(\Delta u_t - \Delta u_{t,max}) \end{aligned} \tag{2.33}$$

where $T_{n,max}$ and $T_{t,max}$ are the normal and tangential tractions corresponding to maximum value of the normal and shear separation $\Delta u_{n,max}$ and $\Delta u_{t,max}$, respectively.

In order to relate the change of D to the displacements and the stresses, is it necessary to introduce a damage rate constitutive law

$$\dot{D}_c = \frac{|\Delta \dot{u}|}{\delta_\Sigma}\Big[\frac{\overline{T}}{\sigma_{max}} - C_f\Big] H(\Delta\overline{u} - \delta_0) \qquad \dot{D}_c \geq 0 \tag{2.34}$$

where $\overline{T}$ is the effective traction

$$\overline{T} = \sqrt{T_n^2 + (T_t/2eq)^2} \tag{2.35}$$

and $\Delta\overline{u}$ the accumulated separation, function of the effective displacement

$$\Delta u = \sqrt{\Delta u_n^2 + \Delta u_t^2} \tag{2.36}$$

and its increment $\Delta\dot{u} = \Delta u|_t - \Delta u|_{t-\Delta t}$. Thus the accumulated separation $\Delta\overline{u}$ can be defined as

$$\Delta\overline{u} = \int |\Delta\dot{u}|\, dt \tag{2.37}$$

If not stated differently, a value of $\delta_\Sigma = 4\,\delta_0$ is assumed. If the crack is closing ($\Delta u_n < 0$) the effective traction reduces to only the contribution from shear, i.e. there is no contribution from the normal traction T_n in Eq. (2.34). In the preliminary results, obtained in [P4] , instead, even during crack closure, the effective traction was not reduced to the shear stress, and it was given by Eq. (2.35). This resulted in a fast propagation, as in RCF the crack is closed during most of the cycle, and there are high negative normal stresses. In order to avoid an excessive damage evolution during crack closure, in the other simulations the effective traction was thus taken to be

$$\overline{T} = \begin{cases} \sqrt{T_n^2 + (T_t/2eq)^2} & \text{if } \Delta u_n \geq 0 \\ \\ T_t/2eq & \text{if } \Delta u_n < 0 \end{cases} \tag{2.38}$$

The parameter C_f represents the ratio between the cohesive endurance limit and the initial undamaged cohesive normal strenght:

$$C_f = \frac{\sigma_f}{\sigma_{max,0}}, \;\; C_f \in [0,1] \tag{2.39}$$

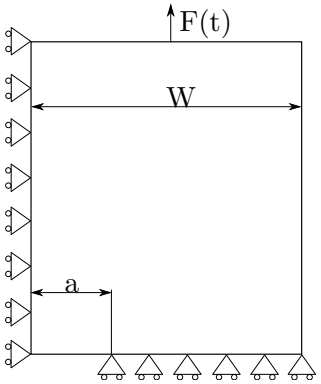

Figure 2.11: The quarter panel geometry used for the test case.

If $\frac{\overline{T}}{\sigma_{max}} - C_f \not> 0$ then no damage evolution occurs during that increment. Once an element has failed ($D = 1$), it still retains some strength in compression, if $\Delta u_n < 0$, such that overlap is penalized

$$T_{n,compr} = \alpha T_{n,compr}(\Delta u_t, \Delta u_n, \sigma_{max} = \sigma_{max,0}) \quad , T_t = 0 \quad if \;\; \Delta u_n < 0, \;\; D = 1 \tag{2.40}$$

where a value of $\alpha = 10$ was here chosen.

2.5.1 Fatigue crack growth: A test case

A test case with a cracked panel (Fig. 2.11) subjected to $R = \sigma_{min}/\sigma_{max} = 0$, $\sigma_{max} = 100\ MPa$ was carried out, in order to evaluate the Siegmund's model parameters δ_0, σ_{max0} and C_f to be used in [P4] . The parameter q was set equal to 0.429, so that the maximum normal and shear stresses are the same. Furthermore, the fatigue limit C_f was set equal to 0.005. This choice is justified by the need to reduce the set of parameters to be varied in the test case computations. When fixing the value of C_f in fact, δ_0 and σ_{max0} were the only two other parameters to be fitted. The value of C_f choosen is justified in the prospective of modeling the VHCF regime, where even small values of the stress imposed, below the conventional fatigue limit, may cause failure. Though these preliminary computations were set to fall into the low cycle regime, this seemed the best choice. Furthermore, it is worth to notice that the test case was carried out assuming long–crack theory even though the subsequent case assumed cracks in the order of a micron.

A Paris law with $C = 11 \cdot 10^{-10}$ and $m = 4.05$ was fitted with the set of parameters $\delta_0 = 0.5\ \mu m$, $\sigma_{max0} = 21000\ MPa$ and $C_f = 0.005$, see Fig. 2.12. The resulting crack growth rate is in the order of $10^{-6}\ m/cycle$, with an initial $\Delta K_I \approx 5.63\ MPam^{0.5}$ ($DK_{th} = 5\ MPam^{0.5}$). This crack growth rate

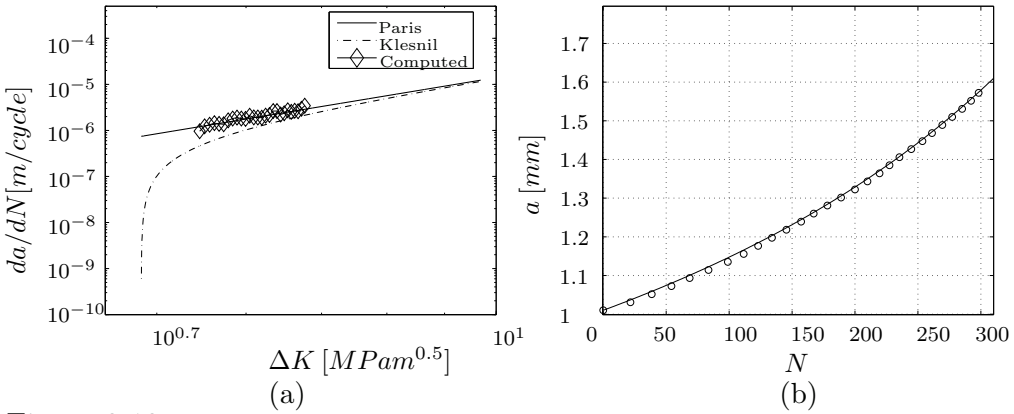

Figure 2.12: (a) Fatigue crack growth rate versus the stress intensity range for the test case and (b) corresponding crack lenght–cycles curve.

is at least 3 order of magnitude higher than what is expected for this material for cracks in vacuum [85, 86], but it was here chosen to have a qualitative understanding of the crack propagation under rolling contact, rather than trying to simulate the exact number of cycles to failure which is, on the other hand, practically unfeasible in the giga cycle regime. The parameters for the cohesive law were thus used in the following calculations to study crack propagation in the inclusion–matrix unit cell [P4] .

2.5.2 Fatigue crack growth: rolling contact

The cohesive model described in Sec. 2.5 was used to model crack propagation in a material point subject to rolling contact fatigue. A similar approach to that in [P3] was used and, in fact, a similar RVE where an alumina particle is embedded in the metal matrix, was modelled.

The mesh used in the calculation is shown in Fig. 2.13, where it can be seen that in the matrix a pre-existing crack is assumed to have nucleated. The crack is oriented radially, and has one tip on the inclusion-matrix interface and the other tip in a region of very fine mesh. Several step up are used to increase the size of the elements in this region to the size of the elements at the edges of the RVE, so that the computational effort is reduced. The fatigue crack growth is modelled by failure of the cohesive elements aligned on the crack, that has an initial lenght a_0, and that it is oriented with an angle θ to the rolling direction (see Fig. 2.8). In the uniform mesh region along the crack, the element size, which is sufficiently small to resolve the cohesive region (see Sec. 2.6), is denoted as c. The initial crack lenght can assume values between the minimum crack length $a_{0,min}$ and the maximum

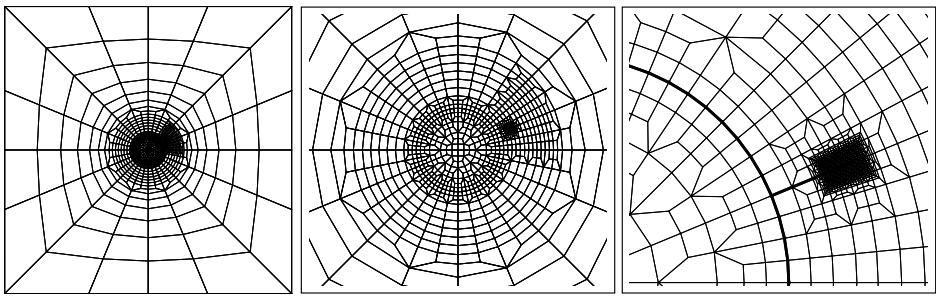

(a) (b) (c)

Figure 2.13: Mesh used for the calculations at full scale (a) and at different levels of detail (b)-(c). In (c) the mesh around the crack is shown. $\theta = 30°$

length $a_{0,max}$. This ensures that the crack tip is always in a region where at least 8 elements of the same lenght c preceed or follow the crack tip. Different cases were considered in the study, "CRC", "INT" and "POR", see Fig. 2.14. The first two assume an inclusion in the matrix, while the latter assumes a pore. The CRC case reflects the case of a crack in the matrix that is perfectly bonded to the inclusion. One crack tip lies on the boundary with the inclusion, and the other one lies in the matrix. The INT case models the case where the matrix–inclusion interface is flexible and therefore cohesive elements are used also along the interface, though they are not allowed to fail. The crack in this case has a tip in the matrix and a tip on the inclusion. In [P4] the jump procedure described in Sec. 2.5.2 was not adopted, and the effective traction was computed by means of Eq. (2.35). In the subsequent studies only the cases "CRC" and "POR" were investigated.

The RVE was subject to a stress history that was applied as periodic boundary conditions. Three different stress histories were used in the investigation, "HDV", "HTAU" and "HVM", corresponding to the macroscopic stress histories $\Sigma_{ij}(t)$ recorded at the depth of the maximum Dang Van damage factor, the maximum orthogonal shear stress and the maximum Von Mises stress, respectively.

The jump-to procedure

A jump-to procedure, similar to the ones proposed in [65] and [84] was used to avoid long computational times. At the beginning of the j-th cycle, the variable ΔD_i in the i-th gauss integration point is set to zero. At each increment this variable is increased by the damage increment in that material point and, at the end of the j-th cycle, ΔD_i will represent the damage increase, for that gauss integration point, during that cycle. An average of this quantity is calculated within all the integration points in each element and

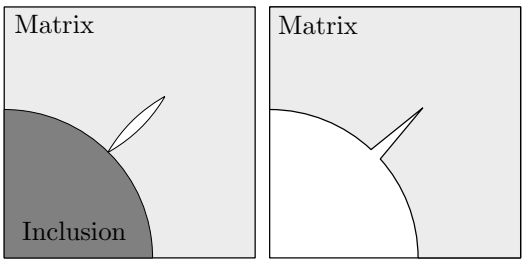

Figure 2.14: The two cases considered for the calculations, (a) "CRC" or "INT" and (b) "POR". A zoom view.

the maximum value ΔD_{max} among the all cohesive elements is then choosen. The number of cycles to skip is then given by

$$\Delta N = F(\Delta \overline{D}/\Delta D_{max}) \tag{2.41}$$

where F(X) is the operator that returns the greatest integer less than or equal to X and $\Delta \overline{D}$ is a constant. Thus the damage variable is updated in each point i as

$$D_i|_{j+\Delta N} = D_i|_j + \Delta N \cdot \Delta D_i|_j \tag{2.42}$$

and the cycle counter jumps from j to $j + \Delta N$. If ΔN is smaller than one, no jump is allowed during that cycle. The jump procedure was first tested on the quarter panel described in Sec. 2.5.1, and a value of $\Delta \overline{D} = 0.025$ was found to be needed for an accurate prediction of the crack growth. However the value of $\Delta \overline{D}$ depends on how fast the damage evolves, and therefore also on the stress history applied. For this reason, when the procedure was tested also for fatigue crack growth under rolling contact, it was found that this value was too big. The pace $\Delta \overline{D}$ was thus reduced till no jump was made and it was then choosen a value slightly bigger, $\Delta \overline{D} = 0.002$. In Fig. 2.15 the fatigue crack growth curves obtained with and without the jump procedure are plotted for different angles and for the HDV case. It is noted that when the jump procedure is active the computations return a faster crack growth. It was not possible to obtain a more accurate prediction without over complicating the procedure, and it was chosen to use this value for $\Delta \overline{D}$, that seemed on one hand to preserve the order of results obtained for different angles, and on the other hand allowed to have a faster computation.

2.6 Mesh sensitivity

In [P3] a rounding radius was introduced at the corner of the TiN inclusion to avoid a stress singularity, see Sec. 2.4. It is noted in fact that a sharp corner

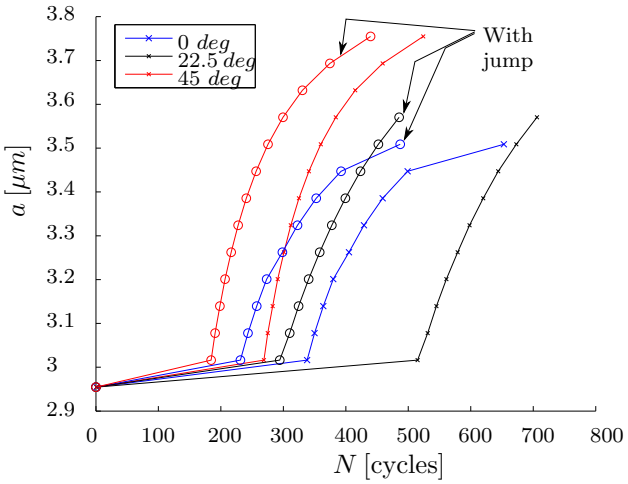

Figure 2.15: Comparison between results obtain with and without the jump-to procedure, for different crack angles θ and for the HDV case.

of the inclusion would result in a stress singularity, as has been analyzed by Tvergaard and Hutchinson [87] for the case of a ceramic with different grain properties. The rounding radius used was taken to be $\gamma\, l_{cub}$, where $\gamma = 0.15$ and l_{cub} is the half width of the inclusion. The value of γ was chosen applying a Hertz load history and results from [P3] are shown in Table 2.1 for two different volume fractions, $V_{f1} = 0.0063$ and $V_{f2} = 0.0292$. As the value of γ decreases, the maximum damage factor increases, since a more severe stress concentration is introduced. The value of 0.15 was chosen as a compromise between the need of a small rounding radius and a mesh not too distorted in the region close to the radius.

Table 2.1: Maximum Dang Van damage factor reached in the matrix, for different sizes of the rounding radius and two different orientations of a TiN inclusion. Results are shown for the Hertz stress history, corresponding to Fig. 1.3. $V_{f1} = 0.0063$, $V_{f2} = 0.0292$.

	0°		30°	
γ	V_{f1}	V_{f2}	V_{f1}	V_{f2}
0.20	0.9299	0.9221	0.9703	0.9618
0.15	0.9308	0.9228	0.9737	0.9651
0.10	0.9324	0.9245	0.9779	0.9692
0.05	0.9338	0.9259	0.9815	0.9727

A mesh convergence investigation, based on the Dang Van damage factor, was also carried out in [P3] for both Al_2O_3 and TiN inclusions, for the two volume fractions, $V_{f1} = 0.007$ and $V_{f2} = 0.073$, and for a Hertz stress history. The TiN inclusion was investigated for two different angles, $\phi = 0°$ and $\phi = 30°$. The number of elements along the interface N_{int} between the

matrix and the inclusion was doubled from 64 to 128 and, accordingly, the number of elements increased from 4972 to 9964 in the case of Al_2O_3 and from 3768 to 11768 for the TiN, see Fig. 2.16. It is noted that the element aspect ratio at the interface is kept fixed, so the increased number of elements around the particle also gives smaller elements in the radial direction. Results, listed in Table 2.2, show that there is little dependence, and that the discretization used in the analysis, with 64 elements along the interface and a much smaller number of elements, gives sufficient accuracy, with a percentage difference of the order of 0.5%. For this reason and because of a much reduced computational time, a value of $N_{int} = 64$ was used in the calculations.

Table 2.2: Mesh convergence analysis results in terms of the maximum Dang Van damage factor reached in the matrix. Hertzian stress history of Fig. 1.3 was here used, with $V_{f1} = 0.007$, $V_{f2} = 0.073$. N_{int} represents the number of elements along the interface between the matrix and the inclusion.

	Al_2O_3		TiN ($\phi = 0°$)		TiN ($\phi = 30°$)	
N_{int}	64	128	64	128	64	128
V_{f1}	1.0137	1.0077	0.9294	0.9200	0.9723	0.9561
V_{f2}	0.9896	0.9875	0.9191	0.9225	0.9590	0.9581

In the preliminary investigation described in Sec. 2.5.1 the mesh dependence of the fatigue crack propagation problem was checked by means of different discretizations. A ratio $\delta_0/c \approx 8.12$ between the separation lenght δ_0 and the cohesive element length c was chosen, so that it was possible to resolve the cohesive behavior. The mesh was constructed with several step down, so that a final ratio between the minimal initial crack lenght $a_{0,min}$ and c was equal to 48. In the region far away from the crack tip, instead, the element size is much bigger, and for this reason the total number of elements is limited to 1661, see Fig. 2.17a. The initial crack lenght could only fall in the range $[a_{0,min}, a_{0,max}]$, which means that the crack tip was always preceded and followed by a sufficiently big region of uniform elements with lenght c. For $a_0 = a_{0,min}$, for instance, the number of elements before the crack tip was equal to 8. Another much finer mesh with $a_{0,min}/c \approx 26000$ was also tested, see Figs. 2.17b-d. It was not possible, however, to fit a Paris law in this case, as all the elements after the first one had failed, started failing after few cycles or portion of cycle, with a linear trend in the $a - N$ plane. It was concluded that the ratio $a_{0,min}/c$ may affect the model, causing the Paris law not to emerge.

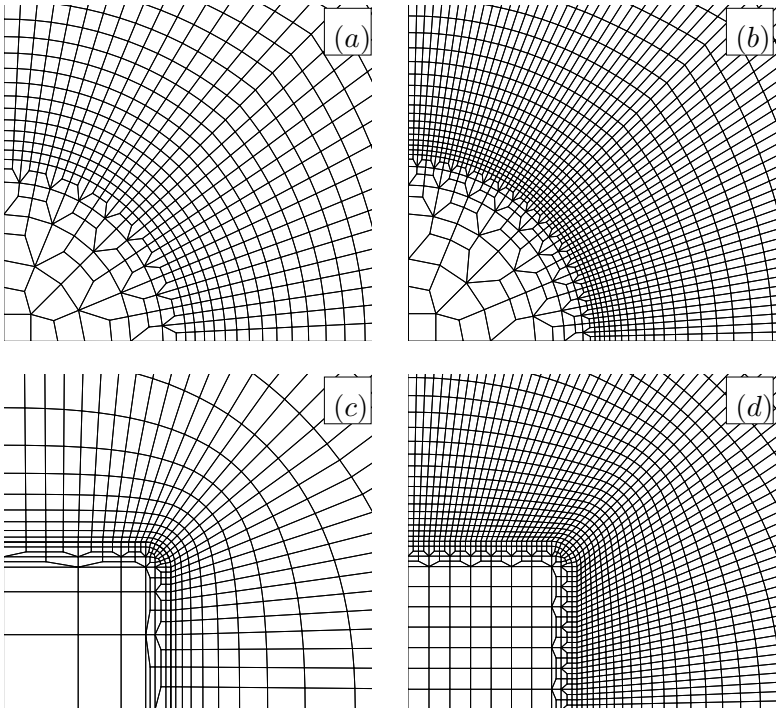

Figure 2.16: A zoom view of the meshes used for the analyses in [P3] , (a) and (c), and the refined meshes used in the convergence study (b) and (d), where the number of elements along the particle was doubled to 128 elements.

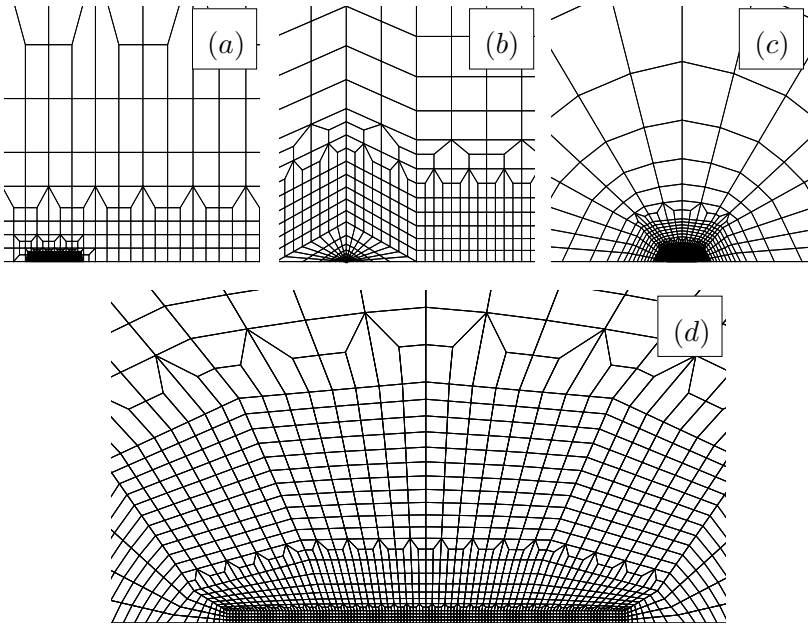

Figure 2.17: Detail of (a) the mesh used in [P4] for the test case, and (b)-(d) different zoom views of another much finer mesh tested.

Chapter 3

Summary of Results

3.1 The Dang Van criterion applied on a roller bearing [P1] -[P2]

The Dang Van criterion has been applied to the rolling contact problem and for the geometry previously described in Sec. 2, considering three different load cases, either with only p_H, only p_{EHL} or both p_{EHL} and p_t. The load history has been divided in an adequate number of steps so that the distance travelled between 2 subsequent steps is approximately 3 % of the Hertzian contact width. For each time step, the value of the damage factor $n(t)$ has been calculated, both with the original Dang Van limit curve and with the modified one. The maximum value in time

$$n = \max_t n(t) \tag{3.1}$$

is then chosen as representative for that material point. If this $n < 1$, the prediction is that initiation of fatigue failure will not occur in the material point. The representative points corresponding to the max value of the damage factor are plotted in Figure 3.1, in the Dang Van region, for all the material points in the region analyzed.

In Figure 3.2 the maximum values n are plotted against the distance from the surface. Both safe regions, as described in Sec. 2.3, are used. As we can see, n reaches the highest value in a sub-surface region, between $0.417\,b$ and $0.508\,b$, depending on the load distribution: this is consistent with experimental observations in literature, where many sub-surface initiated failures in bearings for windmill applications are reported. It should be noted that, according to the Hertzian theory, the maximum shear stress (and Von Mises stress) and the maximum orthogonal shear stress, are reached at depth of $0.78\,b$ and $0.5\,b$, respectively (See Fig. 3.3). Thus the Dang Van criterion

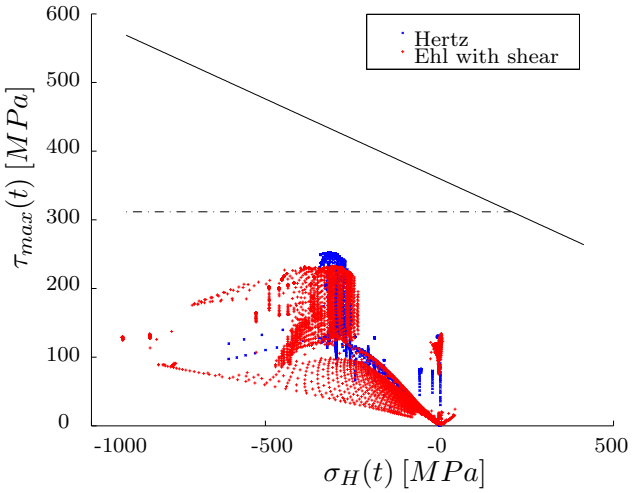

Figure 3.1: A plot of the max Dang Van damage factor in all the integration points in the region analyzed, for Hertzian and EHL load distributions.

predicts a "critical depth" very similar to what expected from the L-P theory, that calculates the fatigue life in rolling contact through the orthogonal shear τ_{xy}, see Sec. 1.3.

For the two EHL load distributions, the peaks reached by the damage factor n are smaller and closer to the contact surface than in the case with the Hertzian pressure distribution. Analogous results are obtained with the use of the original Dang Van safe locus.

The pressure peak used here, $p_0 = 1\ GPa$, results in a stress path that in the Dang Van region is rather close to the modified safe locus. If we consider the curve for the Hertz load in Figure 3.2a, the peak value of the Dang Van damage factor is approximately 0.807, which corresponds to a safety factor of 1.24. This safety factor can be increased by using a smaller value of the pressure peak p_0, a larger length or radius of the roller, or a material more resistant to fatigue. Further calculations, for p_0 equal to 0.8 and 0.5 GPa have been carried out, only for the Hertz distribution, and the results returned values of the safety factor of 1.56 and 2.51, respectively. Therefore the design tool applied here would suggest a pressure peak not bigger than 0.8 GPa in order to have a reasonable safety factor against fatigue failure. In Fig. 3.4 the maximum Dang Van damage factors reached are plotted against the Hertzian maximum pressure p_0 applied, for both the original and the bilinear safe locus. It is possible to notice that an increase in the pressure p_0 from the value of 1 GPa is reflected in an increase of the damage factor that soon reaches the limit curve ($n = 1$). It is here noted that bearings mounted in a wind turbine gearbox are operating at loads

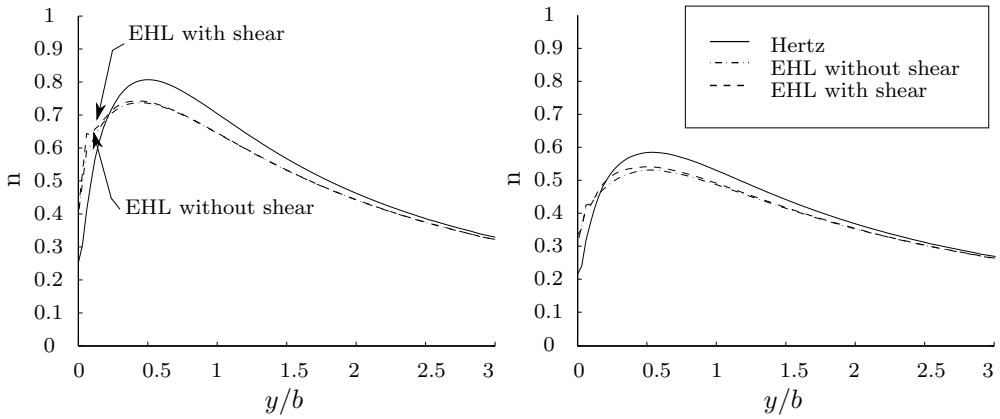

(a) (b)

Figure 3.2: Damage factor versus distance from surface (a) For the bilinear safe locus (b) For the original Dang Van safe locus.

below their dynamic load ratings[1], but they often experience events, such as grid/generator engagements/disengagements, that produce higher contact stresses [31, 37]. It was reported by Rosinski, for instance, that a wind turbine experiences around 15000 overload cycles per year, due to the drive shaft torque oscillations [88]. These overloads can cause misalignments and increase the contact stress in the raceway up to 3–5 GPa, assuming that the load is absorbed elastically. In the practice, part of this load is accomodated plastically, and it is believed that it may be one of the causes of WEA formations [31, 37]. In this analysis the model is fully linear and no plasticity can be accounted for, but it is worth remarking that results returned a safety factor which is close to one, and this considering the material homogeneous with no defects. For a bigger values of the pressure peak, the safety factor according to the Dang Van criterion would fall below one and for further increases the criterion is no more applicable (i.e. a very high number of cycles cannot be sustained).

3.1.1 Hardness variation

The effect of the hardness variation in the inner ring was studied in [P1] [P2] , where different hardness profiles were assumed and the hardness was related to the fatigue limit of the bearing steel. Murakami [9] in fact suggested that the fatigue limit σ_w depends only on the hardness, and not on the microstructure, as also shown in [20], where results for ferritic, perlitic and

[1]The dynamic load rating is defined as that load, constant in magnitude and direction, that corresponds to a basic rating life L_{10} of 10^6 cycles.

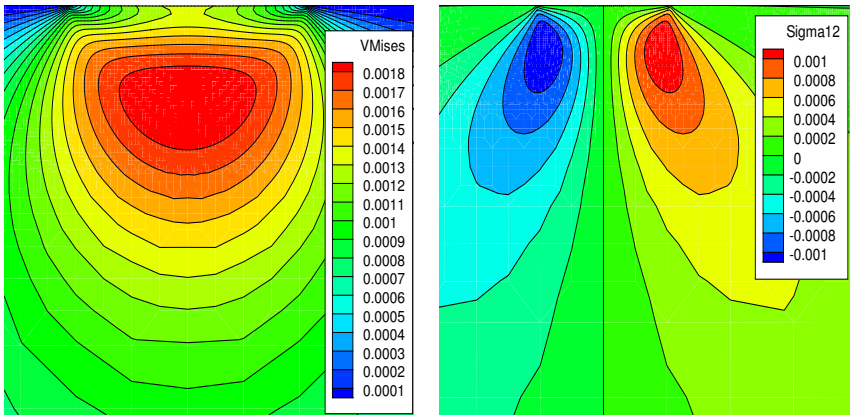

(a) (b)

Figure 3.3: (a) Von Mises and (b) shear stress τ_{xy} under Hertz pressure. Stresses are expressed relatively to the Young modulus E.

martensitic steels were reported.

In order to correlate the hardness to the fatigue limit in pure shear, τ_w, this limit has first been related to σ_{UTS} through an approximate expression proposed in [89] for low-alloy steels:

$$\tau_w = \sigma_w/\sqrt{3} \approx 0.274\,\sigma_{UTS} \tag{3.2}$$

Denoting the Brinell hardness by HB and using an approximate relationship [90]

$$\sigma_{UTS} = 0.0012\,HB^2 + 3.3\,HB \quad [N/mm^2] \tag{3.3}$$

where HB is expressed in N/mm^2, the first coefficient in mm^2/N and the second coefficient is dimensionless, an approximate final relation between τ_w and HB can be written as

$$\tau_w = 0.274\left(0.0012\,HB^2 + 3.3\,HB\right) \quad [N/mm^2] \tag{3.4}$$

Both σ_{UTS} and τ_w in previous equations are expressed in MPa. This procedure was first suggested by Donzella et al. [91, 92]. In the following we assume that the fatigue limit τ_w is given by the expression (3.4). If another expression $\tau_w(HB)$ applies for a material, this will not in principle change the procedure. In fact, all we need is the value of τ_w in each material point of the solid analyzed.

Different hardness distributions along the depth have been studied here. Thus the value of τ_w corresponding to the value of the hardness at that depth has been imposed in the material for each Gauss integration point.

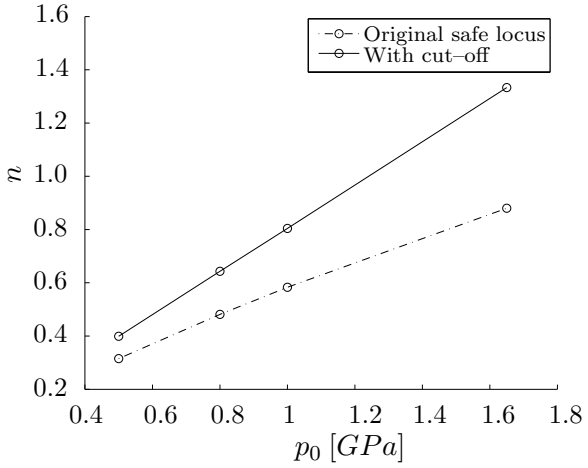

Figure 3.4: The Dang Van damage factor n as a function of the maximum Hertzian pressure applied p_0, for the two different safe loci.

The two different hardness distributions imposed here in the subsurface region of the inner ring and the correspondent τ_w distributions are shown in Figure 3.5a and 3.5b. At distances greater than 1 mm from the surface, HB, for both the distributions, is taken to be constant, at a value such that the related fatigue limit, $\tau_w = \tau_w(HB)$, is approximately 360 MPa. This assumption is equivalent to considering how the effect of a surface hardening process would benefit the fatigue response of the bearing. A recent work by Santos et al. [93] seems to indicate an improvement of fatigue strength, for $AISI$ 52100, by induction heating and repeated quenching, thus validating this assumption. In [93], measuraments presented show a similar step-like hardened profile, with the same peak of hardness here used in Figure 3.5a-b. Also, fatigue tests performed seem to indicate a similar fatigue limit in pure torsion for the untreated steel and, moreover, an increase of this value after the hardening treatment. It may be noted also that some steels show a maximum for the curve $\tau_w(HB)$, which would limit the applicability of Eq. (3.4). In fact, Eq. (3.4) is valid only for smaller values of hardness.

Results show that the values of the damage factor n and the depth at which the maximum n is reached, are strongly dependent on the particular distribution of hardness imposed (Figure 3.6). For all the cases analyzed, the peak of the n-curve shifts away from the surface of the inner ring and, for the cases shown in Figs. 3.5a and 3.5b, the peak values of n are smaller than the corresponding peaks for a material with uniform hardness. In other words, the rings with extra surface hardening have higher safety against fatigue failure. It should also be noted that the maximum Dang Van damage factor is reached, for the cases analyzed, at the interface between the hardened case

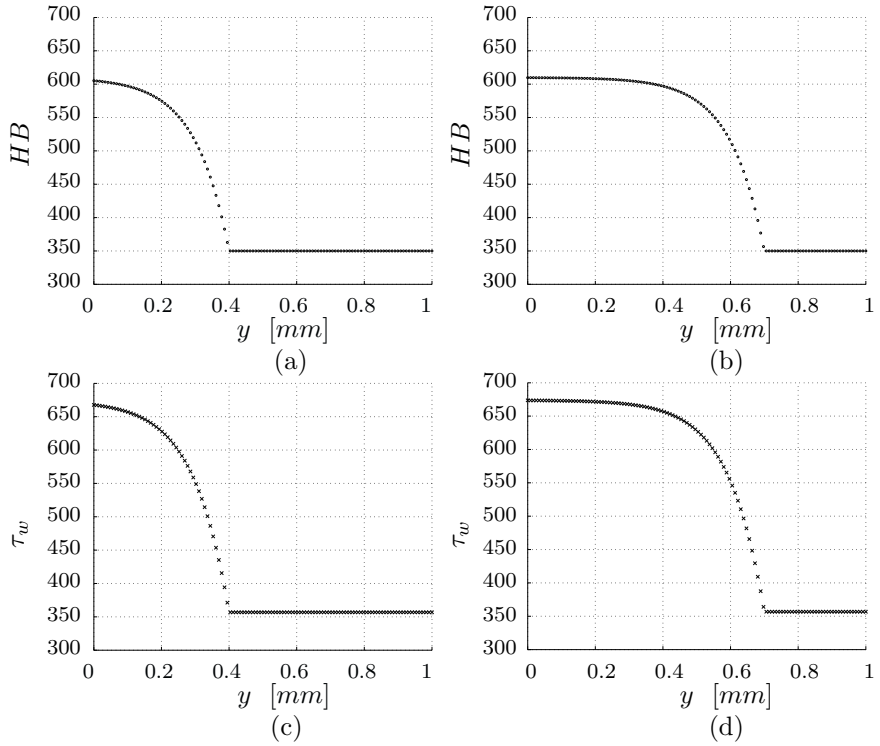

Figure 3.5: (a)-(b) Hardness profiles and (c)-(d) correspondent values of τ_w in the first millimeter of depth. Computations were carried out for $r = 100\ mm$, $R = 200\ mm$, $t_k = 19\ mm$, $R_{roll} = 21\ mm$, $\alpha = 5°$. The Hertzian contact area was $b \approx 0.334\ mm$.

and the untreated, softer core material, which is a well known critical site for subcase failures.

3.1.2 Effect of residual stresses

In order to analyze the influence of pre-existing stresses in the bearing, a typical residual stress distribution for the ring has been considered. It is here noted that the Dang Van criterion can only be applied if the residual stresses are pre-existing to the fatigue process, e.g. due to the machining or the heating process. In this paper it is assumed that the residual stresses are the results of the heat treatment process or diffusion hardening when, during the cooling of the component, the material experiences a volume increase due to the phase transformation from austenite to martensite. As the fast cooling, and therefore the phase transformation, starts from the surface and proceeds toward the bulk material, a compressive residual stress distribution is obtained, as the material close to the surface cannot expand as it wishes, constrained by the material below. The bearing with an assumed residual

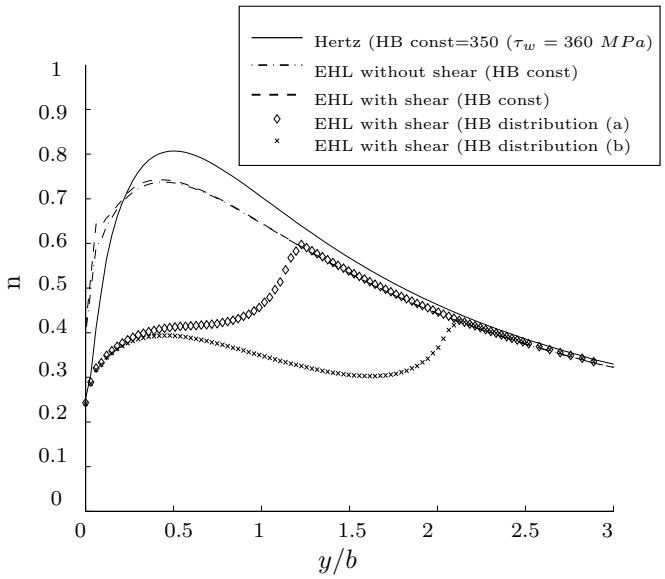

Figure 3.6: Dang Van damage factor versus distance from surface, as results from different load conditions and different variations described in Fig. 3.5. Bilinear safe locus for the Dang Van criterion is here used.

stress distribution, equilibrated by an elastic step calculation, is subsequently subjected to the stresses caused by the contact with the roller. The results obtained with the Dang Van criterion are then compared with the results obtained in the bearing free of residual stresses.

In Figure 3.7 the convention used to name the residual stresses is clarified, while, in Figs. 3.8, the residual stress distribution assumed, in terms of principal stresses, is plotted versus the distance from the surface. Far away from the surface, the residual stresses are assumed to be constant and near zero. The distribution was inspired by experimental results obtained by

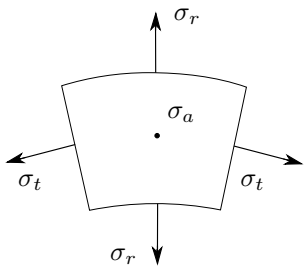

Figure 3.7: Convention used for the principal stresses in the polar coordinate system.

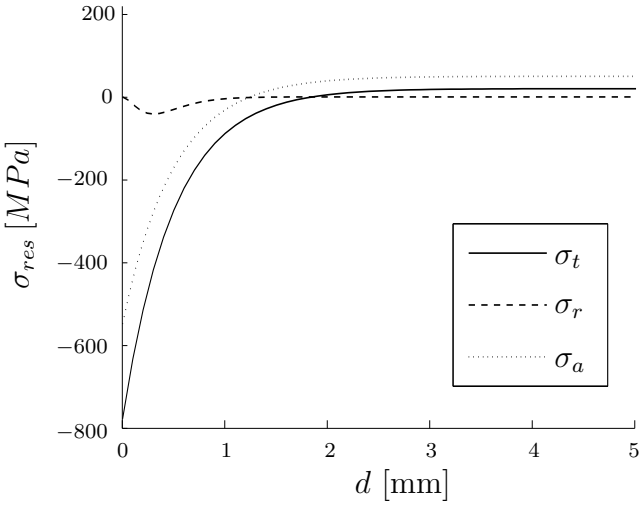

Figure 3.8: Convention used for the principal stresses in the polar coordinate system.

Voskamp [94] for a deep groove ball bearing. The results for the two different safe loci are shown in Figure 3.9. The EHL curves in the figure refer to the EHL pressure distribution where also the effect of shear, p_t, is included. The pre-existing stress state in the inner ring, in the case of the modified safe locus, has no effect, neither positive nor negative (Figure 3.9a). The residual stresses, in fact, result in a simple shift along the σ_H axis in the Dang Van region (Figure 2.6) but this does not change the distance from the limit curve since all the most critical material points are subjected to values of σ_H smaller than σ_A and therefore they are in the region where the limit value for τ_{max} is constant and equal to τ_A. If the original Dang Van limit curve is used instead, the residual stress distribution from Figure 3.8 results in a reduction of the maximum damage factor for the compressive residual stresses (Figure 3.9b) and a shift of the maximum toward the core of the inner race. This is expected for the original Dang Van model, since the reduced value of σ_H will have a beneficial effect, see Figure 2.6.

3.2 The micro-mechanical approach [P3]

Two different macroscopic stress histories, obtained in [P2] and resulting from either the Hertz or the EHL contact pressure distributions in absence of shear load have been applied to the unit cell, for both Al_2O_3 and TiN inclusions (Fig. 1.3). The Dang Van multiaxial criterion was applied to the RVE, assuming that failure would occur only in the matrix.

The results, expressed in terms of the maximum Dang Van damage factor

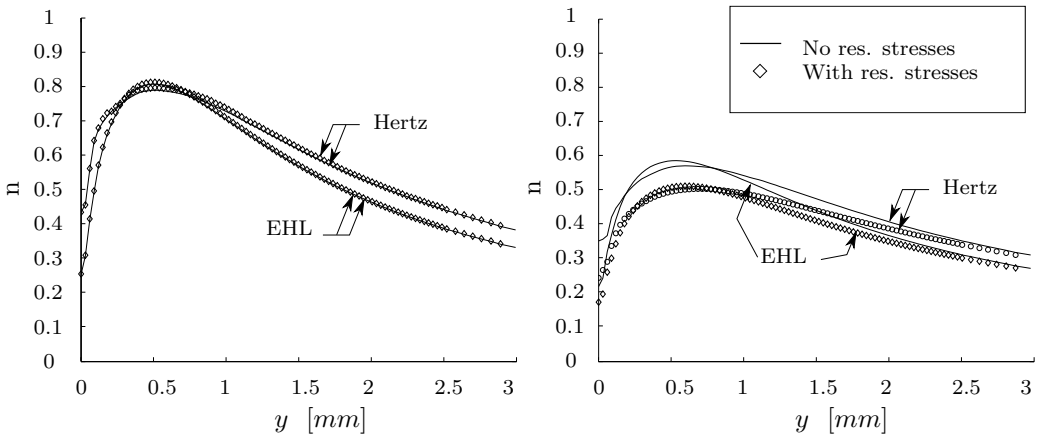

Figure 3.9: Damage factor versus distance from surface: effect of residual stresses. (a) For bilinear limit curve and (b) for original limit curve.

n reached in the matrix, are shown in Fig. 3.10, as function of the volume fraction V_f. For the TiN inclusion, results are also presented as function of the orientation of the inclusion with respect to the inner race surface (see Fig. 2.8). As the analyses carried out are 2D plane strain calculations, volume fractions have been calculated as the ratio between the area of the inclusion, circular for Al_2O_3 and square for TiN, to the area of the cell.

For both the stress histories, regardless of the inclusion type and the volume fraction, the maximum Dang Van damage factor reached in the cell, is always higher than that found in a homogeneous material (macroscopic study) subjected to the same stress history [95] ($n_{max} = 0.78$ for EHL and $n_{max} = 0.81$ for Hertz, respectively). In [95] in fact it was found that for the load analyzed the maximum damage factor in a homogeneous material subjected to the same macroscopic stress histories was always smaller than the limit value 1, thus indicating a safe life for the component according to the cited criterion. The maximum damage factor is here, in some cases, bigger than one, due to the stress concentrations around the particles with higher Young's modulus. But is should be noticed that the values of σ_w and τ_w used in these computations are experimental values that refer to the macroscopic stress state. Corresponding experimental values referring to stresses on the micro-scale would have to be higher. Therefore, it is possible that the cases analyzed here are still in the safe range, even though some of the n-values found in Fig. 3.10 exceed unity. We note that if a smaller maximum n-value, n_{max}, is chosen for a design, e.g. to have a better safety factor, the maximum load carried by the bearing will have to be reduced, or the bearing will have

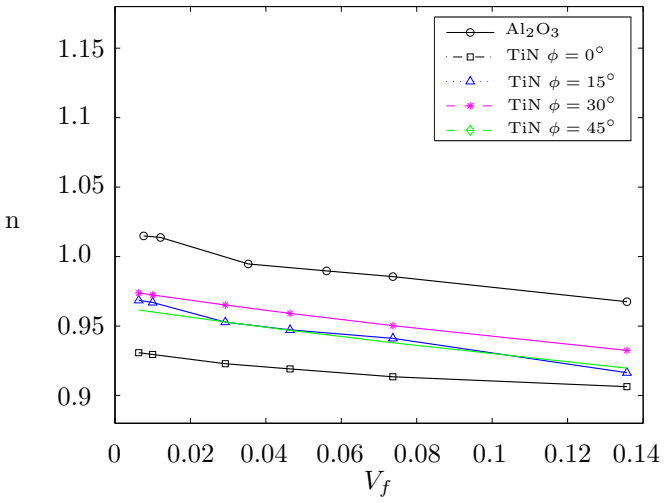

(a)

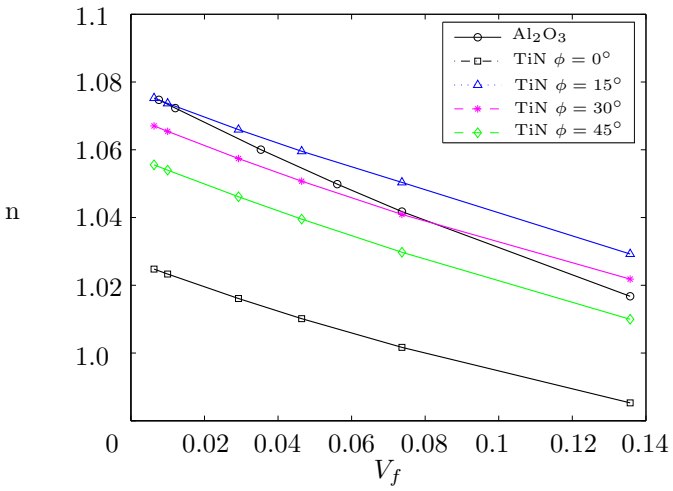

(b)

Figure 3.10: Maximum Dang Van damage factor reached in the matrix, for different inclusions, as function of volume fraction. The load histories applied to the cell result from (a) Hertz contact pressure and (b) EHL contact pressure on the inner race in absence of shear load (See Fig. 1.3).

to be improved. All the curves in Fig. 3.10 show a decreasing trend as function of the volume fraction, such that a safer life corresponds to a bigger inclusion. This prediction may be a result of the inclusions reinforcing the

unit cell, so that a larger inclusion reduces the stress peaks in the matrix.

For both Hertz and EHL stress histories in Fig. 1.3, the curve referring to the Al_2O_3 in the following figures is in most of the cases above the curves for TiN. This is due to the larger difference in Young's moduli for the Al_2O_3 . The shape of the inclusion, and in particular the stress concentration at the TiN corners, is therefore found to be less important than the stress concentration resulting from different material properties between matrix and inclusion. However, the differences are rather small. The rounding radius used here is equal to $\gamma\, l_{cub}$, where $\gamma = 0.15$ and l_{cub} is the half width of the inclusion.

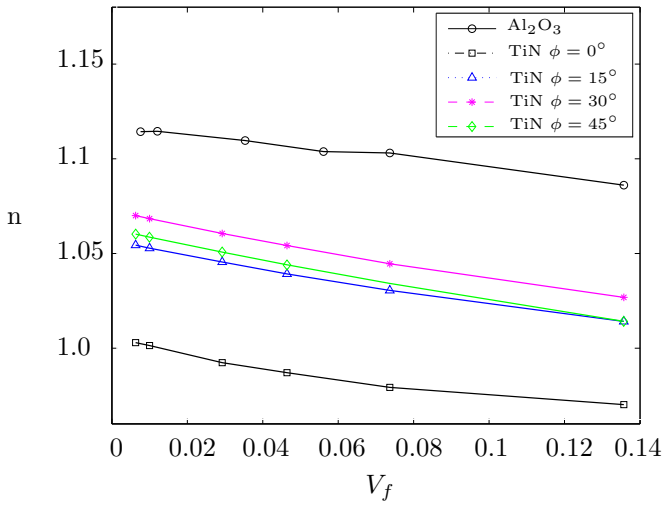

Figure 3.11: Maximum Dang Van damage factor reached in the matrix, for different inclusions, as function of volume fraction. The load history is generated by EHL pressure distribution acting on the inner race, with the shear load.

For a TiN inclusion, the damage factor for ϕ between 15° and 30° degrees is in most cases higher than that for other orientations. This is always true for the EHL load history (Fig. 3.10b) and is true for most of the volume fractions under the Hertz load history (Fig. 3.10a). Apparently this particular orientation is the most dangerous for this kind of inclusion.

In [95] it was found that a Hertz stress history results in a higher Dang Van damage factor than the EHL distribution. In the present study, instead, all the curves from Hertz load history in Fig. 3.10a fall below the corresponding curves for EHL history in Fig. 3.10.

To investigate the effect of the shear load, the results for the case of the EHL load history with the shear load p_t are shown in Fig. 3.11. It is noted

that the curves in Fig. 3.11 are similar to the corresponding curves for EHL without shear of Fig. 3.10b. In some cases, as the alumina and the titanium nitride for $\phi = 30°$ and $\phi = 45°$, the shear load increases the maximum damage factor, while the opposite happens for the other curves. The orientations $\phi = 15°$ and $\phi = 30°$ are still the most dangerous, though the one for $\phi = 45°$ is here comparable. Differences between the corresponding curves for the case that incorporates or neglects the shear are rather small, with the exception of the alumina. Thus, accounting for a shear load due to EHL has only a small effect.

A stress history corresponding to the variable radial load that is experienced by the raceway, as described in 2.2.1, was applied to the RVE. Only the volume fraction $V_f = 0.012$ was investigated, for both alumina and titanium nitride, for which the two cases $\phi = 0°$ and $\phi = 30°$ were considered. Results showed differences only from the 4th decimal digit.

3.2.1 Distribution of the damage factor in the cell

In Fig. 3.12 the contour plot for the Dang Van maximum damage factor is shown, for an alumina inclusion with $V_f = 0.012$, for two different stress histories. In Fig. 3.12a it is seen that the Hertzian load history results in a completely symmetric distribution, with small zones of high damage factor located at the inclusion–matrix interface, at the intersection with the two axes of symmetry. The highest damage factor is reached at $\delta = \pm 11.8°$, in a region almost parallel to the rolling direction. The same values are reached in the symmetric lower half part of the cell. In fig 3.12b, which refers to an EHL stress history in absence of shear load, the symmetry of the contour is lost. The maximum damage factor is still located at the interface with the inclusion, but it is reached at an angle of $\delta = 84.9°$. The areas of high damage factor are still close to the interface, but they are a bit rotated and located in a band approximately oriented at 45° to the overall rolling direction, see Fig. 3.12b. This result seems to indicate that in this direction, failure is more likely to occur. Rather small differences in the damage factor distribution have been found for EHL stress history with or without shear load and therefore in the following figures we will refer to the case which includes the shear. Furthermore, as failure is assumed to happen in the matrix rather than in the inclusion, contour plots are only presented for the matrix. Analyses for different values of the volume fraction V_f show distributions of the damage factor n around the particles similar to those shown in Fig. 3.12.

In Fig. 3.13 the Dang Van damage factor for material points at the matrix-inclusion interface is plotted versus the angle δ for the case of an alu-

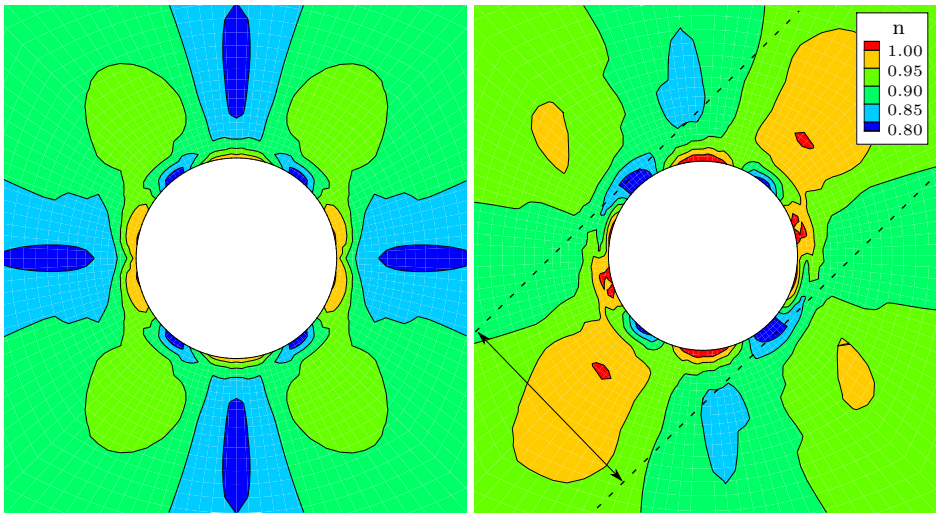

(a) (b)

Figure 3.12: Maximum Dang Van damage factor distribution in the matrix (a) Hertz (b) EHL without shear load. $V_f = 0.012$. A zoom at center of cell.

mina particle and for the hertz history. In the same figure, as a comparison, a damage factor according to a modified Goodman diagram is also plotted. A fully-reversed uniaxial cyclic stress is obtained from the equivalent effective mean and amplitude values of the principal stresses [53]

$$\begin{aligned} \sigma_{eq,m} = & \frac{1}{\sqrt{2}}\sqrt{(\sigma_{I,m}-\sigma_{II,m})^2+(\sigma_{II,m}-\sigma_{III,m})^2+(\sigma_{I,m}-\sigma_{III,m})^2} \\ \sigma_{eq,a} = & \frac{1}{\sqrt{2}}\sqrt{(\sigma_{I,a}-\sigma_{II,a})^2+(\sigma_{II,a}-\sigma_{III,a})^2+(\sigma_{I,a}-\sigma_{III,a})^2} \end{aligned} \tag{3.5}$$

and it is so compared with the linear safe locus

$$\sigma_a = \sigma_w\left[1-\frac{\sigma_{eq,m}}{\sigma_{UTS}}\right] \tag{3.6}$$

where σ_w is the fatigue limit, $\sigma_{eq,m}$ is the effective mean stress and σ_{UTS} is the tensile strength, considered here equal to σ_y. The damage factor n_{Good} is evaluated as distance from the safe locus, in analogy to the Dang Van damage factor n. Beside the relative ratio n/n_{Good}, it is here interesting to note that the absolute and relative maxima are reached approximately at the same angles, for both cases.

In Fig. 3.14 the results for a TiN inclusion with $V_f = 0.01$ and $\phi = 0°$ are shown. As for alumina, the zone of highest damage factor is found at the interface between the inclusion and the matrix, or very close to it. For the Hertzian stress history the highest Dang Van damage factor is reached in the zones that start from the four corners of the inclusion (Fig. 3.14a), while

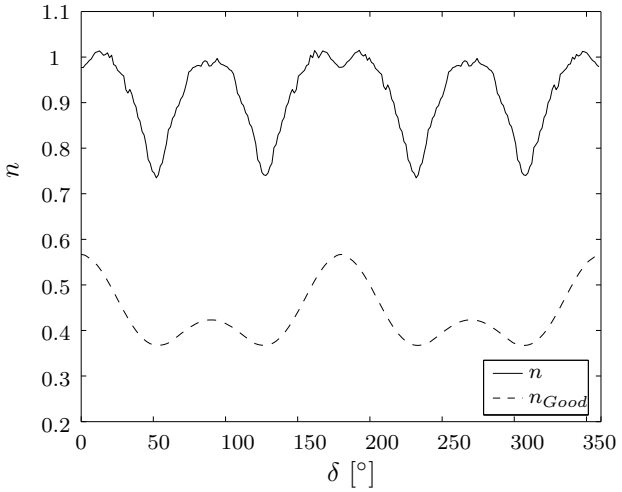

Figure 3.13: The damage factor for the equivalent Goodman criterion and for the Dang Van criterion versus the angle δ. Values refer to material points at the interface between the matrix and an alumina particle, in a RVE subject to a Hertzian load history.

for the EHL stress history it is reached close to the rounding radius of the inclusion. However differences between the highest n and the sourrounding zones, for both cases, are small, thus indicating that stress concentration dominates. If the RVE is subjected to the EHL load history, a zone with high damage factor is found in a band approximately oriented at 45°, as already seen for the alumina.

As the angle ϕ that defines the orientation of the inclusion increases, for Hertzian stress history, the max n is reached at the interface with the inclusion, at all 4 corners (Fig. 3.15). For the EHL stress history, instead, only the corners in the first and third quadrant have very high values of n. These peaks are however highly localized and zones of high Dang Van damage factor are still found close to the other two corners.

The maximum von Mises stress, for the alumina, is reached, in the case of Hertzian stress history, at the time step 90 in Fig. 1.3, i.e. when the roller is exactly above the inclusion and $\Sigma_{12} = 0$. For the EHL stress history without shear load, instead, the maximum von Mises stress is reached at a time which depends on the inclusion size but which is always very close to time step 108 in Fig. 1.3, i.e. when the macroscopic shear stress is close to its negative maximum. Analogous considerations can be made for the titanium nitride inclusion.

In the case of a stress history that accounts for the shear load on the inner race, results are similar to those found in absence of shear load. The maximum von Mises stress is reached typically at time step 109 in Fig. 1.3, both

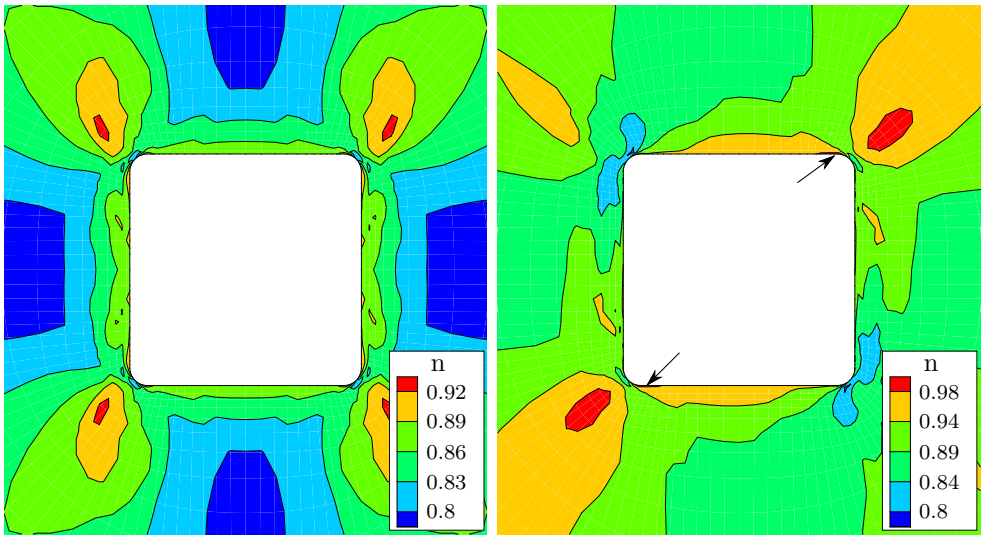

(a) (b)

Figure 3.14: Dang Van maximum damage factor for a TiN inclusion for (a) Hertz and (b) EHL stress history with shear load. $\phi = 0°$, $V_f = 0.01$. In (b) arrows indicate zones where the highest values of n are reached. A zoom at center of cell.

for alumina inclusions and for titanium nitride inclusions. Small variations are due to different orientations of the inclusions. The maximum von Mises stress ranges, for alumina, are between $0.24\,\sigma_y$ and $0.40\,\sigma_y$, depending on the volume fraction and on the stress history applied; for TiN, the effective stress range from $0.32\,\sigma_y$ to $0.33\,\sigma_y$. The value used here for σ_y is 1960 MPa [14].

3.3 Fatigue crack growth [P4]

As also mentioned in Sec. 1, fatigue cracks in materials subject to rolling contact in the very high cycle regime, usually nucleate at matrix-inclusion interface, as result of the stress concentration effect due to the material properties mismatch. It is more likely, in fact, that a crack develops close to an inclusion, where the stresses amplitudes are greater and there are more chances that some less favourably oriented grain acts as crack initiation sites. Cracks may nucleate at the matrix-inclusion interface, and then develop radially, in a direction which is often approximately oriented at 45° with respect to the rolling surface. Sometimes, the crack nucleation also involves some partial debonding of the inclusion from the matrix [17]. The crack initiation process, that may take as long as 95% of the fatigue life N_f [53], is not addressed in the results presented here, and neither the effects of inhomogenities at grain scale. Instead, the material in the matrix is modelled as homogeneous, and

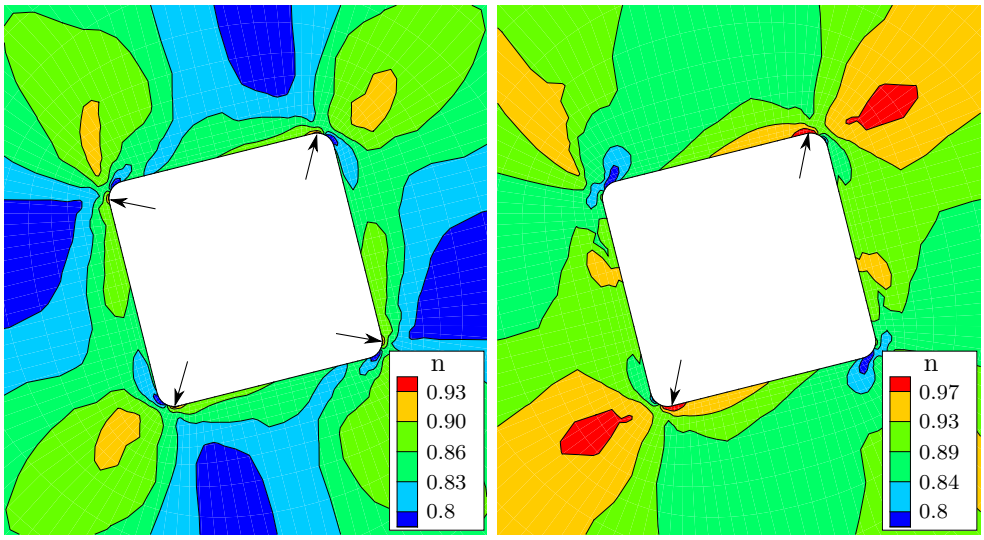

(a) (b)

Figure 3.15: Dang Van maximum damage factor for a TiN inclusion for (a) Hertz and (b) EHL stress history with shear load. $\phi = 15°$, $V_f = 0.01$. Arrows indicate zones where the highest values of n are reached. A zoom at center of cell.

only the fatigue crack growth of a pre-existing crack assumed to have nucleated in the matrix, is investigated.

Some preliminary results [P4] in terms of crack lenght and number of cycles applied are shown in Figs. 3.16-3.17, for the three cases described in Sec. 2.5.2, "CRC", "INT" and "POR", and for a depth corresponding to the maximum Dang Van damage factor (HDV). In Fig. 3.16 (CRC) the results obtained with two different values δ_0 are presented, $\delta_0 = 0.5\ \mu m$ (3.16a) and $\delta_0 = 0.05\ \mu m$ (3.16b), respectively. The value of a_0 is here 1.5 μm. It is clear that the smaller value of $\delta_0 = 0.05\ \mu m$, i.e. a stiffer cohesive traction-separation law, corresponds to a quicker propagation of the crack, regardless of the angle. The cracks oriented at angles $\theta = 0°$ or $\theta = 30°$ have the fastest propagation (Fig.3.16a), though differences with other angles are small. This seems to be confirmed also in Fig. 3.16b, where only angles smaller than 45° propagated within 60 cycles. Figures 3.17a-b, that refer to cases INT and POR, respectively, show the same trend for different angles of the crack: the crack growth is slightly slower than the case CRC, and only the crack oriented at 90° seems to propagate considerably slower. All the results show "S-shaped" curves and this is in contrast what was expected, i.e. greater crack growth rates for longer cracks. The author believes that this may be due to the small size of the fine mesh region where the cohesive elements are placed, and to the big element size step up from that region to the edges of

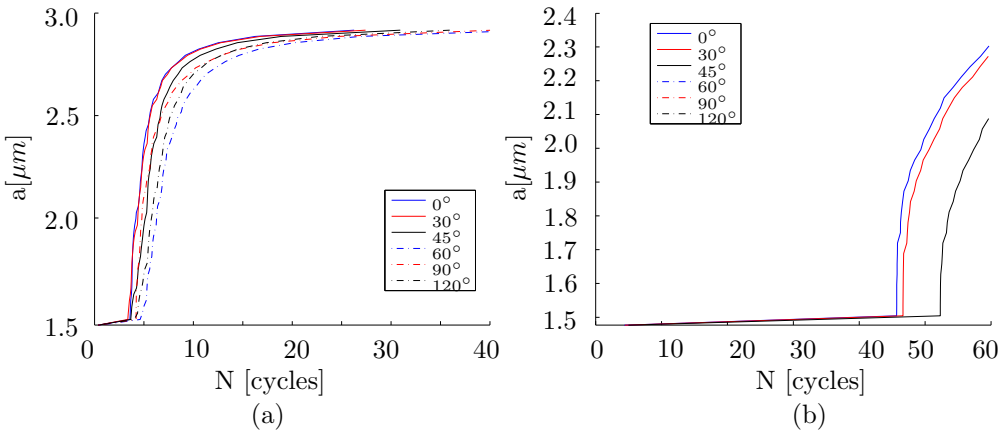

Figure 3.16: Crack length evolution for the "CRC" case, from [P4] , assuming (a) $\delta_0 = 0.05\ \mu m$ and (b) $\delta_0 = 0.5\ \mu m$. In (b) only cracks with angles between 0° and 45° propagated within 60 cycles.

the RVE, where the element size is much bigger. In order to improve the understanding, further investigations were carried out, where the jump-to procedure described in Sec. 2.5.2 and an improved damage rate constitutive law were adopted, see Eq. (2.38).

In Figs. 3.18-3.19 the crack lenght a is plotted versus the number of cycles N, for different crack angles θ and for the different stress histories, (a) HDV, (b) HVM and (c) HTAU, as described in Sec. 2.5.2. A value of $a_0 = 2.97\ \mu m$ was here assumed. In Fig. 3.18 the results for the case CRC are presented. As shown in the figure, the crack growth rates once the first element has failed at a number of cycles N_1 are similar, while a sensible difference can be found in the values of N_1 for different angles. The crack grow rate da/dN is always higher in the HDV case than for HVM and HTAU. For instance, for $\theta = 0°$, the crack growth rates between the first and second element are equal to $(da/dN)_{HDV} \approx 5 \cdot 10^{-9}\ m/cycle$, $(da/dN)_{HVM} \approx 4 \cdot 10^{-9}\ m/cycle$ and $(da/dN)_{HTAU} \approx 2.7 \cdot 10^{-9}\ m/cycle$, respectively.

For an inclusion located at the depth of maximum Dang Van damage factor, Fig. 3.18a, a cracks located at either 0° or 90° starts propagating earlier than other angles. In [21] it was found that the maximum Dang Van damage factor was reached in a material point close to the inclusion–matrix interface and located at an angle θ (δ in [21]) approximately of 11° for a cell subject to the HDV stress histories. Furthermore, in [21] it was also found that a region with a slightly smaller damage factor than the maximum was reached at $\theta = 90°$, see Fig. 3.13. This is in agreement with the results obtained here. On the other hand, a crack located at an angle of $\theta = 45°$, that was also expected to grow faster because of experimental observations

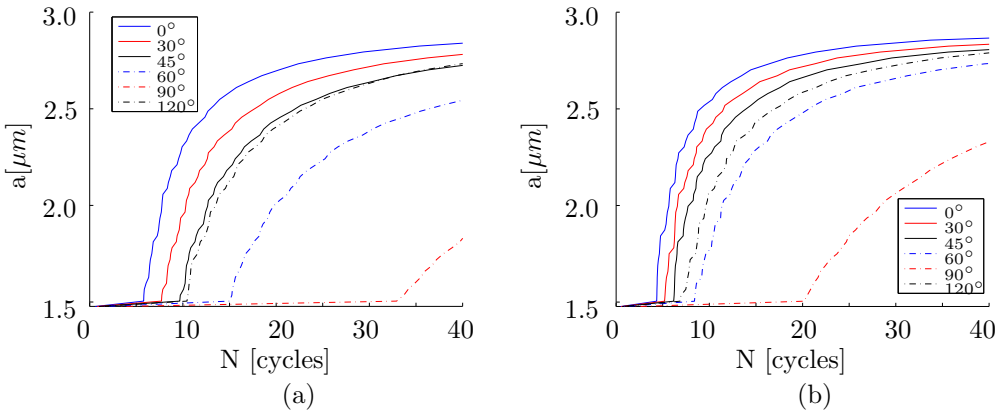

Figure 3.17: Crack length growth for (a) INT and (b) POR cases, from [P4] . $\delta_0 = 0.5\ \mu m$.

found in open literature, represents the safer case, with the biggest value of N_1. However, as said before, the nucleation process is here neglected, and only fatigue growth of cracks with the same initial lenght is investigated. It is thus still possible that $\theta = 45°$ represents a more harmful case. It must also be noted that the jump-to procedure described in Sec. 2.5.2, has been found to underestimate by a factor of approximately 38% the value of N_1 with respect to the same cases without any jump. It was found, however, that the jump procedure preserved the order in which the curves appear on the a-N plane, see Fig. 2.15. In Figs. 3.18b-c it is possible to see that the order of the $a-N$ curves changes for different depths, and it is not possible to find a particular trend that predicts a most dangerous angle θ for any depth. All the curves in Figs. 3.18b-c, however, lie beyond the correspondent curves of Fig. 3.18a, i.e. they have a longer life, which is of particular interest: in fact it suggests that the stress history recorded at a depth of maximum Dang Van damage factor predicts a shorter life than the stress histories of a material point subject to the maximum Von Mises stress or maximum shear stress. The only exception is the case of $\theta = 22.5°$ for HVM, that predicts valus of N approximately 23% smaller than the curve for HDV.

Results in Fig. 3.19 show that for the POR case, i.e. when the inclusion is substitued by a pore, the crack reaches a given lenght before the CRC case at the same angle θ: the fatigue life is shorter. It is also evident from the curves that when the particle is absent in the matrix, the particular depth or, equivalently the particular stress history to which the material point is subject, has little effect on the propagation life.

In Fig. 3.20 the crack propagation for a EHL stress history is compared with results from Hertzian history (see Fig. 3.18a and Fig. 3.19a), which are

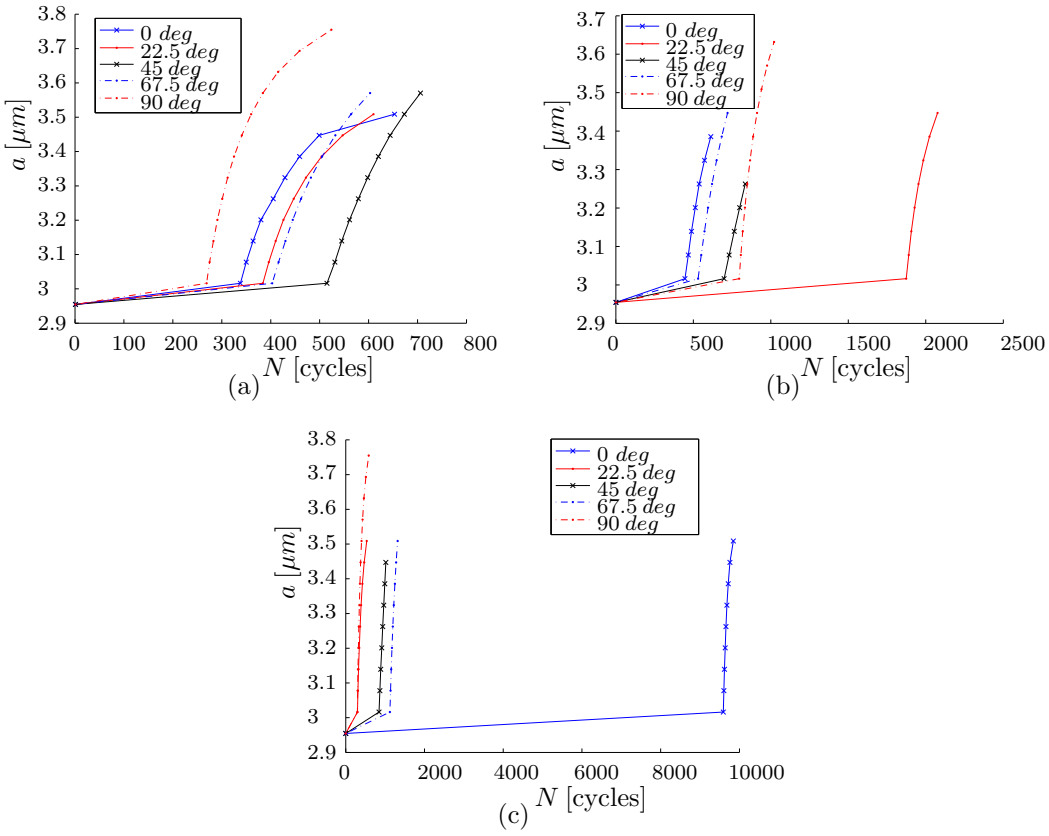

Figure 3.18: Crack length versus the number of cycles for (a) HDV, (b) HTAU and (c) HVM. The curves all refer to the case of an inclusion embedded in the matrix (CRC).

plotted again for convenience. The two stress histories are shown in Fig. 1.3. The computations, carried out for the EHL case and for a smaller number of cycles, show that in all the cases it results in a faster propagation, though the differences are small.

The last results also showed the same shape of the a-N curves as obtained in [P4] , and some considerations have to be made. As the same parameters of the test case were used for these computations, the author believes that it might be due to a shielding effect of the inclusion. In fact, for the test case, the crack growth rate is increasing with the crack lenght as expected, Fig. 2.12. Stresses in a material point decrease with distance from the inclusion, and this may cause the damage rate in the elements following a failed element to be smaller and smaller, as this is function of tractions and opening displacements, see Eq. (2.34). In order to investigate the problem, some computations were runned, for $\theta = 0°$ and $\theta = 90°$ and for the same element size, but with a longer zone where the mesh is highly refined. Thus,

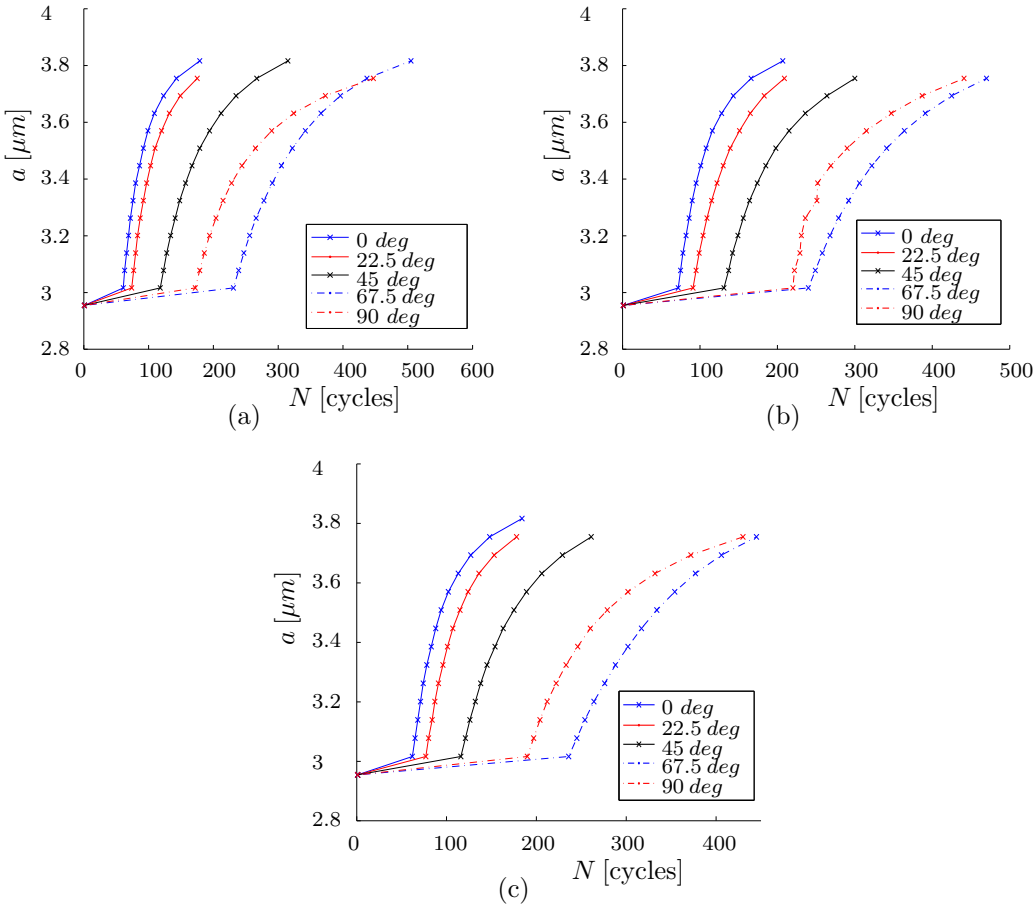

Figure 3.19: Crack length versus the number of cycles for (a) HDV, (b) HTAU and (c) HVM. The curves all refer to the case of a pore embedded in the matrix (POR).

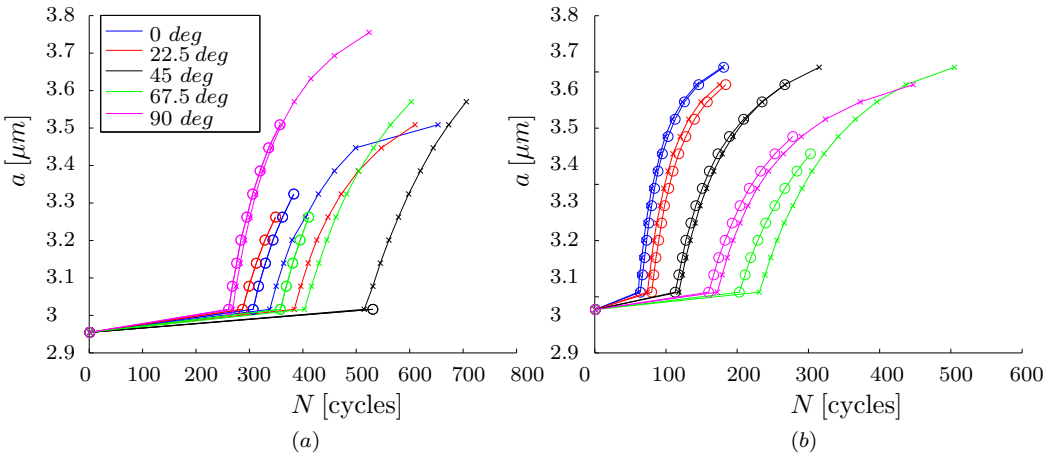

Figure 3.20: Crack propagation curves for (×) Hertzian and (○) EHL stress history. (a) Results for inclusion (CRC) and (b) for a pore (POR).

ahead of the crack tip more elements with size c are present, and therefore the mesh effect, if present, is minimized. Moreover the jump-to procedure was deactivated in this analysis. Three cases were analyzed, with a number of cohesive elements $N_{elm}^{CZ} = 16$ (as previously), $N_{elm}^{CZ} = 48$ and $N_{elm}^{CZ} = 80$, respectively. It was found from Fig. 3.21 that, for the cases with a longer refined mesh zone, the curvature decrease less rapidly, suggesting that there could be also a mesh effect as the mesh size increases very rapidly outside the refined zone. For both the angles $\theta = 0°$ and $\theta = 90°$ it can be also noted that for bigger values of N_{elm}^{CZ} the crack starts propagating at a smaller number of cycles Despite the better results obtained increasing N_{elm}^{CZ}, the calculations become extremely heavier, and computational time is increased as much as a factor of 10. Moreover, it can be seen that the concavity is still present.

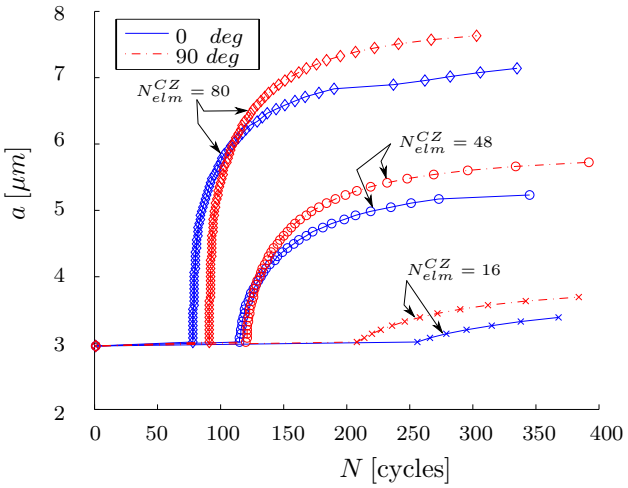

Figure 3.21: Crack length a versus the number of cycles N for different values of N_{elm}^{CZ} and for the crack angles $\theta = 0°$ and $\theta = 90°$.

3.3.1 Variable load

As described in Sec. 2.2.1, it is possible to model the load distribution in a roller bearing and calculate the stress history in a material point in the ring at a particular depth. So far it was always assumed that the stress history applied was constant and corresponding to the maximum load on the roller Q_{max}. However, it has been seen that a roller is loaded by a force $Q(\phi)$ that depends on its angular position ϕ (see Fig. 2.4). In Fig. 3.22 the resulting stress history in a material point located at the maximum Dang Van damage factor depth is plotted. For reference, the stress history corresponding to the maximum load Q_{max} is highlighted. In Fig. 3.23 the fatigue curves for an alumina inclusion subject to the stress history of Fig. 3.22 are plotted. In the

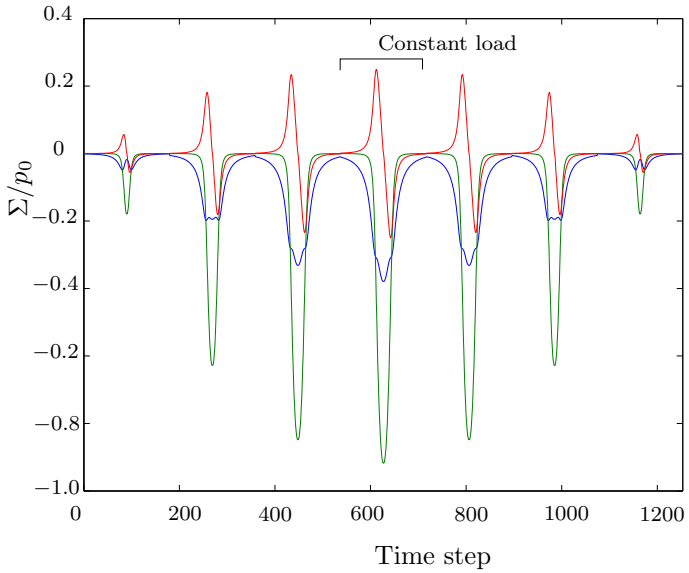

Figure 3.22: Stress history for a material point located at the maximum Dang Van damage factor depth in a bearing ring. The variable load $Q(\phi)$ (see Sec. 2.2.1) acting on the raceway results in different amplitudes of the stress components Σ_{11} (blue), Σ_{22} (green) and Σ_{12} (red) over a complete revolution of the bearing. For comparison the stress history corresponding to the maximum load Q_{max} is also highlighted.

same figure, the curves referring to the stress history caused by a constant load Q_{max} are also depicted. A value of Q_{max} corresponding to a maximum Hertzian pressure $p_0 = 1\ GPa$ has been used here, see Sec. 2.2, Eq. (2.4). It should be noted that, in the case of a variable load, each revolution of the bearing corresponds to the contact of seven loaded rollers (Fig. 3.22), as assumed in Sec. 2.2.1, and therefore a direct comparison cannot be made between the two sets of curves in Fig. 3.23. However, if we multiply the number of cycle N obtained in the case of variable load by a factor of 5.2, the curves almost coincide with the curves obtained for a constant load. This suggests that the beginning and the end of the stress history in Fig. 3.22 have little influence on the crack propagation. Results obtained varing the maximum load Q_{max} are presented in Fig. 3.24, in terms of number of cycle N_1 that are necessary to fail the first cohesive element along the crack front, for a given angle θ. The four different maximum loads are here expressed in terms of the maximum Hertzian pressure p_0, see Eq. (2.4) in Sec. 2.2. Thus the values of p_0 in the figure represent the values of the Hertzian pressure distribution corresponding to the maximum load ($Q(\phi) = Q_{max}$). As expected the curves, in analogy to $S - N$ curves, show that a bigger value of the load applied corresponds to a smaller value N_1 to start the crack propagation. Also it is seen that, among the angles investigated, the angle

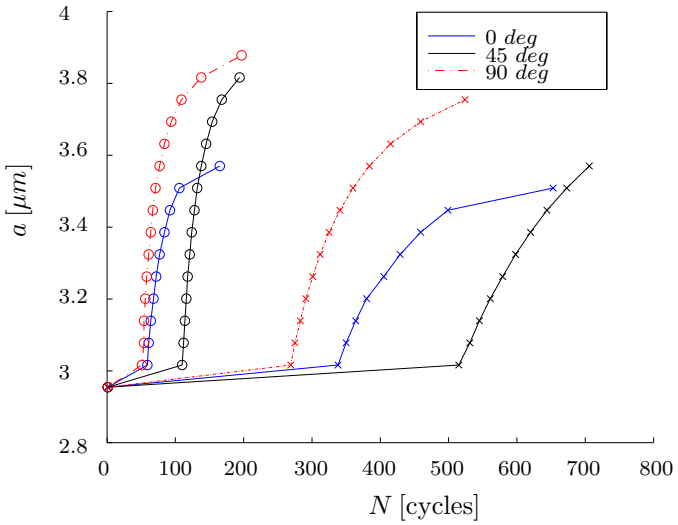

Figure 3.23: Fatigue crack growth at an Al_2O_3 inclusion located at the maximum Dang Van damage factor depth subject to (×) constant or (○) variable load (see Sec. 2.2.1), as in a real bearing. Curves are plotted for crack angles $\theta = 0°$, $\theta = 45°$ and $\theta = 90°$.

$\theta = 90°$ represents the worst case.

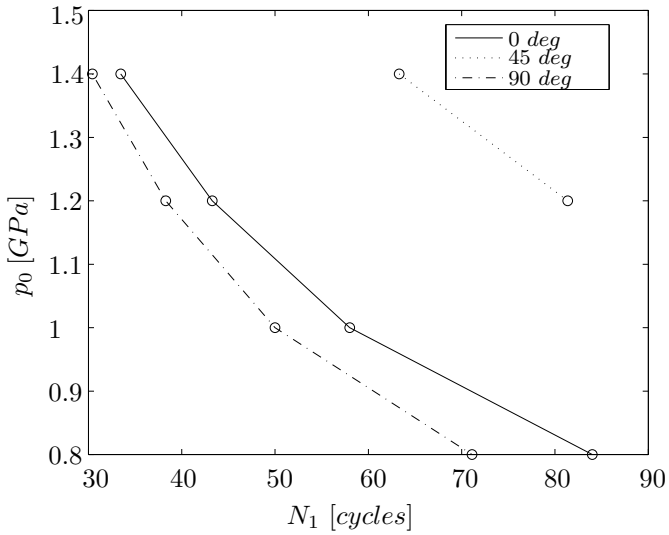

Figure 3.24: Maximum Hertzian pressure in the most loaded roller versus the number of cycles N_1 to fail the first cohesive elements. Curves are plotted for crack angles $\theta = 0°$, $\theta = 45°$ and $\theta = 90°$.

Chapter 4

Conclusions

The goal of the present work was to develop a deeper understanding on failure for rolling contact fatigue. A particular focus was given to failure in roller bearings for windmill application, as the thesis was part of a bigger project called REWIND, aimed to improve the design and the reliability of wind turbines. The outcome of the project includes the present thesis and the 4 research publications [P1] -[P4].

In the first part of the project a 2D plane strain finite element model of a roller bearing was investigated, and results were interpreted in lights of the Dang Van multiaxial fatigue criterion. A modified bilinear safe locus proposed in [52] and predicting a more conservative behavior for high negative hydrostatic stresses was adopted. Both a Hertzian and a elastohydrodynamic lubrication load distribution were investigated and the results were compared. It was found that for a maximum pressure $p_0 = 1\ GPa$, the maximum Dang Van damage factor for the bilinear safe locus in the case of a Hertzian load was reached in the subsurface region and it was approximately $n = 0.807$, corresponding to a safety factor of 1.24. Results obtained for the EHL load were similar, but a smaller damage factor was reached. It has to be noted that even though $p_0 = 1\ GPa$ is a typical nominal pressure for bearings in the gearbox of a wind turbine, much higher pressure peaks can be reached, due for instance to transient phenomena such as grid/generator engagements/disengagements. In these cases very high contact stresses may rise and maximum pressure peaks can reach $3\ GPa$. It is clear then that even if the Dang Van criterion predicts a safe life for an homogeneous material and for Hertzian maximum pressure $p_0 = 1\ GPa$, a higher safefty factor is needed, and therefore a smaller maximum pressure is suggested in the design phase, or a larger bearing. Moreover it has to be noted that the maximum damage factor was reached at a depth very close to $0.5b$, with b the Hertzian half-contact width. Such a critical depth represents also the

depth were the maximum orthogonal shear stress τ_{xy} is reached, and it is at the basis of the well known Lundberg-Palmgren model for bearings life. The influence of a hardness treatment, modelled by imposing an assumed hardness distribution along the depth and relating it to the fatigue limit, was investigated. The hardness treatment, assumed to be beneficial for the fatigue life as reported in [93], resulted in a smaller Dang Van damage factor reached in the subsurface region, with a maximum reached at the interface between hardened material and untreated material. Compressive residual stresses were found to be beneficial for fatigue life (smaller damage factor), but only for the original Dang Van safe locus.

The macroscopic investigation of the roller bearing resulted in some insights, but the safe life predicted by the Dang Van criterion does not match the experimental observations reported in literature that support the belief of no infinite life for such mechanical elements. Moreover, poor lubrication, overloads and inclusion content are just some of the factors that can reduce the fatigue life. The latter is well known to be extremely relevant in the very high cycle regime and in particular in rolling contact, as most subsurface failures are found to nucleate at non-metallic particles, such as alumina, titanium nitride or manganese sulphide. In windmill bearings, typical flaws called "butterflies" or "white etching cracks", also suggest that rolling contact fatigue cannot be really understood without taking into account the effect of inclusions. A micro-mechanical study aimed to investigate the influence of alumina and titanium nitride in a AISI 52100 bearing steel matrix was for this reason carried out. In the study, a single particle was embedded in the matrix, and the RVE was subject to a typical rolling contact stress history as periodic boundary conditions. Both stress histories from a Hertzian and from a elastohydrodynamic lubricated load distribution were applied, and also the volume fraction and the inclusion orientation were investigated. The stress concentration due to the elastic properties mismatch resulted in a higher Dang Van damage factor than for the macroscopic study, and it was shown that the maximum was always reached in the matrix and in a region very close to the inclusion-matrix interface. For the EHL stress history, it was also seen that a high damage factor was also reached, beside the interface, in a characteristic band, oriented at approximately 45° to the rolling direction.

In the last part of the project fatigue crack growth under rolling contact was studied by means of fatigue cohesive elements. The Roe-Siegmund model was adopted and fatigue was simulated by the continous evolution of a damage variable in the cohesive elements. The characteristic parameters of the model were fitted, in a test case, on a Paris law with typical values for a bearing steel and were subsequently used in a micro-micromechanical study,

with an alumina inclusion embedded in a bearing steel matrix. In the RVE, a pre-existing crack was assumed to have nucleated, and only the fatigue crack growth was analyzed. Thus, the nucleation process was not accounted for. Stress histories recorded at different depth were applied as periodic boundary condition and it was found that the depth of maximum Dang Van damage factor was characterized by a faster propagation. Calculations where the inclusion was replaced by a circular pore returned a shorter fatigue life than the case with the inclusion. When the RVE was subject to an EHL stress history, this always resulted in a shorter life compared to the Hertzian load.

Bibliography

[1] Johnson KL. *Contact Mechancs*. Cambridge University Press, Cambridge, 1985.

[2] Littmann WE. The mechanism of contact fatigue. Technical report, NASA, 1970.

[3] Olver AV. The mechanism of rolling contact fatigue: un update. *Proc IMechE Part J: J Engineering Tribology*, 219(J04104):313–330, 2005.

[4] Sadeghi F, Jalalahmadi B, Slack TS, Raje N, and Arakere NK. A review of rolling contact fatigue. *Journal of tribology*, 131(041403):1–15, 2009.

[5] Hertz H. On the contact of elastic solids. *J Reine Angew Math*, 92:156–171, 1882.

[6] Gohar R and Rahnejat H. *Fundamentals of Tribology*. Imperial College Press, London, 2nd edition, 2012.

[7] Lundberg G and Palmgren A. Dynamic capacity of rolling bearings. *Acta Polytech Scand, Mech Eng Ser*, 1(3):7–53, 1947.

[8] Lundberg G and Palmgren A. Dynamic capacity of rolling bearings. *Acta Polytech Scand, Mech Eng Ser*, 2(4):96–127, 1947.

[9] Murakami Y. *Metal Fatigue: Effects of small defects and nonmetallic inclusions*. Elsevier Science, Oxford, 1st edition, 2002.

[10] Murakami Y, Nomoto T, Ueda T, and Murakami Y. On the mechanism of fatigue failure in the superlong life regime ($N > 10^7$ cycles). Part I: Influence of hydrogen trapped by inclusions. *Fatigue Fract Engng Mater Struct*, 23:893–902, 2000.

[11] Murakami Y, Nomoto T, Ueda T, and Murakami Y. On the mechanism of fatigue failure in the superlong life regime ($N > 10^7$ cycles). Part II: A fractographic investigation. *Fatigue Fract Engng Mater Struct*, 23:903–910, 2000.

[12] Murakami Y and Endo M. Effects of defects, inclusions and inhomogeneities on fatigue strength. *International Journal of Fatigue*, 16:163–182, 1994.

[13] Evans M H. White structure flaking (WSF) in wind turbine gearbox beaerings: effects of 'butterflies' and white etching cracks (WECs). *Material Science and Technology*, 28(1):3–22, 2012.

[14] Hashimoto K, Fujimatsu T, Tsunekage N, Hiraoka K, Kida Katsuyuki, and Costa Santos E. Study of rolling contact fatigue of bearing steels in relation to various oxide inclusions. *Materials and Design*, 32:1605–1611, 2011.

[15] Hashimoto K, Fujimatsu T, Tsunekage N, Hiraoka K, Kida Katsuyuki, and Costa Santos E. Effect of inclusion/matrix interface cavities on internal-fracture-type rolling contact fatigue life. *Materials and Design*, 32:4980–4985, 2011.

[16] Evans M H, Richardson, Wang L, and Wood RJK. Serial sectioning investigation of butterfly and white etching crack (WEC) formation in wind turbine gearbox bearings. *Wear*, 302(1-2):1573–1582, 2013.

[17] Grabulov A, Petrov R, and Zandbergen HW. EBSD investigation of the crack initiation and TEM/FIB analyses of the microstructural changes around the cracks formed under Rolling Contact Fatigue (RCF). *International Journal of fatigue*, 32:576–583, 2010.

[18] Nishioka K. On the effect of inclusions upon the fatigue strength. *J. Jpn. Soc. Testing Mater.*, 6(45):382–385, 1957.

[19] Alley ES and Neu RW. Microstructure-sensitive modeling of rolling contact fatigue. *International Journal of Fatigue*, 32:841–850, 2010.

[20] Chalant G and Suyitno BM. Effects of microstructure on low and high cycle fatigue behaviour of a micro-alloyed steel. In *Proc. 6th Int. Conf. Mech. Behav. Mater.*, pages 511–516, Kyoto, 1991. VI.

[21] Cerullo M and Tvergaard V. Micromechanical study of the effect of inclusions on fatigue failure in a roller bearing. *(Submitted)*, 2014.

[22] Kabo E. Material defects in rolling contact fatigue – influence of overloads and defect clusters. *International Journal of fatigue*, 24:887–894, 2002.

[23] Hashimoto K, Hiraoka K, Kida K, and Costa Santos E. Effect of sulphide inclusions on rolling contact fatigue life of bearing steels. *Materials Science and Technology*, 28(1):39–43, 2012.

[24] Nishijima S and Kanazawa K. Stepwise S–N curve and fish-eye failure in gigacycle fatigue. *Fatigue Fract. Eng. Mater Struc*, 22:601–607, 1999.

[25] Shiozawa K, Lu L, and Ishihara S. S-N curve characteristics and subsurface crack initiation behaviour in ultra-long life fatigue of a high carbon-chromium bearing steel. *Fatigue Fract Engng Mater Struct*, 24:781–790, 2001.

[26] Shiozawa K, Morii Y, Nishino S, and Lu L. Subsurface initiation and propagation mechanism in high-strength steel in a very high cycle fatigue regime. *International Journal of Fatigue*, 28:1521–1532, 2006.

[27] Sakai T, Harada H, and Oguma N. Crack initiation mechanism of bearing steel in very high cycle fatigue. In *Proc. 16th European Conference on Fracture (ECF16)*, Alexandroupolis, Greece, 2006.

[28] Chan KS. Roles of microstructure in fatigue crack initiation. *International*

Journal of Fatigue, 32:1428–1447, 2010.

[29] Mitamura N, Hidaka H, and Takaki S. Microstructural development in bearing steel during rolling contact fatigue. *Material Science Forum*, 539-543:4255–4260, 2007.

[30] Hiraoka K, Nagao M, and Isomoto Tatsuro. Study on flaking process in bearings by white etching area generation. *Journal of ASTM International*, 3(6):234–240, 2006.

[31] Kotzalas MN and Doll GL. Tribological advancements for reliable wind turbine performance. *Philos T Roy Soc A*, 368:4829–4850, 2010.

[32] Ebert FJ. Fundamentals of design and technology of rolling element bearings. *Chinese Journal of Aeronautics*, 23:123–136, 2010.

[33] Stadler K and Stubenrauch A. Premature bearing failures in industrial gearboxes - Lagerfrühausfälle in Industriegetrieben. Technical report, SKF GmbH, 2013.

[34] Errichello R, Budny R, and Eckert R. Investigations of bearing failures associated with white etching areas (WEAs) in wind turbine gearboxes. *Tribology Transactions*, 56:1069–1076, 2013.

[35] Brooksbank D and Andrews KW. Stress fields around inclusions and their relation to mechanical properties. *J Iron Steel Inst.*, 210:246–255, 1972.

[36] Oswald FB, Zaretsky EV, and Poplawski JV. Relation between residual and hoop stresses and rolling bearing fatigue life. *Tribology Transactions*, 57:749–765, 2014.

[37] Greco A, Sheng S, Keller J, and Erdemir A. Material wear and fatigue in wind turbine systems. *Wear*, 302(1-2):1583–1591, 2013.

[38] Arabian-Hoseynabadi H, Oraee H, and Tavner PJ. Failure Modes and Effects Analysis (FMEA) for wind turbines. *Int J Electr Power Energy Syst*, 32:817–824, 2010.

[39] Amirat Y, Benbouzid MEH, Al-Ahmar E, and al. A brief status on condition monitoring and fault diagnosis in wind energy conversion systems. *Renewable Sustainable Energy Rev* , 13:2629–2636, 2009.

[40] Blau PJ, Walker LR, Xu H, and al.. Wear analysis of wind turbine gearbox bearings - Final Report. Technical report, Oak Ridge National Laboratory, Oak Ridge, USA, 2010.

[41] Smolders K, Feng Y, Long H, and Tavner P. Reliability analysis and prediction of wind turbine gearboxes. In *EWEC - European Wind Energy Conference*, Warsaw, Poland, 2010.

[42] Fernandes C, Martins RC, and Seabra JHO. Friction torque of cylindrical roller thrust bearings lubricated with wind turbine gear oils. *Tribol Int*, 59:121–128, 2013.

[43] Spinato F and Tavner PJ and van Bussel GJW and Koutoulakos E. Reliability

of wind turbine subassemblies. *IET Renew Power Gener*, 3(4):387–401, 2009.

[44] Yang M and Chengbing H and Xinxin F. Institutions function and failure statistic and analysis of wind turbine. *Physics Procedia*, 24:25–30, 2012.

[45] Ragheb A and Ragheb M. Wind turbine gearboxes technologies. In *Proc. pf the 1st International Nuclear and Reneawble Energy Conference*, Amman, Jordan, 2010.

[46] ISO. ISO 281:2007 Rolling bearings – Dynamic load ratings and rating life. 2007.

[47] Ioannides E and Harris TA. A new fatigue life model for rolling bearings. *Journal of Tribology*, 107:367–377, 1985.

[48] Liu J and Zenner H. *Fatigue limit of ductile metals under multiaxial loading*, pages 147–63. Biaxial/multiaxial fatigue and fracture. Elsevier, Amsterdam, 2003.

[49] Papadopoulos IV. A high-cycle fatigue criterion applied in biaxial and triaxial out-of-phase stress conditions. *Fatigue Fract Eng Mater Struct*, 18:79–91, 1995.

[50] Dang Van K. *Sur la resistance a la fatigue des metaux*. PhD thesis, Scientifique et Technologique l'Armement France, Paris, 1973.

[51] Dang Van K. *Macro-micro approach in High-Cycle Fatigue*, pages 120–130. ASTM STP 1191. ASTM DL McDowell and R Ellis Eds, Philadelphia, 1993.

[52] Desimone H, Bernasconi A, and Beretta S. On the application of the Dang Van criterion to rolling contact fatigue. *Wear*, 260:567–572, 2006.

[53] Suresh S. *Fatigue of materials*. Cambridge University Press, Cambridge, 2nd edition, 2006.

[54] Ciavarella M, Monno F, and Demelio G. On the Dang Van fatigue limit in rolling contact fatigue. *International Journal of Fatigue*, 28:852–863, 2006.

[55] Ciavarella M and Monno F. A comparison of multiaxial fatigue criteria as applied to rolling contact fatigue. *Tribology International*, 43:2139–2144, 2010.

[56] Bernasconi A, Filippini M, Foletti S, and Vaudo D. Multiaxial fatigue of a railway steel under non-proportional loading. *International Journal of Fatigue*, 28:663–672, 2006.

[57] Chen Q, Shao E, Zhao D, Guo J, and Fan Z. Measurement of the critical size of inclusions initiating contact fatigue cracks and its application in bearing steel. *Wear*, 147:285–294, 1991.

[58] Raje N, Sadeghi F, and Rateick RG Jr. A statistical damage mechanics model for subsurface initiated spalling in rolling contacts. *Journal of Tribology*, 130(042201):1–11, 2008.

[59] Slack T and Sadeghi F. Explicit finite element modeling of subsurface initiated spalling in rolling contacts. *Tribology International*, 43:1693–1702, 2010.

[60] Jalalahmadi B and Sadeghi F. A Voronoi FE fatigue damage model for life

scatter in rolling contacts. *Journal of Tribology*, 132(021404):1–14, 2010.

[61] Weinzapfel N, Sadeghi F, and Bakolas V. An approach for modeling material grain structure in investigations of hertzian subsurface stresses and rolling contact fatigue. *Journal of Tribology*, 132(041404):1–12, 2010.

[62] Slack T and Sadeghi F. Cohesive zone modeling of intergranular fatigue damage in rolling contacts. *Tribology International*, 44:797–804, 2011.

[63] Warhadpande A, Sadeghi F, Kotzalas MN, and Doll G. Effects of plasticity on subsurface initiated spalling in rolling contact fatigue. *International Journal of Fatigue*, 36:80–95, 2012.

[64] Weinzapfel N and Sadeghi F. Numerical modeling of sub-surface initiated spalling in rolling contacts. *Tribology International*, 59:210–221, 2013.

[65] Bomidi JAR, Weinzapfel N, Sadeghi F, Liebel A, and Weber J. An improved approach for 3D rolling contact fatigue simulations with microstructure topology. *Tribology Transactions*, 56(3):385–399, 2013.

[66] Paulson NR, Bomidi JAR, Sadehi F, and Evans RD. Effects of crystal elasticity on rolling contact fatigue. *International Journal of Fatigue*, 61:67–75, 2014.

[67] Jacobson BO and Hamrock BJ. Non-newtonian fluid model incorporated into elastohydrodynamic lubrication of rectangular contacts. *J Tribol*, 106:275–282, 1984.

[68] Professor Klit P and Janakiraman S. Private communication.

[69] Harris TA and Kotzalas MN. *Essential concepts of bearing technologies*. Taylor & Francis Group , Boca Raton, 5th edition, 1985.

[70] Sjövall H. The load distribution within ball and roller bearings under given external radial and axial load. *Tek Tidskr Mek*, h(9), 1933.

[71] Nagatomo T, Takahashi K, Okamura Y, Kigawa T, and Noguchi S. Effects of load distribution on life of radial roller bearings. *Journal of Tribology*, 134(2):021101–1–021101–7, 2012.

[72] Sines G. *Behaviour of metals under complex static and alternating stresses*, pages 145–169. Metal fatigue. McGraw-Hill, New York, 1959.

[73] Davoli P, Bernasconi A, Filippini M, and Papadopoulos IV. Independence of the torsional limit upon a mean shear stress. *Int J Fatigue*, 25(6):471–480, 2003.

[74] Heywood RB. *Designing against fatigue*. Chapman and Hall Ltd., London, 1962.

[75] Dalan TJ. *Stress Range*. Horger OJ (Ed). ASME Handbook Metal Engineering Design, New York, 1953.

[76] Lai J, Lund T, Rydn K, Gabelli A, and Strandell I. The fatigue limit of bearing steels – Part I: A pragmatic approach to predict very high cycle fatigue strength. *Int Journal of Fatigue*, 37:155–168, 2012.

[77] Tvergaard V. Effect of stress-state and spacing on voids in a shear-field. *International Journal of Solid and Structures*, 49(22):3047–3054, 2012.

[78] Roe KL and Siegmund T. An irreversible cohesive zone model for interface fatigue crack growth simulation. *Engineering fracture mechanics*, 70(2):209–232, 2003.

[79] Siegmund T. A numerical study of transient fatigue crack growth by use of an irreversible cohesive zone model. *International Journal of Fatigue*, 26:929–9392, 2004.

[80] Wang B and Siegmund T. Numerical simulation of constraint effects in fatigue crack growth. *International Journal of Fatigue*, 27:1328–1334, 2005.

[81] Wang B and Siegmund T. Simulation of fatigue crack growth at plastically mismatched bi-material interfaces. *International Journal of Plasticity*, 22:1586–1609, 2006.

[82] Brinckmann S and Siegmund T. Computations of fatigue crack growth with strain gradient plasticity and an irreversible cohesive zone model. *Engineering Fracture Mechanics*, 75:2276–2294, 2008.

[83] Jha D and Banerjee A. A cohesive model for fatigue failure in complex stress-states. *International Journal of Fatigue*, 36:155–162, 2012.

[84] Lemaitre Jean. *A course on Damage Mechanics*. Springer, Berlin, 1996.

[85] Beswick JM. Fracture and Fatigue crack propagation properties of hardened 52100 steel. *Metallurgical Transactions A*, 20A:1961–1973, 1988.

[86] Stanzl-Tschegg and Schonbauer B. Near-threshold fatigue crack propagation and internal cracks in steel. *Procedia Engineering*, 2(1):1547–1555, 2010.

[87] Tvergaard V and Hutchinson J. Microcrackig in ceramics induced by thermal expansion or elastic anisotropy. *J Am Ceram Soc*, 71(3):157–166, 1988.

[88] Rosinski J and Smurthwaite D. Troubleshooting wind gearbox problems. *Gears Solutions*, 8:22–33, 2010.

[89] Atzori B, Meneghetti G, and Susmel L. Material fatigue properties for assessing mechanical components weakened by notches and defects. *Fatigue Fract Eng Mater Struct*, 28:83–97, 2005.

[90] Roessle ML and Fatemi A. Strain-controlled fatigue properties of steels and some simple approximations. *Int J Fatigue*, 22:495–511, 2000.

[91] Donzella G and Petrogalli C. A failure assessment diagram for components subjected to rolling contact loading. *International Journal of Fatigue*, 32:256–268, 2010.

[92] Donzella G, Petrogalli C, and Mazzù. Application of a failure assessment diagram under rolling contact to components with hardness variable along the depth. *Procedia Engineering*, 10:746–751, 2011.

[93] Santos EC, Kida K, Honda T, Koike H, and Rozwadowska J. Fatigue strenght improvement of AISI E52100 bearing steel by induction heating and repeated

quenching. *Materials Science*, 47(5):677–682, 2011.

[94] Voskamp AP. *Microstructural changes during rolling contact fatigue*. PhD thesis, Technical University of Delft, Delft, 1996.

[95] Cerullo M. Application of Dang Van criterion to rolling contact fatigue in wind turbine roller bearings under elastohydrodynamic lubrication conditions. *P I Mech eng C-J Mec*, 228(12):2079–2089, 2014.

Publication [P1]

Application of the Dang Van criterion to rolling contact fatigue in wind turbine roller bearings

Application of Dang Van criterion to rolling contact fatigue in wind turbine roller bearings

Michele Cerullo

Department of Mechanical Engineering ,Technical University of Denmark, Lyngby 2100, Denmark
mcer@mek.dtu.dk

Abstract A 2-D plane strain finite element simulation of rolling contact in wind turbine roller bearings is used to study very high cycle fatigue (VHCF). Focus is on fatigue in the inner ring, where the effect of residual stresses and hardness variation along the depth are accounted for. The purpose here is to ensure that VHCF failure does not initiate. For the purpose the Dang Van multiaxial fatigue criterion is applied, simulating the contact on the bearing raceway by substituting the roller with the Hertzian static pressure distribution. Contact without friction is assumed here and the material used for the simulation is taken to be an AISI 52100 bearing steel. Both an initially stress free bearing and different residual stress distributions are considered. An assumed residual stress distribution, equilibrated by an elastic step calculation, is subsequently subjected to the stresses caused by the contact with the roller. The effect of variable hardness along the depth is also studied, relating its values to the fatigue limit parameters for the material and it is found that its distribution can have a significant influence on the probability of failure for bearings subjected to VHCF loading.

Keywords High Cycle Fatigue, Wind turbine, Dang Van

1. Introduction

It has been seen [1,2] that one of the important reasons of corrective maintenance for a wind turbine is a failure due to rolling contact fatigue (RCF) in one of the bearings in the gear box [3]. Therefore, the interest on the reliability of gearboxes grew over the last years [4,5]. Though failure rates in electrical systems and other subassemblies in a wind turbine are in fact higher, or at least comparable with faults in the gearbox, recent studies [6–8] show that the downtime, in terms of hours lost per failure, is much higher for latter ones. This, rather than the failure rate, is therefore one of the main reasons for the industry's focus on these subsystems.
In the gearbox, the bearings used are mostly roller bearings, due to the high loads involved. Even if the lubricant is kept clean and the bearing is properly lubricated, roller bearings sometimes experience rolling contact fatigue that appears as a crack starting below the surface of the inner race [9]. Once nucleated, this crack quickly propagates to the surface, resulting in particles of material flaking and leading to the failure of the bearing. Roller bearings for wind turbine applications operate in the fully elastic range and are subjected to a very high number of load cycles, with an expected life of 20 years [10]. However, practical experience show a high life scatter in these machinery elements, with failures that sometimes occur after a few years. The failure of these elements is thought to be due mainly to inhomogeneities and nonmetallic inclusions, that act as sites for crack nucleation under rolling contact fatigue. The cracks usually nucleate around inclusions, where the material experiences high stress concentration and typical butterfly defects are observed.
The modelling in the present paper is focused on ensuring that the cyclic stress fields stay within limits so that very high cycle fatigue damage does not initiate. Several multiaxial fatigue models have been developed [11–15], and some of them have been applied to RCF problems. The Dang Van criterion [16] and its further modifications has been widely used, over the last decades, in automotive industry [17] and in rolling contact problems as railwails and bearings [18,19]. It seems that the Dang Van criterion is not sufficiently conservative for negative values of the hydrostatic stress, therefore a modified version has been recently proposed [20], predicting a less sensitive behavior with respect to this stress component. This paper also includes a study of the overall effect

of pre-existing residual stresses in the material, resulting from hardening process. Using the Dang Van criterion, different residual stresses and hardening distributions are studied, and results are compared.

2. Problem formulation

Part of the initial geometry of the inner ring of the roller bearing is illustrated in Fig. 1. The inner ring and the shaft have been considered as one body of external radius $R=R_s+t_k$, where R_s is the shaft radius and t_k is the thickness of the inner ring. This assumption is equivalent to neglecting contact stresses related to the mounting and any local stress concentrations at the interface between ring and the shaft.

In order to reduce the computational time, only an angular sector of the solid, with angular width $\alpha=10°$, has been modeled. Far away from the surface, the region analyzed is terminated by a circular arc boundary with radius r. Along the edges, the solid is free to slide in the radial direction, being constrained in the direction perpendicular to the edges. A cartesian coordinate system Oxyz is used, with the origin O in the center of curvature of R, the axis z pointing out of the paper, and the axes x and y, respectively, horizontally and vertically aligned. As a 2-D model is studied, no edge effects in the direction perpendicular to the plane of the model are accounted for. The pressure acting on the raceway and resulting from the contact with the roller, is evaluated according to classical Hertzian theory, and is considered identical in any plane parallel to xy:

$$p(x,y)=p_0\,[1-(\frac{x-x_p}{a})^2-(\frac{y-y_p}{a})^2]^{0.5} \tag{1}$$

In Eq.(1), p_0 is the maximum value of the pressure, x_p and y_p the coordinates of the center of the contact area, a the semi-width of the contact area under the roller and x and y the coordinates of a generic point on the surface in the contact area. The value of p_0 is related to the force acting on the roller by the relation

$$p_0=\sqrt{\frac{q}{\pi}\frac{\Delta}{\rho}} \tag{2}$$

where Δ is function of the Young moduli E_i and Poisson ratios ν_i of the roller and the inner race, here assumed of the same material. The constant ρ is a pure function of the curvature radii and $q=F/L$ is the force per unit length acting on the roller.

A bearing with the inner ring thickness $t_k=19$ mm, mounted on a shaft of $R_s=200$ mm, has been used in the simulations. Furthermore values of 70 mm and 20 mm, respectively, are assumed for the length and the radius of the roller. A load of 37 KN is considered pushing the roller against the inner race, resulting in a static Hertzian maximum pressure p_0~1 GPa. The contact is assumed continuous without any vibrations effects. No friction or sliding are here accounted for.

The pressure distribution, that simulates the contact, is assumed to move along the surface, in a region where the mesh is uniform. Far away from the zone affected by the contact stresses, instead, the elements are stretched, both in the radial and in the tangential direction, close to the edges. The material is considered isotropic, with Young modulus E=210 GPa and Poisson ratio $\nu=0.3$.

In terms of the displacement components u_i on the reference base vectors the strain tensor is given by

$$\varepsilon_{i,j}=\frac{1}{2}(u_{i,j}+u_{j,i}) \tag{3}$$

where $()_{,j}$ denotes partial differentiation. The equilibrium equations, written in terms of the stress tensor σ_{ij} and the strain tensor ε_{ij}, are obtained by the use of the principle of virtual work:

$$\int_V \sigma_{ij}\delta\varepsilon_{ij}\,dV=\int_S T_i u_i\,dS \tag{4}$$

where V and S are the volume and surface of the region analyzed, and T_i are the specified surface tractions.

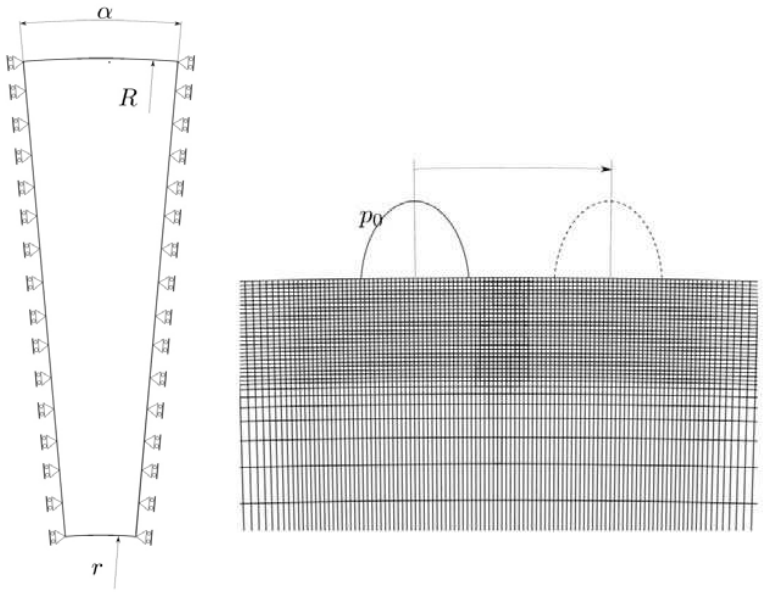

(a) (b)

Figure 1. (a) Geometry used to model the problem: r=100mm, R_s=200mm, t_k=19 mm, α=10°. (b) A detail of the mesh used.

2.1 The Dang Van criterion

A brief introduction to the basis of the fatigue criterion used will be given (see further details in [16]). The Dang Van criterion is a stress based multiaxial fatigue criterion. It relates the variation of the stress state in a material point to a critical parameter, that should not be reached:

$$f[\sigma_{ij}(t)] \leq \lambda \tag{5}$$

The critical value λ is usually function of the fatigue limits in pure torsion, τ_w, and the fatigue limit in pure bending, σ_w, and its choice is essential in a multiaxial criterion since it establishes which is the most important stress component that is assumed to have influence on the failure. The Dang Van criterion, in particular, can be formulated as:

$$\tau_{max}(t)+\alpha_{DV}\sigma_H(t) \leq \tau_w \tag{6}$$

where

$$\alpha_{DV}= 3\left(\frac{\tau_w}{\sigma_w}-\frac{1}{2}\right) \tag{7}$$

is a constant that depends on the material fatigue limits previously mentioned, $\sigma_H(t)$ is the instantaneous hydrostatic component of the stress tensor and $\tau_{max}(t)$ is the instantaneous value of the Tresca-like shear stress

$$\tau_{max}(t)= \frac{\widehat{\sigma_I}(t)-\widehat{\sigma_{III}}(t)}{2} \tag{8}$$

The stress deviator is obtained by the usual definition:

$$s_{ij}(t)=\sigma_{ij}(t)- \delta_{ij}\sigma_H(t) \tag{9}$$

Then a constant tensor, s_{ij}^m, is calculated by solving the minmax problem

$$s_{ij}^{m}=\min_{s_{ij}^{*}} \max_t [(s_{ij}(t)-s_{ij}^{*})(s_{ij}(t)-s_{ij}^{*})] \quad (10)$$

and the shifted deviator tensor is defined as

$$\widehat{s_{ij}}(t)=\sigma_{ij}(t)- s_{ij}^{m} \quad (11)$$

The principal values of the shifted tensor appear in Eq. (8).
The problem in Eq. (10) is solved iteratively using a move limit approach :

$$s_{ij}^{m}=\min_{s_{ij}^{*}} \max_t [(s_{ij}(t)-s_{ij}^{*})(s_{ij}(t)-s_{ij}^{*})]=\min_{s_{ij}^{*}} [\max_t \Phi] \quad (12)$$

with

$$\Phi=\Phi(t, s_{ij}(t), s_{ij}^{*}) \quad (13)$$

Choosing an arbitrarily starting value for s_{ij}^{*}, for example the average deviatoric stress tensor in the stress history for that material point, then for every iteration we identify the maximum value of Φ. Let t_m be the time step at which $\max \Phi$ happen, then the value of s_{ij}^{*} is updated

$$s_{ij}^{*}=s_{ij}^{*}+ ds_{ij}^{*} \quad (14)$$

with

$$ds_{ij}^{*}=\gamma (s_{ij}(t_m)-s_{ij}^{*}) \quad (15)$$

which can be interpreted as a modified steepest descend method. If at one step Φ increases, γ is reduced to 0.25 γ. The iteration is stopped if the norm of the difference between s_{ij}^{*} at the current iteration step k and at the previous step falls into a tolerance range:

$$\left\| s_{ij}^{*}]_k - s_{ij}^{*}]_{k-1} \right\| \le \varepsilon_{toll} \quad (16)$$

Although a superimposed hydrostatic tension has an effect on the fatigue life in normal cyclic loading [21], several studies [11] have shown that a superimposed mean static torsion has no effect on the fatigue limit of metals subjected to cyclic torsion. The independency of the mean shear stress is correctly predicted through the minimization process in Eq. (10), see also [20]. The Dang Van criterion could also be used with $\tau_{max}(t)$ representing the maximum shear stress at every point of the stress history. Then, one would not account for the experimental observation that in cyclic torsion fatigue failure is independent of the mean shear stress, and this would usually result in lower permitted stress levels.
The Dang Van proposal is equivalent to request, in the $\sigma_H(t)$ - $\tau_{max}(t)$ plane, that all the representative points of the stress state, fall below the line intersecting the $\tau_{max}(t)$ axis in τ_w with a negative slope of α: if all of the points fulfill this requirement, the criterion predicts a safe life for the component (see Fig. 2).
The original Dang Van safe locus predicts a detrimental effect of tensile hydrostatic stress while an over-optimistic positive effect is expected from compressive values. The negative effect of tensile mean stress is well known in literature from classic Haigh diagrams, that also show a flat response for negative stress ratios [22, 23]. For this reason it is not too conservative to choose a different safe locus in the Dang Van plane to be in agreement with this response, for example a bilinear limit curve, as proposed recently in [20]. The safe locus could be therefore identified in two segments, one with a null slope and the other one with a negative slope equal to α (Fig. 2). For $\sigma_H(t) \ge \sigma_A$ the safe region is identical to the original Dang Van region, while for smaller values of σ_A, the cut-off with the flat curve replaces the Dang Van limit curve by a curve more on the safe side. Values of $\sigma_A = \sigma_w/3$ and of $\tau_A = \sigma_w/2$ have been proposed in [20], on the basis of experimental results obtained on high-strength steel smooth specimens. However, it is possible to choose a different set of values for (σ_A, τ_A), though here the same choice has been made. If the ratio of the fatigue limits, σ_w/τ_w, was equal to 0.5, the value α_{DV} in Eq. (6) would be zero, which is far from reality, as steels usually

show ratios between 0.57 and 0.8 [21]. Anyway, it is always possible to assume different values of σ_A, more or less conservative than the cut off shown in Fig 2.
In the following sections, both the original safe locus and a new one with the mentioned cut-off will be used, and results will be compared. For τ_w a value of 360 MPa has been imposed [24] and a ratio $\sigma_w/\tau_w=\sqrt{3}$. With this assumption the value of the constant α_{DV} used in the calculations is approximately 0.23205.

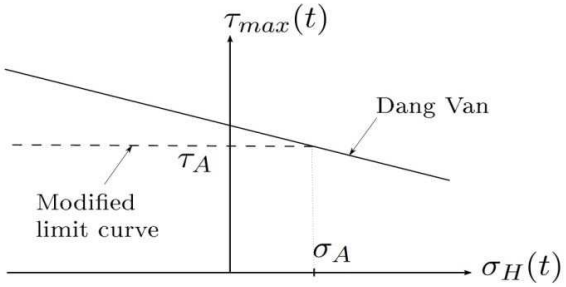

Figure 2. The Dang Van safe locus: the dashed line represents the alternative limit curve, for $\sigma_H(t)<\sigma_A$, here assumed equal to $\sigma_w/3$, as proposed in [20].

For a material point subjected, at time t, to $\sigma_H(t)$ and $\tau_{max}(t)$, the ratio between $\tau_{max}(t)$ and the corresponding limit value for that $\sigma_H(t)$ is here used to define the damage factor n(t). Points on the limit curve, then, result in a unit damage factor; points inside the safe region have damage factor smaller than one. As previously mentioned, two different safe loci are here used: one with a linear limit curve and another one with a bilinear limit curve. Consequently, a damage factor is here defined as

$$n(t)= \frac{\tau_{max}(t)}{\tau_w-\alpha_{DV}\,\sigma_H(t)} \tag{17}$$

if referred to the original Dang Van's safety region or

$$n(t)=\begin{cases} \dfrac{\tau_{max}(t)}{\tau_w-\alpha_{DV}\,\sigma_H(t)} & \text{if } \&\sigma_H>\sigma_A \\ \dfrac{\tau_{max}(t)}{\tau_A} & \&\text{if } \sigma_H\le\sigma_A \end{cases} \tag{18}$$

when the bilinear limit curve is used. As mentioned above, σ_A and τ_A are chosen equal to $\sigma_w/3$ and $\sigma_w/2$, respectively.

3. Results and discussion

The Dang Van criterion has been applied to the rolling contact problem and for the geometry described in section 2. The load history has been divided in an adequate number of steps and, for each time step, the value of the damage factor n(t) has been calculated, both with the original Dang Van limit curve and with the modified one. The maximum value in time

$$n= \max_t n(t) \tag{19}$$

is then chosen, as representative for that material point. If this $n<1$, the prediction is that initiation of fatigue failure will not occur in the material point. The representative points corresponding to the max value of the damage factor are plotted, in Fig. 3, in the Dang Van region, for all the integration points in the region analyzed.
In Fig. 4 the maximum values of this factor n are plotted against the distance from the surface. Both safe regions, as described before, are used. As we can see, n reaches the highest value in a sub-surface region, about 0.20 mm below the surface : this is consistent with literature, where a lot of sub-surface initiated failures in bearings for windmill applications are reported.

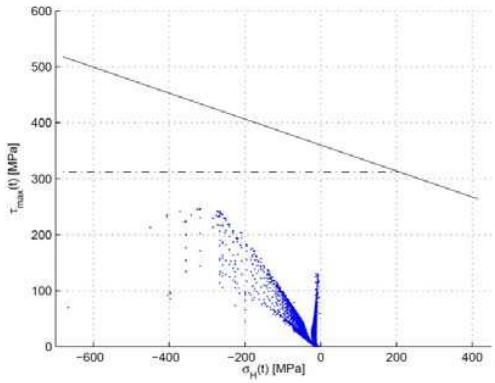

Figure 3. The Dang Van criterion: in order that the failure does not occur, all the representative points should be inside the safe region delimited by the limit curves. In this figure, and for the problem considered, only the representative points corresponding to max value of the damage factor are plotted for all the integration points in the region analyzed.

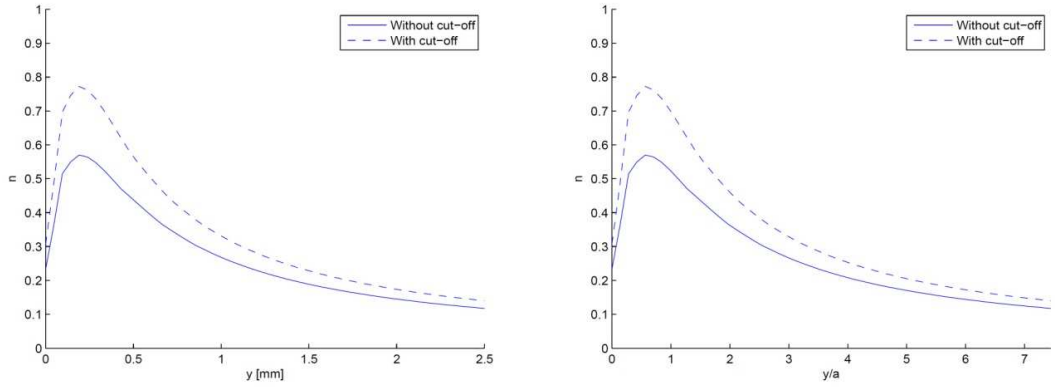

Figure 4. Damage factor versus distance from surface (a) and versus distance from surface non dimensionalized by the half contact width (b).

3.1 Hardness variation

The relationships between fatigue strength, the hardness and the ultimate tensile strength are used, in this section, to study the influence of the hardness variation in the inner ring.
Since fatigue crack initiation is mainly caused by slip within grains, the yield stress, in the past, has been thought to have the strongest correlation with the fatigue limit. However Murakami [25] has found better correlations between tensile strength, hardness and fatigue limits.
In order to correlate the hardness to the fatigue limit, τ_w, this limit has first been related to σ_{UTS} through an approximate expression proposed in [26] for low-alloy steels:

$$\tau_w=\sigma_w/\sqrt{3}\approx 0.274\ \sigma_{UTS} \tag{20}$$

Denoting the Brinell hardness by HB and using an approximate relationship found in [27]

$$\sigma_{UTS}=0.0012\ HB^2+3.3\ HB \tag{21}$$

an approximate final relation between τ_w and HB can be written as

$$\tau_w=0.274\ (0.0012\ HB^2+3.3\ HB) \tag{22}$$

In the following we assume that the fatigue limit τ_w is given by the Eq. (22). If another expression $\tau_w(HB)$ applies for a material, this will not in principle change the procedure. In fact, all we need is

the value of τ_w in each material point of the solid analyzed.
Different hardness distributions along the depth have been studied here. Thus the value of τ_w corresponding to the value of the hardness at that depth has been imposed in the material for each Gauss integration point.
The different hardness distributions imposed in the subsurface region of inner ring and the correspondent τ_w distributions are shown in Fig. 5 (a)–(d). At distances greater than 1 mm from the surface, HB, for distributions (a) and (b), are taken to be constant, at a value such that the related fatigue limit, $\tau_w=\tau_w(HB)$, is approximately 360 MPa. This assumption is equivalent to considering how the effect of a surface hardening process would benefit the fatigue response of the bearing. Results show that the values of the damage factor n and the depth at which the maximum n is reached, are strongly dependent on the particular distribution of hardness imposed (Fig. 6).

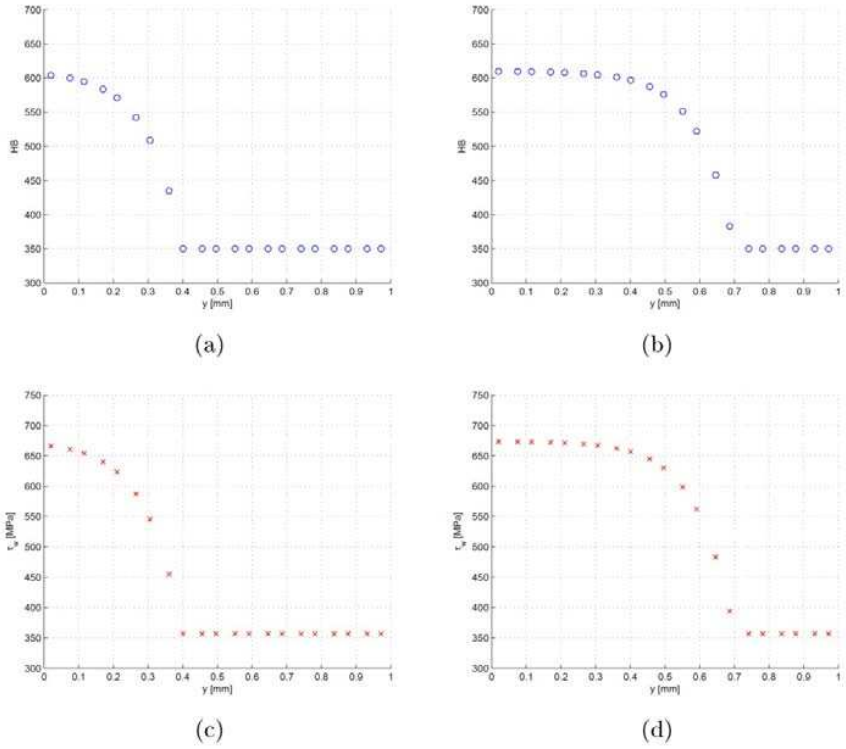

Figure 5. Hardness distributions ((a)-(b)) and correspondent values of τ_w ((c)-(d)) in the first millimeter of depth .

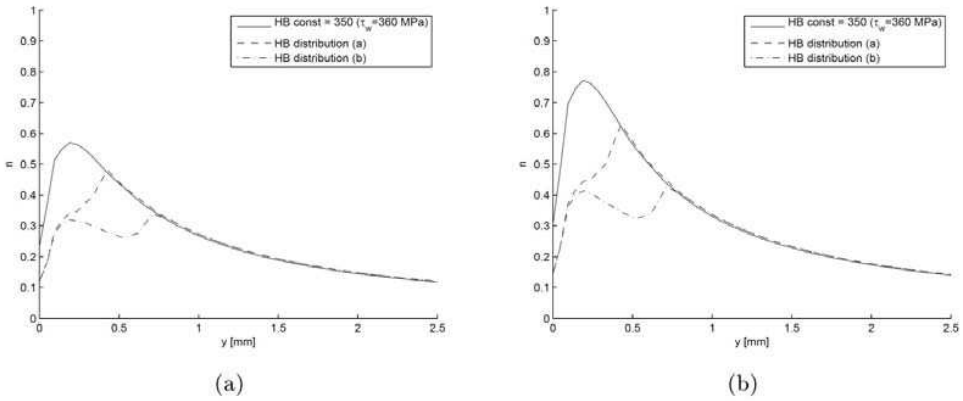

Figure 6. Damage factor versus distance from surface. In (a) the original Dang Vang safe locus has been used, while in (b) the bilinear limit curve, as described in section 2.1. The different distributions are referred to Fig. 5.

For all the cases analyzed, the peak of the n-curve shifts away from the surface of the inner ring and, for cases shown in Figs. 5a and 5b, the peak values of n are smaller than the correspondent peaks for a material with uniform hardness. In other words, the rings with extra surface hardening have higher safety against fatigue failure.

3.2 Residual stresses

In order to analyze the influence of pre-existing stresses in the bearing, two different residual stress distributions have been considered. The bearing with the assumed residual stress distribution, equilibrated by an elastic step calculation, is subsequently subjected to the stresses caused by the contact with the roller. The results obtained with the Dang Van criterion are then compared with the results obtained in the bearing free of residual stresses.

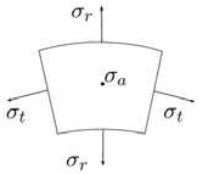

Figure 7. Convention used for the principal stresses in the polar coordinate system.

In Fig. 7 the convention used to name the residual stresses is clarified, while, in Figs. 8a and 8b, the residual stress distributions, in terms of principal stresses, are plotted versus the distance from the surface. Far away from the surface, the residual stresses are assumed to be constant and near zero.
The results for the two different safe loci (Fig. 2) are shown in Fig. 9. The pre-existing stress states in the inner ring, in the case of the modified safe locus, have little effect, neither positive nor negative (Fig. 9a). The residual stresses, in fact, result in a simple shift along the σ_H axis in the Dang Van region (Fig. 2) but this does not change the distance from the limit curve since all the most critical material points are subjected to values of σ_H smaller than σ_A and therefore they are in the region where the limit value for τ_{max} is constant and equal to τ_A. If the original limit curve is used, instead, the residual stress distribution (a) from Fig. 8 results in a reduction of the maximum damage factor for the compressive residual stresses, but an increase of the maximum damage factor for tensile residual stresses (Fig. 9b).

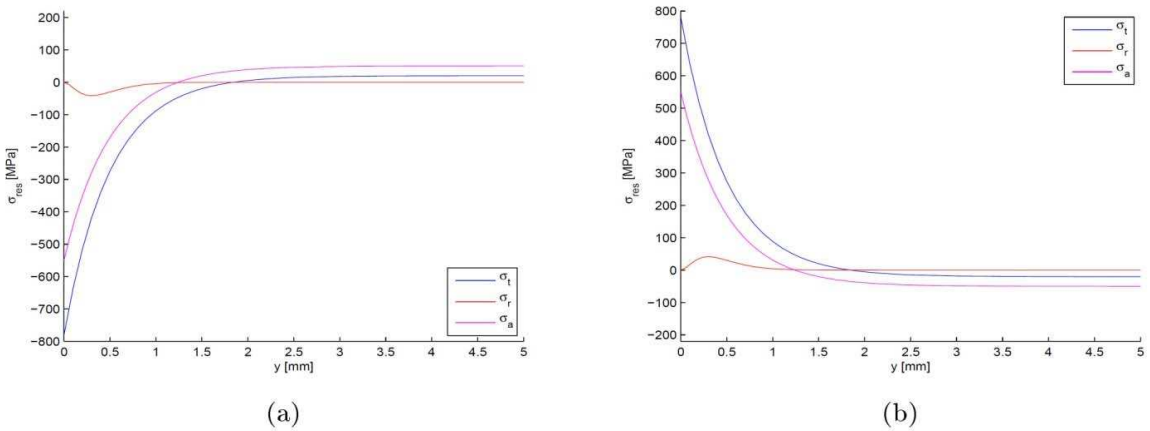

Figure 8. Residual stresses assumed in terms of principal stresses. Distribution (b) is obtained by multiplying (a) by -1.

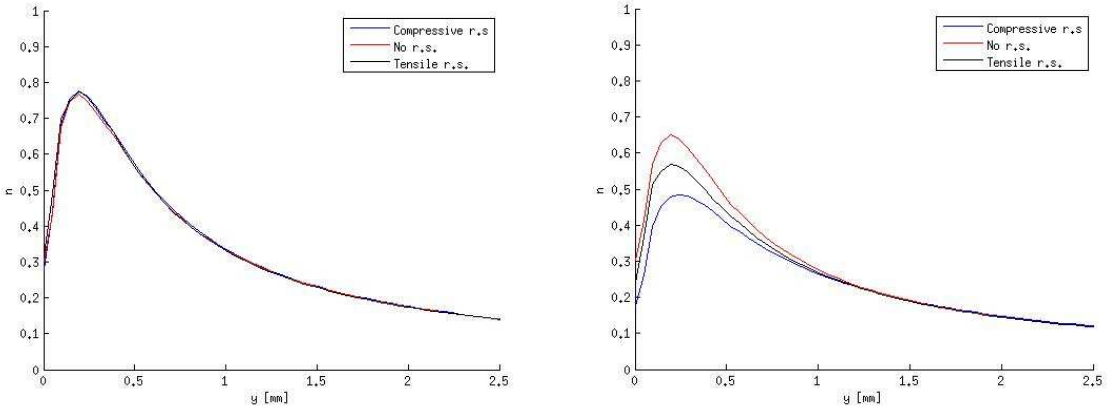

(a) (b)

Figure 9. Damage factor versus distance from surface for bilinear (a) and original limit curve (b).

4. Conclusions

The Dang Van criterion has been applied to a roller bearing for windmill applications and the influence of hardness variations and different residual stresses has been studied. Results have shown that, according to the Dang Van criterion, the highest damage factor is reached below the surface, regardless the safe locus used. This suggests that failure is most likely to initiate in the material a little below the surface, which is consistent with literature that reports subsurface failures of roller bearings for wind turbine applications.

The effect of increased hardness, in a thin layer close to the surface, has also been studied, relating the hardness to the fatigue strength of the material. The particular hardness distribution induced is seen to be important in evaluating the safety against fatigue for the bearing. Assuming that a higher fatigue strength corresponds to a higher Brinell hardness, the results indicate that a hardening surface treatment will be beneficial in terms of fatigue damage. However, surface hardening is not really possible for AISI 52100 bearing steel, though some recent work [28] seems to indicate an improvement of fatigue strength, for these steels, by induction heating and repeated quenching. It may be noted also that some steels show a maximum for the curve $\tau_w(\mathrm{HB})$, which would limit the applicability of Eq. (22). In fact, Eq.(22) is valid only for smaller values of hardness.

Bearings with different residual stress distributions have also been studied and calculations carried out show, for the Dang Van criterion, a positive effect of compressive residual stresses in the subsurface region according to the original safe locus. No influence of residual stresses has been found with the use of the modified safe locus and for the load case analyzed.

Acknowledgements

The author would like to thank Prof. Viggo Tvergaard and Associate Prof. Peder Kilt, Technical University of Denmark, for ideas, discussions and comments. This work is supported by the Danish Council for Strategic Research, in the DSF center REWIND.

References

[1] H. Arabian-Hoseynabadi, H. Oraee, P.J. Tavner, Failure Modes and Effects Analysis (FMEA) for wind turbines. Electrical Power and Energy Systems , 32 (2010) 817–824.

[2] Y. Amirat, M.E.H. Benbouzid, E. Al-Ahmar, B. Bensaker, S. Turri, Brief status on condition monitoring and fault diagnosis in wind energy conversion systems. Renew Sust Energ Rev, 13 (2009) 2629–2636.

[3] P.J. Blau, L.R. Walker, H. Xu, R.J. Parten, J. Qu, T. Geer, Wear analysis of wind turbine gearbox bearings - Final Report. Oak Ridge National Laboratory 2010.

[4] K. Smolders, Y. Feng, H. Long, P. Tavner Reliability Analysis and Prediction of Wind Turbine

Gearboxes. European Wind Energy Conference–EWEC 2010.
[5] C.Fernandes, R. C. Martins, Jorge H. O. Seabra, Friction torque of cylindrical roller thrust bearings lubricated with wind turbine gear oils. Tribology International (2012) (article in press).
[6] F. Spinato, P. J. Tavner, G. J. W. van Bussel, E. Koutoulakos, Reliability of Different Wind Turbine Concepts with Relevance to Offshore Application. European Wind Energy Conference 2008.
[7] F. Spinato, P. J. Tavner, G. J. W. van Bussel, E. Koutoulakos, Reliability of wind turbine subassemblies. IET Renewable Power Generation, 3 (2009) Issue 4, 387–401.
[8] Ma yang, He Chengbing, Feng Xinxin, Institutions Function and Failure Statistic and Analysis of Wind Turbine. Physics Procedia, 24 (2012), 25–30.
[9] F. Sadeghi, B. Jalalahmadi, T. S. Slack, N. Raje, N. K. Arakere, A Review of Rolling Contact Fatigue. Journal of Tribology, 131 (2009), Issue 4, 041403–1.
[10] A. Ragheb, M. Ragheb, Wind turbine gearboxes technologies. Proceedings of the 1st International Nuclear and Reneawble Energy Conference - INREC 2010.
[11] G. Sines, Behaviour of metals under complex static and alternating stresses, in: Metal Fatigue (eds. G. Sines and J.L. Waisman), McGraw-Hill, New York, 1959, pp. 145–169.
[12] W. N. Findley, Trans. ASME Ser B 81 (1959), 301.
[13] T. Matake, Bull. JSME 20 (1977), 257.
[14] D. L. McDiarmid, Fatigue Fract. Engng Mater. Struct. 17 (1994), 1475.
[15] I. V. Papadopoulos, Fatigue polycyclique des métaux: une nouvelle approche. Ph.d Thesis, spécialité: Mécanique, Ecole des Ponts et Chaussées, France, 1987.
[16] K. Dang Van, Sur la résistance à la fatigue des métaux. Sciences Technique Armement 47 (1973), 3.
[17] A.-S. Beranger, J.-V. Berard and J.-F. Vittori, A fatigue life assessment methodology for automotive components, in Fatigue Design of Components, in: ESIS Publication, 22, G. Marquis and J. Solind (eds.), Elsevier Science, 1997.
[18] A. Bernasconi, M. Filippini, S. Foletti, D. Vaudo, Multiaxial fatigue of a railwheel steel under non-proportional loading. International Journal of Fatigue, 28 (2006), 663–672.
[19] M. Ciavarella, F. Monno, G. Demelio. On the Dang Van fatigue limit in rolling contact fatigue. International Journal of Fatigue, 28 (2006), 852–863.
[20] H. Desimone, A. Bernasconi, S. Beretta, On the application of Dang Van criterion to rolling contact fatigue. Wear 260 (2006), 568–571.
[21] S. Suresh, Fatigue of materials, Cambridge University Press, New York, 2006.
[22] R.B. Heywood, Designining against fatigue, Chapman and Hall Ltd., London, 1962.
[23] T.J. Dalan, in: O.J. Horger (Ed.), ASME Handbook, Metal Engineering Design, New York.
[24] J. Lai, T. Lund, K. Rydén, A. Gabelli, I. Strandell, The fatigue limit of bearing steels – Part I: A pragmatic approach to predict very high cycle fatigue strength. Int. Journal of Fatigue 37 (2012), 166–167.
[25] Y. Murakami, Metal Fatigue: Effects of Small defects and Nonmetallic Inclusions, Elsevier, Oxford, 2002.
[26] B. Atzori, G. Meneghetti, L. Susmel, Material fatigue properties for assessing mechanical components weakened by notches and defects. Fatigue Eng Mater, 28 (2005), 83–97.
[27] M.L. Roessle, A. Fatemi, Strain-controlled fatigue properties of steels and some simple approximations. Int. Journal of Fatigue, 22 (2000), 495–511.
[28] E.C. Santos, K. Honda, H. Koike, J. Rozwadowska, Fatigue strength improvement of AISI 52100 bearing steel by induction heating and repeated quenching. Material Science, 47 (2011), No. 5, 677 –682.

Publication [P2]

Application of the Dang Van criterion to rolling contact fatigue in wind turbine roller bearings under elastohydrodynamic lubrication conditions

Application of Dang Van criterion to rolling contact fatigue in wind turbine roller bearings under elastohydrodynamic lubrication conditions

Michele Cerullo

Proceedings of the Institution of Mechanical Engineers, Part C: Journal of Mechanical Engineering Science 2014 228: 2079 originally published online 20 December 2013
DOI: 10.1177/0954406213516946

Original Article

Institution of MECHANICAL ENGINEERS
Journal of MECHANICAL ENGINEERING SCIENCE

Proc IMechE Part C:
J Mechanical Engineering Science
2014, Vol. 228(12) 2079–2089

DOI: 10.1177/0954406213516946
pic.sagepub.com
SAGE

Application of Dang Van criterion to rolling contact fatigue in wind turbine roller bearings under elastohydrodynamic lubrication conditions

Michele Cerullo

Abstract

A 2D plane strain finite element program has been developed to investigate very high cycle fatigue in wind turbine roller bearings due to rolling contact. Focus is on fatigue in the inner ring, where the effect of residual stresses and hardness variation along the depth is accounted for. Both classic Hertzian and elastohydrodynamic lubrication theories have been used to model the pressure distribution acting on the inner raceway and results are compared according to the Dang Van multiaxial fatigue criterion. The contact on the bearing raceway is simulated by substituting the roller with the equivalent contact pressure distribution. The material used for the simulations is taken to be an AISI 52100 bearing steel and linear elastic behavior is here assumed. The effect of different residual stress distributions is also studied, as well as the effect of variable hardness along the depth, relating its values to the fatigue limit parameters for the material. It is found that both for Hertzian and elastohydrodynamic lubrication contacts, the Dang Van criterion predicts that fatigue failure will first occur in the subsurface region and that, regardless of the specific pressure distribution used, the hardness distribution can have a significant influence on the safety against failure for bearings subjected to very high cycle fatigue loading.

Keywords

High cycle fatigue, wind turbine, Dang Van, rolling contact fatigue, elastohydrodynamic lubrication

Date received: 14 August 2013; accepted: 12 November 2013

Introduction

It has been seen[1,2] that one of the important reasons (we here refer to causes related to mechanical failure) of corrective maintenance for a wind turbine is failure in one of the bearings in the gear box.[3] Therefore, the interest in the reliability of gearboxes has grown over the last years.[4,5] Though failure rates in electrical systems and other subassemblies in a wind turbine are in fact higher, or at least comparable with faults in the gearbox, recent studies[6,7] show that the downtime, in terms of hours lost per failure, is much higher for the latter. This, rather than the failure rate, is therefore one of the main reasons for the industry's focus on these subsystems.

In the gearbox, the bearings used are mostly roller bearings, due to the high loads involved. The majority of wind turbine gearbox failures appear in the intermediate and high–speed shaft bearings,[8] while failure is more unlikely to be observed in the planet bearings. It is well known that even if the lubricant is kept clean and the bearing is properly lubricated, roller bearings sometimes experience failure that can appear either as a surface crack or as a subsurface crack. Both mechanisms have been denoted as rolling contact fatigue (RCF) in a general review on this subject.[9] In the present investigation, the analyses focus on determining the location in the bearing (surface or subsurface) where the safety against fatigue initiation is smallest. Roller bearings for wind turbine applications operate in the fully elastic range and are subjected to a very high number of load cycles, with an expected life of 20 years.[10] This expected life corresponds to a number of cycles to failure in the order of 10^9–10^{11} cycles, which is what is referred to as very high cycle fatigue (VHCF) regime. It is commonly believed[9,11] that fatigue failure in this regime is mainly due to interior

Department of Mechanical Engineering, Technical University of Denmark, Lyngby, Denmark

Corresponding author:
Michele Cerullo, Department of Mechanical Engineering, Technical University of Denmark, Nils Koppels Alle, 2100 Lyngby, Denmark.
Email: mcer@mek.dtu.dk

cracks that may nucleate at nonmetallic inclusions. In wind mill roller bearings, a crack may start below the surface of the inner race and, once nucleated, this crack can quickly propagate to the surface, resulting in particles of material flaking and leading to the failure of the bearing.

Beside the expected life, practical experience shows a high life scatter in these machinery elements, with failures that sometimes occur after a few years.[8] The failure of these elements is thought to be mainly due to inhomogeneities and nonmetallic inclusions that act as sites for crack nucleation under RCF. The cracks usually nucleate around inclusions, where the material experiences high stress concentration and typical butterfly defects are observed.[12–14]

The modeling in the present paper is focused on ensuring that the cyclic stress fields caused by elastohydrodynamic lubricated (EHL) contact stay within limits so that VHCF damage does not initiate. A few preliminary results for Hertzian contact stresses and a cruder mesh have been given in Ref. 15. Several multiaxial fatigue models have been developed,[16–20] and some of them have been applied to RCF problems. The Dang Van criterion[21,22] and its further modifications have been widely used, over the last decades, in the automotive industry[23] and in rolling contact problems as railways and bearings.[24,25] It seems that the Dang Van criterion is not sufficiently conservative for negative values of the hydrostatic stress,[25–27] therefore a modified version has been recently proposed,[27] predicting a less sensitive behavior with respect to this stress component. This paper also includes a study of the overall effect of preexisting residual stresses in the material, resulting from a hardening process. Using the Dang Van criterion in a Finite Element Method (FEM) code developed by the author, different residual stresses and hardening distributions are studied, and results are compared.

Problem formulation

Part of the initial geometry of the inner ring of the roller bearing is illustrated in Figure 1. The inner ring and the shaft have been considered as one body of external radius $R = R_s + t_k = 219\,\text{mm}$, where $R_s = 200\,\text{mm}$ is the shaft radius and $t_k = 19\,\text{mm}$ is the thickness of the inner ring. This assumption is equivalent to neglecting contact stresses related to the mounting and any local stress concentrations at the interface between the ring and the shaft. A value of $R_{roll} = 21\,\text{mm}$ has been considered for the roller radius.

In order to reduce the computational time, only an angular sector of the solid, with angular width $\alpha = 5^\circ$, has been modeled. Far away from the surface, the region analyzed is terminated by a circular arc boundary with radius r. Along the sides, the solid is free to slide in the radial direction, being constrained in the direction perpendicular to the sides. A Cartesian coordinate system $Oxyz$ is used, with the origin O in the center of the shaft, the axis z pointing out of the paper, and the axes x and y horizontally and vertically aligned, respectively. As a 2D model is studied, no edge effects in the direction perpendicular to the plane of the model are accounted for.

Two different pressure distributions (Figure 2) are used to simulate the contact between the roller and the raceway.

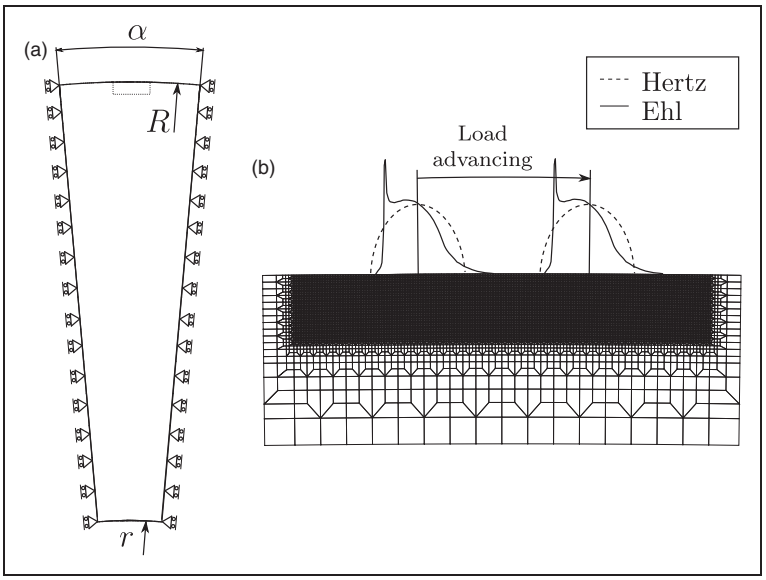

Figure 1. Geometry used to model the problem: $r = 100\,\text{mm}$, $R = 200\,\text{mm}$, $t_k = 19\,\text{mm}$, $R_{roll} = 21\,\text{mm}$, $\alpha = 5^\circ$. On the right, a detail of the mesh used.

A first distribution p_H is taken to be the static Hertzian pressure distribution for a line contact

$$p_H(x,y) = p_0\left[1 - \left(\frac{x-x_p}{a}\right)^2 - \left(\frac{y-y_p}{a}\right)^2\right]^{(1/2)} \quad (1)$$

In equation (1), p_0 is the maximum value of the pressure, x_p and y_p the coordinates of the center of the contact area, a the semi-width of the contact area under the roller, and x and y the coordinates of a generic point on the surface in the contact area. It should be noted that in the original Hertz model, no vertical coordinate is included and an equivalent half space is introduced. However, here it was chosen to map the Hertzian distribution on a round surface. The value of p_0 is related to the force acting on the roller by the relation

$$p_0 = \sqrt{\frac{q}{\pi}\frac{\Delta}{\rho}} \quad (2)$$

where $\Delta = (\frac{1-\nu_1^2}{E_1} + \frac{1-\nu_2^2}{E_2})^{-1}$ is function of Young's moduli E_i and Poisson's ratios ν_i of the roller and the inner race, here assumed of the same material. The constant $\rho = (\frac{1}{R} + \frac{1}{R_{roll}})^{-1}$ is a function of the curvature radii and $q = F/L$ is the force per unit length acting on the roller.

The second pressure distribution used in calculations, p_{ehl}, was inspired by Jacobson et al.,[28] where a numerical program was developed to study different EHL contact problems. Under EHL conditions, the high pressure causes the viscosity of the lubricant to increase exponentially: thus the lubricant becomes able to carry both normal and shear load and causes deformations in the two bodies in contact. As the normal load used in Ref. 28 is too small compared to typical loads for bearings in a wind turbine gear box, the original normal pressure distribution (Figure 4(b) in Ref. 28) has been scaled, ensuring that the total load, F, expressed in terms of the integral of the pressure over the contact area, is the same for the two distributions

$$F = \int_{A_H} p_H \, \mathrm{d}s = \int_{A_{ehl}} p_{ehl} \, \mathrm{d}s \quad (3)$$

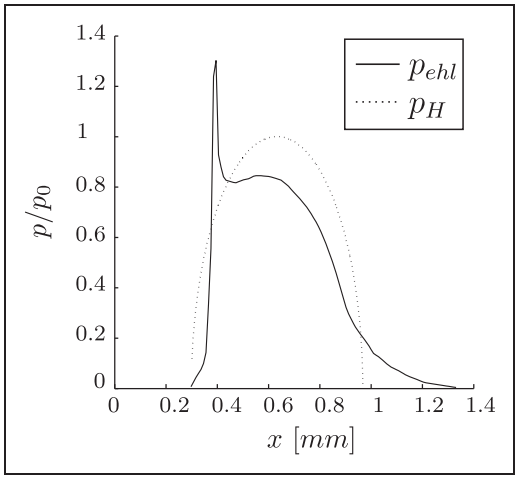

Figure 2. The two different normal pressure distributions used in the simulations, p_H and p_{ehl}. The two distributions are here plotted on an equivalent flat half space, according to the Hertzian model, where x_p in equation (1) is the center of the Hertzian pressure distribution.

Thus, no separate solution has been obtained here for the EHL contact problem, but the p_{ehl} distribution applied here is considered useful for an indicative parametric study. Also, the particular profile obtained, has a more pronounced pressure spike, which is typical for high speeds, as those expected in high speed shaft roller bearings that rotate up to 1500–1800 r/min. The shear load distribution that depends, among others, on the normal load, on the viscosity of the lubricant, and on the relative velocity of bodies accounts for the friction in the contact. In order to take this into account, in some calculations a simplified assumption, indicated by tribological calculations currently carried out at the Technical University of Denmark,[29] was used for the shear stress distribution: $p_t = 0.1\, p_{ehl}$. The proportionality of p_t is equivalent to consider a uniform value of the friction coefficient throughout the contact. In these calculations this shear load distribution has thus been applied to the surface of the inner ring in contact, together with the normal distribution p_{ehl}. The resulting friction traction on the inner ring is oriented in the direction of the x axis.

A bearing with the inner ring thickness $t_k = 19$ mm, mounted on a shaft of $R_s = 200$ mm, has been used in the simulations. Furthermore values of 70 and 20 mm, respectively, are assumed for the length and the radius of the roller. A peak load of 37 kN is considered pushing the roller against the inner race, resulting in a static Hertzian maximum pressure $p_0 \approx 1$ GPa. This value of the pressure is a typical working condition for roller bearings in the gearbox, though it must be noted that sometimes the rings can experience overloads, due for instance to misalignments or grid connection, that can increase this value. Here however the load on the roller was considered constant. The Hertzian contact half-width, a, is equal to 0.33 mm and the contact is assumed continuous without any vibration effects.

The pressure distributions, that simulate the contact, are assumed to move along the surface, in a region where the mesh is uniform. The elements size, which is here 20 μm, is then smoothly increased from this region to the edges, by a step-up process. The material is considered isotropic, with Young's modulus $E = 210$ GPa and Poisson's ratio $\nu = 0.3$.

In terms of the displacement components u_i on the base vectors, the strain tensor is given by

$$\varepsilon_{ij} = \frac{1}{2}(u_{i,j} + u_{j,i}) \tag{4}$$

where $()_{,j}$ denotes partial differentiation. The equilibrium equations, written in terms of the stress tensor σ_{ij} and the strain tensor ε_{ij}, are obtained by the use of the principle of virtual work

$$\int_V \sigma_{ij}\delta\varepsilon_{ij}\mathrm{d}V = \int_S T_i\delta u_i\mathrm{d}S \tag{5}$$

where V and S are the volume and surface of the region analyzed, and T_i are the specified surface tractions.

The Dang Van criterion

A brief introduction to the basis of the fatigue criterion used will be given (see further details in Refs. 21,22). The Dang Van criterion is a stress-based multiaxial fatigue criterion which assumes that even if at macroscale the stress state remains in the elastic regime, at grain scale (called "mesoscale") the material can show some plasticity initially. For this reason, a residual stress tensor can exist such that the macroscopic stress tensor gives a state of stress under the yield limit. According to Melan's theorem on shakedown, this residual stress tensor must be time invariant.

The Dang Van criterion is formulated as

$$\tau_{\max}(t) + \alpha_{DV}\sigma_H(t) \leqslant \tau_w \tag{6}$$

where τ_w is the fatigue limit in pure torsion and σ_w as the fatigue limit in pure bending (see Figure 3). The constant α_{DV}

$$\alpha_{DV} = 3\left(\frac{\tau_w}{\sigma_w} - \frac{1}{2}\right) \tag{7}$$

depends on the material fatigue limits previously mentioned, $\sigma_H(t)$ is the instantaneous hydrostatic component of the stress tensor, and $\tau_{\max}(t)$ is the instantaneous value of the Tresca-like shear stress

$$\tau_{\max}(t) = \frac{\hat{s}_I(t) - \hat{s}_{III}(t)}{2} \tag{8}$$

The stress deviator is obtained by the usual definition

$$s_{ij}(t) = \sigma_{ij}(t) - \delta_{ij}\sigma_H(t) \tag{9}$$

In order to apply the Dang Van criterion, it is necessary to find the residual stress tensor ρ_{ij} and, in particular, the deviatoric part of it. In order to do that, a constant tensor, $s^m_{ij} = -dev(\rho_{ij})$, is calculated as that particular s^*_{ij} that solves the minmax problem[22,27]

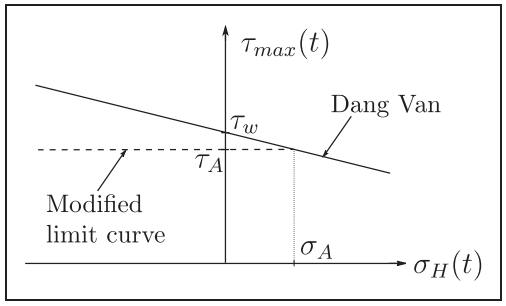

Figure 3. The Dang Van safe locus: the dashed line represents the alternative limit curve, for $\sigma_H(t) < \sigma_A$, here assumed equal to $\sigma_w/3$, as proposed in Ref. 27.

$$\min_{s^*_{ij}}\max_t[(s_{ij}(t) - s^*_{ij})(s_{ij}(t) - s^*_{ij})] \tag{10}$$

Once s^m_{ij} is found, the following stress deviator can be calculated

$$\hat{s}_{ij}(t) = s_{ij}(t) - s^m_{ij} \tag{11}$$

The principal values of this tensor appear in equation (8). The problem in equation (10) is solved iteratively using a move limit approach

$$\min_{s^*_{ij}}\max_t[(s_{ij}(t) - s^*_{ij})(s_{ij}(t) - s^*_{ij})] = \min_{s^*_{ij}}[\max_t \Phi] \tag{12}$$

with

$$\Phi = \Phi(t, s_{ij}(t), s^*_{ij}) \tag{13}$$

Choosing an arbitrary starting value for s^*_{ij}, for example the average deviatoric stress tensor in the stress history for that material point, then for every iteration we identify the maximum value of Φ. Let t_m be the time step at which max Φ happens, then the value of s^*_{ij} is updated

$$s^*_{ij} = s^*_{ij} + ds^*_{ij} \tag{14}$$

with

$$ds^*_{ij} = \gamma(s_{ij}(t_m) - s^*_{ij}) \tag{15}$$

which can be interpreted as a modified steepest descent method. If at one step Φ increases, γ is reduced to 0.25γ. The iteration is stopped if the

norm of the difference between s^*_{ij} at the current iteration step k and at the previous step falls into a tolerance range

$$\|s^*_{ij}|_k - s^*_{ij}|_{k-1}\| < \varepsilon_{tol} \tag{16}$$

Although a superimposed hydrostatic tension has an effect on the fatigue life in normal cyclic loading,[30] several studies[16,31] have shown that a superimposed mean static torsion has little or no effect on the fatigue limit of metals. The independency of the mean shear stress is correctly predicted through the minimization process in equation (10) that leads to the calculation of s^m_{ij}, see also Refs. 27,30.

The Dang Van proposal is equivalent to request, in the $\sigma_H(t) - \tau_{\max}(t)$ plane, that all the representative points of the stress state fall below the line intersecting the $\tau_{\max}(t)$ axis at τ_w with a negative slope of α_{DV}: if all of the points fulfill this requirement, the criterion predicts a safe life for the component (see Figure 3).

The original Dang Van safe locus predicts a detrimental effect of tensile hydrostatic stress while an overoptimistic positive effect is expected under compressive hydrostatic stress. The negative effect of tensile mean stress is well known in literature from classic Haigh diagrams that also show a flat response for negative stress ratios.[32,33] For this reason it is not too conservative to choose a different safe locus in the Dang Van plane to be in agreement with this response, for example a bilinear limit curve, as proposed recently in Ref. 27. The safe locus could be therefore identified in two segments, one with a null slope and the other one with a negative slope equal to α_{DV} (Figure 3). For $\sigma_H(t) \geqslant \sigma_A$ the safe region is identical to the original Dang Van region, while for smaller values of $\sigma_H(t)$, the cutoff with the flat curve replaces the Dang Van limit curve by a curve more on the safe side. Values of $\sigma_A = \sigma_w/3$ and of $\tau_A = \sigma_w/2$ have been proposed in Ref. 27, on the basis of experimental results obtained on high-strength steel smooth specimens. It is possible, if experiments are available to support that, to choose a different set of values for (σ_A, τ_A), but here the same choice has been made as that in Ref. 27. If the ratio of the fatigue limits, τ_w/σ_w, was equal to 0.5, the value α_{DV} in equation (6) would be zero, which is far from reality, as steels usually show ratios between 0.57 and 0.8.[30]

In the following sections, both the original safe locus and a new one with the mentioned cutoff will be used, and results are compared. For τ_w a value of 360 MPa has been imposed[11] and a ratio $\tau_w/\sigma_w = 1/\sqrt{3}$. With this assumption the value of the constant α_{DV} used in the calculations is approximately 0.23. As mentioned in Ref. 11 the value of τ_w here chosen also coincides with the value proposed in the ISO 281:2007,[34] where the fatigue properties for rolling bearings in the VHCF are presented.

For a material point subjected, at time t, to $\sigma_H(t)$ and $\tau_{\max}(t)$, the ratio between $\tau_{\max}(t)$ and the corresponding limit value for that $\sigma_H(t)$ is here used to define the damage factor $n(t)$. Points on the limit curve, then, result in a unit damage factor while points inside the safe region have damage factor smaller than one. As previously mentioned, two different safe loci are here used: one with a linear limit curve and another one with a bilinear limit curve. Consequently, a damage factor is here defined as

$$n(t) = \frac{\tau_{\max}(t)}{\tau_w - \alpha_{DV}\,\sigma_H(t)} \tag{17}$$

if referred to the original Dang Van's safety region or

$$n(t) = \begin{cases} \dfrac{\tau_{\max}(t)}{\tau_w - \alpha_{DV}\,\sigma_H(t)} & \text{if} \quad \sigma_H > \sigma_A \\ \dfrac{\tau_{\max}(t)}{\tau_A} & \text{if} \quad \sigma_H \leqslant \sigma_A \end{cases} \tag{18}$$

when the bilinear limit curve is used. As mentioned earlier, σ_A and τ_A are here chosen equal to $\sigma_w/3$ and $\sigma_w/2$, respectively.

Results and discussion

The Dang Van criterion has been applied to the rolling contact problem and for the geometry previously described, considering three different load cases, either with only p_H, only p_{ehl} or both p_{ehl} and p_t. The load history has been divided in an adequate number of steps so that the distance travelled between two subsequent steps is approximately 3% of the Hertzian contact width. For each time step, the value of the damage factor $n(t)$ has been calculated, both with the original Dang Van limit curve and with the modified one. The maximum value in time

$$n = \max_t n(t) \tag{19}$$

is then chosen as representative for that material point. If this $n < 1$, the prediction is that initiation of fatigue failure will not occur in the material point. The representative points corresponding to the max value of the damage factor are plotted in Figure 4, in the Dang Van region, for all the integration points in the region that goes from the surface of the inner ring to a depth of 1 mm.

In Figure 5 the maximum values of this factor n are plotted against the distance from the surface. Both safe regions, as described before, are used. As we can see, n reaches the highest value in a subsurface region, between 0.14 and 0.17 mm below the surface, depending on the load distribution: this is consistent with experimental observations in literature, where many subsurface initiated failures in bearings for windmill applications are reported. For the two EHL load distributions, the peaks reached by the damage factor n are smaller and closer to the contact surface than in the case with the Hertzian pressure

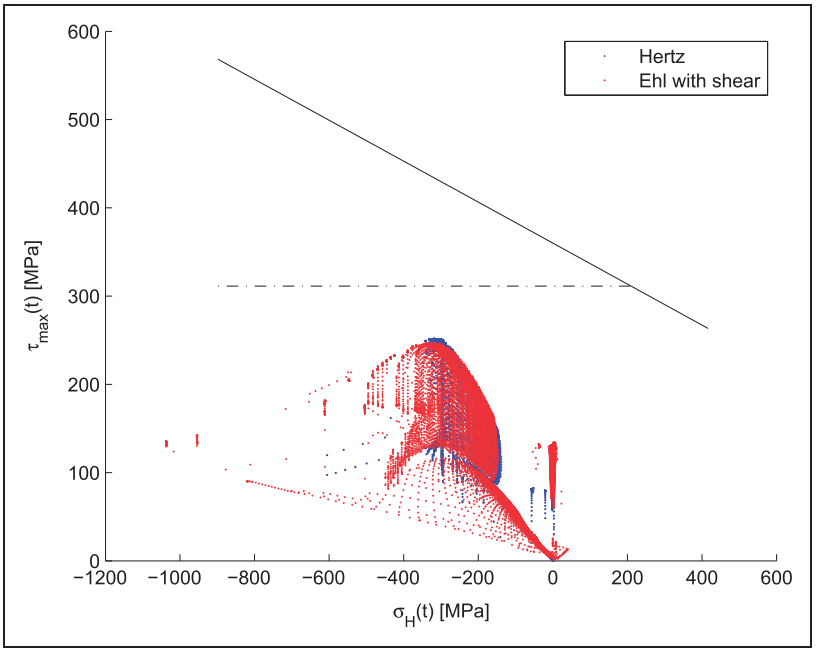

Figure 4. The Dang Van criterion: in order that the failure does not occur, all the representative points should be inside the safe region delimited by the limit curves. In this figure, and for the problem considered, only the representative points corresponding to max value of the damage factor are plotted, for all the integration points in the region analyzed and for both Hertzian and EHL load distributions.

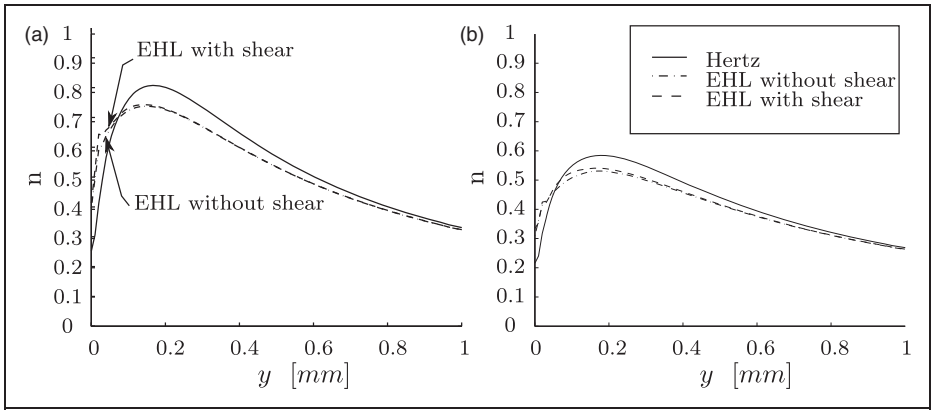

Figure 5. Damage factor versus distance from surface. (a) For the bilinear safe locus, (b) for the original Dang Van safe locus.

distribution. Analogous results are obtained with the use of the original Dang Van safe locus.

The pressure peak here used, $p_0 = 1$ GPa, results in a stress path that in the Dang Van region is rather close to the modified safe locus. If we consider the curve for the Hertz load in Figure 5(a), the peak value of the Dang Van damage factor is approximately 0.807, which corresponds to a safety factor of 1.24. It is seen that the computational method presented here can be used as a design tool, such that the safety factor can be increased by using a smaller value of the pressure peak p_0, a larger length or radius of the roller, or a material more resistant to fatigue. Further calculations, for p_0 equal to 0.8 and 0.5 GPa have been carried out, only for the Hertz distribution, and the results returned values of the safety factor of 1.56 and 2.51, respectively. Therefore, the design tool applied here would suggest a pressure peak not bigger than 0.8 GPa in order to have a reasonable safety factor against fatigue failure.

Hardness variation

The relationships between fatigue strength, the hardness, and the ultimate tensile strength are used in this section to study the influence of the hardness variation in the inner ring.

Since fatigue crack initiation is mainly caused by slip within grains, the yield stress, in the past, has been thought to have the strongest correlation with the

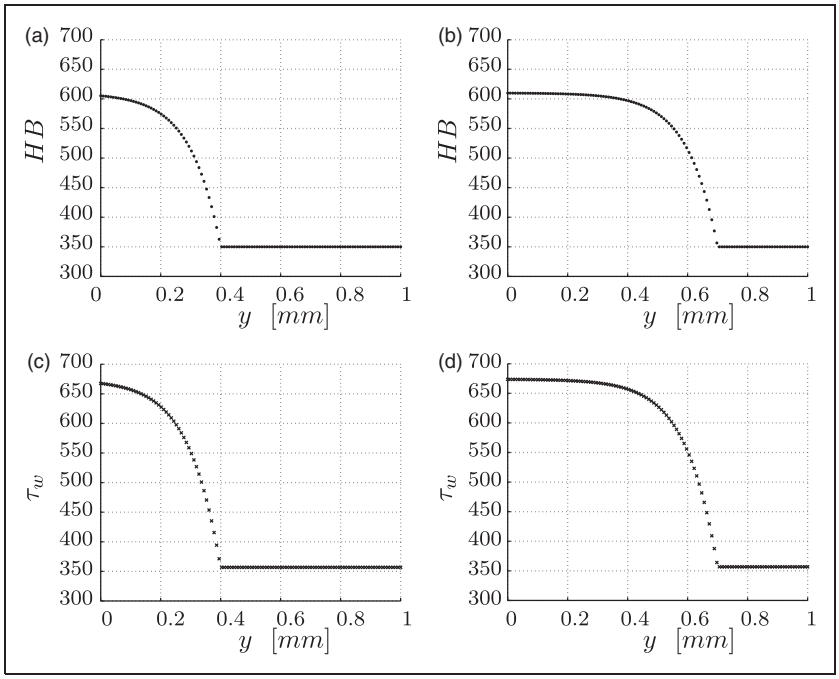

Figure 6. (a), (b) Hardness distributions and (c), (d) correspondent values of τ_w in the first millimeter of depth.

fatigue limit. However, Murakami[35] has found better correlations between tensile strength, hardness, and fatigue limits.

In order to correlate the hardness to the fatigue limit, τ_w, this limit has first been related to σ_{UTS} through an approximate expression proposed in Ref. 36 for low-alloy steels

$$\tau_w = \sigma_w/\sqrt{3} \approx 0.274\,\sigma_{UTS} \tag{20}$$

Denoting the Brinell hardness by HB and using an approximate relationship (see Ref. 37)

$$\sigma_{UTS} = 0.0012\,HB^2 + 3.3\,HB \quad [\mathrm{N/mm^2}] \tag{21}$$

where HB is expressed in $\mathrm{N/mm^2}$, the first coefficient in $\mathrm{mm^2/N}$, and the second coefficient is dimensionless, an approximate final relation between τ_w and HB can be written as

$$\tau_w = 0.274\,(\,0.0012\,HB^2 + 3.3\,HB) \quad [\mathrm{N/mm^2}] \tag{22}$$

Both σ_{UTS} and τ_w in previous equations are expressed in MPa. This procedure was first suggested by Donzella et al.[38,39] In the following we assume that the fatigue limit τ_w is given by expression (22). If another expression $\tau_w(HB)$ applies for a material, this will not in principle change the procedure. In fact, all we need is the value of τ_w in each material point of the solid analyzed.

Different hardness distributions along the depth have been studied here. Thus, the value of τ_w corresponding to the value of the hardness at that depth has been imposed in the material for each Gauss integration point.

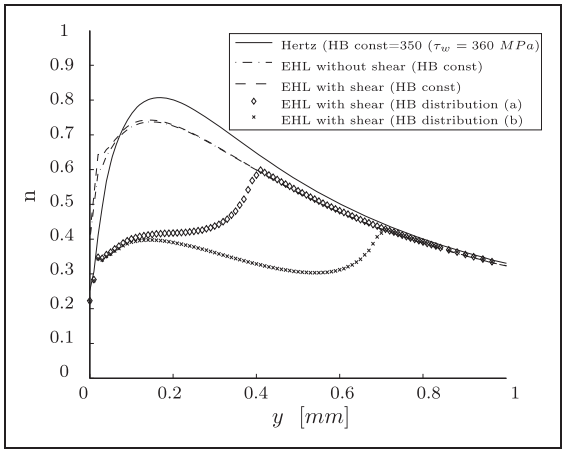

Figure 7. Damage factor versus distance from surface, as results from different load conditions and different hardness variations described in Figure 6. Modified safe locus for the Dang Van criterion was here used.

The two different hardness distributions imposed in the subsurface region of inner ring and the correspondent τ_w distributions are shown in Figure 6(a) and (b). At distances greater than 1 mm from the surface, HB, for both the distributions, is taken to be constant, at a value such that the related fatigue limit, $\tau_w = \tau_w(HB)$, is approximately 360 MPa. This assumption is equivalent to considering how the effect of a surface hardening process would benefit the fatigue response of the bearing. A recent work

by Santos et al.[40] seems to indicate an improvement of fatigue strength, for AISI 52100, by induction heating and repeated quenching, thus validating this assumption. In Ref. 40, measurements presented show a similar step-like hardened profile, with the same peak of hardness here used in Figure 6(a) and (b). Also, fatigue tests performed seem to indicate a similar fatigue limit in pure torsion for the untreated steel and, moreover, an increase of this value after the hardening treatment. It may be noted also that some steels show a maximum for the curve $\tau_w(HB)$, which would limit the applicability of equation (22). In fact, equation (22) is valid only for smaller values of hardness.

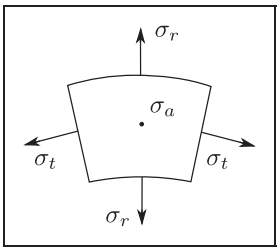

Figure 8. Convention used for the principal stresses in the polar coordinate system.

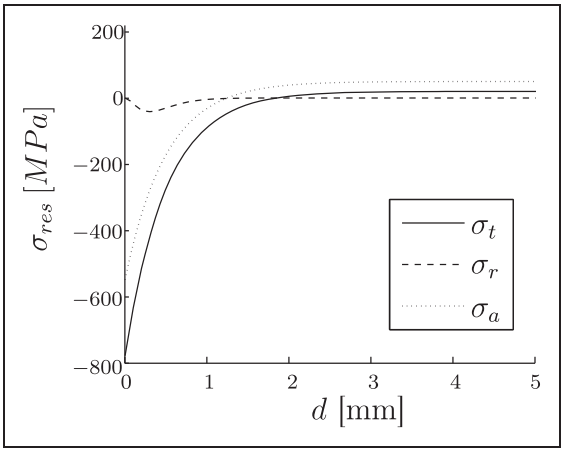

Figure 9. Residual stresses assumed in terms of principal stresses versus the depth d from the ring surface.

Results show that the values of the damage factor n and the depth at which the maximum n is reached are strongly dependent on the particular distribution of hardness imposed (Figure 7). For all the cases analyzed, the peak of the n-curve shifts away from the surface of the inner ring and, for the cases shown in Figure 6(a) and (b), the peak values of n are smaller than the corresponding peaks for a material with uniform hardness. In other words, the rings with extra surface hardening have higher safety against fatigue failure. It should also be noted that the maximum Dang Van damage factor is reached, for the cases analyzed, at the interface between the hardened case and the untreated, softer core material, which is a well-known critical site for subcase failures.

Residual stresses

In order to analyze the influence of preexisting stresses in the bearing, a typical residual stress distribution for the ring has been considered. It is here noted that the Dang Van criterion can only be applied if the residual stresses are preexisting to the fatigue process, e.g. due to the machining or the heating process. In this paper it is assumed that the residual stresses are the results of the heating process when, during the cooling of the component, the material experiences a volume increase due to the phase transformation from austenite to martensite. As the fast cooling, and therefore the phase transformation, starts from the surface and proceeds toward the bulk material, a compressive residual stress distribution is obtained, as the material close to the surface cannot expand as it wishes,

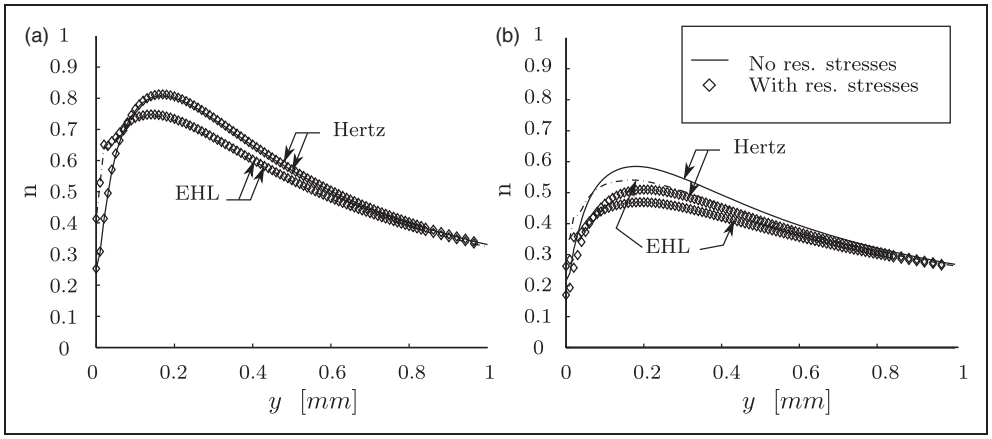

Figure 10. Damage factor versus distance from surface: effect of residual stresses. (a) For bilinear limit curve, (b) for original limit curve.

constrained by the material below. The bearing with an assumed residual stress distribution, equilibrated by an elastic step calculation, is subsequently subjected to the stresses caused by the contact with the roller. The results obtained with the Dang Van criterion are then compared with the results obtained in the bearing free of residual stresses.

In Figure 8 the convention used to name the residual stresses is clarified, while, in Figure 9, the residual stress distribution assumed, in terms of principal stresses, is plotted versus the distance from the surface. Far away from the surface, the residual stresses are assumed to be constant and near zero. The distribution was inspired by experimental results obtained by Voskamp[41] for a deep groove ball bearing.

The results for the two different safe loci are shown in Figure 10. Curves refer to the EHL pressure distribution (we here also include the effect of shear, p_t). The preexisting stress state in the inner ring, in the case of the modified safe locus, has no effect, neither positive nor negative (Figure 10(a)). The residual stresses, in fact, result in a simple shift along the σ_H axis in the Dang Van region (Figure 3) but this does not change the distance from the limit curve since all the most critical material points are subjected to values of σ_H smaller than σ_A and therefore they are in the region where the limit value for $\tau_{\max}$ is constant and equal to τ_A. If the original Dang Van limit curve is used instead, the residual stress distribution from Figure 9 results in a reduction of the maximum damage factor for the compressive residual stresses (Figure 10(b)). This is expected for the original Dang Van model, since the reduced value of σ_H will have a beneficial effect, seen in Figure 3.

Conclusions

The Dang Van criterion has been applied to a roller bearing for windmill applications under different load conditions and the influence of hardness variations and residual stresses has been studied. The effects of both elastohydrodynamic pressure distributions and classic Hertz theory, as applied to the Dang Van multiaxial fatigue criterion, have been analyzed. Shear load has also been applied, together with the EHL normal pressure distribution, to take into account the possible friction experienced by the inner ring.

Results have shown that, according to the Dang Van criterion, the highest damage factor is reached below the surface, regardless of the load distribution and the safe locus used. This suggests that failure is most likely to initiate in the material a little below the surface, which is consistent with experimental observations that report subsurface failures of roller bearings for wind turbine applications. The Hertz distribution resulted in a higher damage factor than the EHL distribution, with or without shear load. Very small differences on results were induced by the presence of the small shear load considered here, indicating a small influence for the criterion used and the assumptions made on its distribution.

The effect of increased hardness, in a thin layer close to the surface, has also been studied, relating the hardness to the fatigue strength of the material. The particular hardness distribution induced is seen to be important in evaluating the safety against fatigue for the bearing. Assuming that a higher fatigue strength corresponds to a higher Brinell hardness, the results indicate that a hardening surface treatment will be beneficial in terms of increased safety against failure.

A bearing with a residual stress distribution has also been studied and the calculations carried out show, for the Dang Van criterion, a positive effect of a compressive residual stresses in the subsurface region according to the original safe locus. No influence of residual stresses has been found with the use of the modified safe locus, for the load cases analyzed.

All the results return a Dang Van damage factor smaller than one, thus indicating a subcritical working condition and an infinite safe life for the component analyzed. On the other hand, typical working conditions for these components, represented by a peak pressure of around 1 GPa, eventually may cause the failure of these elements, which happens often long before the expected life. Reasons for such failures could be overloads during working conditions, e.g. during the engagements of the generator, that may increase the pressure up to 3.1 GPa,[8] beyond the yield limit. Also the material here considered homogeneous is indeed heterogeneous and microstructure alterations in the material close to the interface between the steel and second phase particles can occur, which may demand a more sophisticated approach to study the problem.

The computational procedure presented here results in a damage factor n specified by equation (20). As discussed in the "Results and discussion" section, the inverse, $1/n$, represents the safety factor against fatigue, and the procedure can be used as a design tool by varying the central parameter until an acceptable safety factor is obtained. It is concluded that using a peak pressure p_0 somewhat lower than 1 GPa would be preferable.

Acknowledgements

The author would like to thank Prof. Viggo Tvergaard and Associate Prof. Peder Kilt, Technical University of Denmark, for ideas, discussions, and comments. The work is supported by the Strategic Research Center "REWIND—Knowledge based engineering for improved reliability of critical wind turbine components," Danish Research Council for Strategic Research, grant no. 10-093966.

Funding

This research received no specific grant from any funding agency in the public, commercial, or not-for-profit sectors.

References

1. Arabian-Hoseynabadi H, Oraee H and Tavner PJ. Failure modes and effects analysis (FMEA) for wind turbines. *Int J Electr Power Energy Syst* 2010; 32: 817–824.
2. Amirat Y, Benbouzid MEH, Al-Ahmar E, et al. A brief status on condition monitoring and fault diagnosis in wind energy conversion systems. *Renew Sust Energy Rev* 2009; 13: 2629–2636.
3. Blau PJ, Walker LR, Xu H, et al. *Wear analysis of wind turbine gearbox bearings*. Final Report. Oak Ridge, TN: Oak Ridge National Laboratory, 2010.
4. Smolders K, Feng Y, Long H, et al. Reliability analysis and prediction of wind turbine gearboxes. In: *EWEC—European Wind Energy Conference*, Warsaw, Poland, 20–23 April 2010.
5. Fernandes C, Martins RC and Seabra JHO. Friction torque of cylindrical roller thrust bearings lubricated with wind turbine gear oils. *Tribol Int* 2013; 59: 121–128.
6. Spinato F, Tavner PJ, van Bussel GJW, et al. Reliability of wind turbine subassemblies. *IET Renew Power Gener* 2009; 3(4): 387–401.
7. Yang M, Chengbing H and Xinxin F. Institutions function and failure statistic and analysis of wind turbine. *Phys Procedia* 2012; 24: 25–30.
8. Kotzalas MN and Doll GL. Tribological advancements for reliable wind turbine performance. *Philos T Roy Soc A* 2010; 368: 4829–4850.
9. Sadeghi F, Jalalahmadi B, Slack TS, et al. A review of rolling contact fatigue. *J Tribol* 2009; 131(4): 041403.
10. Ragheb A and Ragheb M. Wind turbine gearboxes technologies. In: *Proceedings of the 1st international nuclear and* renewable *energy conference*, Amman, Jordan, 21–24 March 2010.
11. Lai J, Lund T, Rydén K, et al. The fatigue limit of bearing steels—Part I: A pragmatic approach to predict very high cycle fatigue strength. *Int J Fatigue* 2012; 37: 166–167.
12. Evans M-H. White structure flaking (WSF) in wind turbine gearbox bearings: Effects of 'butterflies' and white etching cracks (WEC). *J Mater Sci Technol* 2012; 28: 3–22.
13. Grabulov A, Petrov R and Zandbergen HW. ESBD investigation of the crack initiation and TEM/FIB analysis of the microstructural changes around the cracks formed under rolling contact fatigue. *Int J Fatigue* 2010; 32: 576–583.
14. Greco A, Sheng S, Keller J, et al. Material wear and fatigue in wind turbine systems. *Wear* 2013; 302(1–2): 1583–1591.
15. Cerullo M. Application of Dang Van criterion to rolling contact fatigue in wind turbine roller bearings. *Proceeding of the 13th International Conference of Fracture – ICF13*, Beijing, China, 16–21 June 2013.
16. Sines G. Behaviour of metals under complex static and alternating stresses. In: G Sines and JL Waisman (eds) *Metal fatigue*. New York: McGraw-Hill, 1959, pp.145–169.
17. Findley WN. A theory for the effect of mean stress on fatigue life of metals under combined torsion and axial load or bending. *Journal of Engineering for Industry* 1959; 81: 301–306.
18. Matake T. An explanation on fatigue limit under combined stress. *Bull JSME* 1977; 20: 257.
19. McDiarmid DL. A shear-stress based critical-plane criterion of multiaxial fatigue failure for design and life prediction. *Fatigue Fract Eng Mater Struct* 1994; 17(12): 1475–1484.
20. Papadopoulos IV. *Fatigue polycyclique des metaux: une nouvelle approche*. PhD Thesis, specialite: Mecanique, Ecole des Ponts et Chaussees, France, 1987.
21. Dang Van K. *Sur la resistance a la fatigue des metaux*. PhD Thesis. Paris: Scientifique et Technologique l'Armement France, 1973.
22. Dang Van K. Macro–micro approach in high-cycle multiaxial fatigue. In: DL McDowell and R Ellis (eds) *Advances in multiaxial fatigue*. ASTM STP 1191. Philadelphia: ASTM, 1993, pp.120–130.
23. Beranger AS, Berard JV and Vittori JF. A fatigue life assessment methodology for automotive components. In: G Marquis and J Solind (eds) *Fatigue Design 1995 Symposium Procedings*, Helsinki. ESIS Publication 22. Elsevier Science, 1997.
24. Bernasconi A, Filippini M, Foletti S, et al. Multiaxial fatigue of a railwheel steel under non-proportional loading. *Int J Fatigue* 2006; 28: 663–672.
25. Ciavarella M, Monno F and Demelio G. On the Dang Van fatigue limiting rolling contact fatigue. *Int J Fatigue* 2006; 28: 852–863.
26. Ciavarella M and Monno F. A comparison of multiaxial fatigue criteria as applied to rolling contact fatigue. *Tribol Int* 2010; 43: 2139–2144.
27. Desimone H, Bernasconi A and Beretta S. On the application of Dang Van criterion to rolling contact fatigue. *Wear* 2006; 260: 568–571.
28. Jacobson BO and Hamrock BJ. Non-Newtonian fluid model incorporated into elastohydrodynamic lubrication of rectangular contacts. *J Tribol* 1984; 106: 275–282.
29. Private communications with Professor P. Klit and S.Janakiraman.
30. Suresh S. *Fatigue of materials*. 2nd edn. New York: Cambridge University Press, 2006, pp.253–254.
31. Davoli P, Bernasconi A, Filippini M, et al. Independence of the torsional limit upon a mean shear stress. *Int J Fatigue* 2003; 25: 471–480.
32. Heywood RB. *Designing against fatigue*. London: Chapman and Hall Ltd, 1962.
33. Dalan TJ. Stress range. In: Horger OJ (ed.) *ASME handbook, metal engineering design*. New York, 1953.
34. ISO 281:2007, Rolling bearings—dynamic load ratings and rating life.
35. Murakami Y. *Metal fatigue: Effects of small defects and nonmetallic inclusions*. Oxford: Elsevier, 2002, pp.5–8.
36. Atzori B, Meneghetti G and Susmel L. Material fatigue properties for assessing mechanical components weakened by notches and defects. *Fatigue Fract Eng Mater Struct* 2005; 28: 83–97.
37. Roessle ML and Fatemi A. Strain-controlled fatigue properties of steels and some simple approximations. *Int J Fatigue* 2000; 22: 495–511.
38. Donzella G, Petrogalli C and Mazzù A. Application of a failure assessment diagram under rolling contact to

components with hardness variable along the depth. *Eng Procedia* 2011; 10: 746–751.
39. Donzella G, Petrogalli C and Mazzù A. A failure assessment diagram for components subjected to rolling contact loading. *Int J Fatigue* 2010; 32: 256–268.
40. Santos EC, Kida K, Honda T, et al. Fatigue strength improvement of AISI E52100 bearing steel by induction heating and repeated quenching. *Mater Sci* 2011; 47(5): 677–682.
41. Voskamp AP. *Microstructural changes during rolling contact fatigue*. PhD Thesis, Technical University of Delft, Netherlands, 1996.

Publication [P3] (Accepted in International Journal of Structural Integrity)

Micromechanical study of the effect of inclusions on fatigue failure in a roller bearing

Micromechanical study of the effect of inclusions on fatigue failure in a roller bearing

Abstract

Purpose In the present paper a set of micromechanical analyses are carried out to study the effect of small inclusions on fatigue life of wind turbine bearings.
Design/methodology/approach The local stress concentrations around an inclusion are determined from a characteristic unit cell model containing a single inclusion, using the approximation of a 2D plane strain numerical analysis. The Dang Van multiaxial fatigue criterion is used for the local stresses in the matrix material, to ensure that the stresses remain within the fatigue limit. The matrix material is taken to be one of the most commonly used bearing steels, AISI 52100, and two different types of inclusions are considered. The macroscopic stress histories applied correspond to either a Hertzian or an elastohydrodynamic (EHL) contact pressure distribution under the rollers.
Findings The paper shows that sub-surface fatigue failure due to rolling contact is more likely to develop close to the inclusion-matrix interface, at particular angles that depend on the material and on the inclusion orientation.
Originality/value Inclusions represent an important issue in the design of wind turbine bearings, that are supposed to work in the very high cycle regime ($N > 10^{11}$ cycles). This paper develops a micromechanical study that provides a deeper understanding on effect of inclusions on the fatigue life, according to one of the most used multiaxial fatigue criteria.
Keywords: Dang Van fatigue criterion, Rolling contact fatigue, Inclusions, Wind Turbine, Elastohydrodynamic lubrication (EHL)
Paper Type: Research paper

Keywords: Dang Van fatigue criterion, Rolling contact fatigue, Inclusions, Wind Turbine, Elastohydrodynamic lubrication (EHL)

1. Introduction

Many criteria have been developed to estimate the fatigue life of bearings (Ioannides and Harris, 1985; ISO, 1989; Lundberg and Palmgren, 1947; Tallian, 1992a,b), but failure still occurs, sometimes long before estimated life (Evans, 2012, 2013; Kotzalas and Doll, 2010). Design of these bearings usually considers the material as homogeneous. However, the material is heterogeneous, since small inclusions are present. Thus, while a standard design would ensure that the average macroscopic stresses in the homogeneous material stay within the stress range where no fatigue occurs, there is also an interest in considering the local stress concentrations around inclusions. These stress concentrations can eventually result in crack nucleation and failure of the component (Evans, 2012; Grabulov et al., 2010; Greco et al., 2013; Sadeghi, 2009). Thus, it is known from experiments that fatigue failure tends to initiate at subsurface inclusions.

In the present paper we carry out a micromechanical study to improve the understanding of the effect of small inclusions on fatigue. For the matrix material we use a multiaxial fatigue criterion, the Dang Van criterion (Dang Van, 1992), to look for the limiting load level below which failure is avoided. During a cyclic stress history this multiaxial fatigue criterion follows the variation of all stress components to ensure that the stress path remains within the fatigue limit. While the Dang Van criterion is proposed for macroscopic stresses, it is reasonable to also expect that the criterion can be used on the micro–level in the small region of stress concentrations around an inclusion in the material. If the solution shows stresses outside the safe region, the external load can be scaled down to find the maximum allowable external load. The method used here is a standard method in the micromechanics of failure, where the analysis of a characteristic unit cell model containing a single inclusion is used to obtain an understanding of the material. Many such cell model analysis have been carried out earlier, e.g. to study ductile fracture or high temperature creep failure (Tvergaard, 1990, 1991, 2012), to study failure of graded composite materials (Reiter et al., 1997), or to study low cycle fatigue in short fiber composites (Tvergaard and Pedersen, 2000). In the present case of roller bearings subject to a very high number of load cycles (10^{11} or more) plastic yielding cannot be allowed, so the stress analyses have to be elastic.

Among several published studies of rolling contact fatigue (Alley and Neu, 2010; Hiraoka et al., 2006; Kabo, 2002; Kuo, 2007; Lai et al., 2012;

Melander, 1997; Slack et al., 2007; Slack and Sadeghi, 2010; Stienon et al., 2009; Weinzapfel and Sadeghi, 2013) some have used the Dang Van criterion on the predicted variations of the macroscopic stresses (Bernasconi et al., 2006; Ciavarella and Monno, 2010; De Simone et al., 2006). This includes (Ciavarella et al., 2006), where the criterion has been discussed in relation to elastic or plastic shakedown. Also a previous study (Cerullo, 2013) has used the Dang Van criterion on the macroscopic stresses in the inner race of a roller bearing, considering either a Hertzian or an elastohydrodynamic (EHL) contact pressure distribution under the rollers, and the stress history has been determined for the point of the inner race where the maximum Dang Van damage factor is reached. In the present micromechanical studies the unit cell model containing an inclusion is taken to be located at the most critical point determined in (Cerullo, 2013), and the macroscopic stress history determined for that point in (Cerullo, 2013) is applied as the boundary conditions on the unit cell.

The matrix material is taken to be AISI 52100, which is one of the most commonly used bearing steels, in which Al_2O_3 inclusions and TiN inclusions occur.The Al_2O_3 inclusions can appear in spherical or ellipsoidal-like shape (Hashimoto et al., 2011). TiN inclusions, which appear in cubic shape and are of smaller size than Al_2O_3 inclusion on average, are considered dangerous for the fatigue life of the material, partly due to the high stress concentrations at sharp corners (Murakami, 2002). However, some authors think that TiN particles play a minor role in the fatigue process of AISI 52100 (Hashimoto et al., 2011), compared to that of Al_2O_3 particles. In the analyses here both the effects of Al_2O_3 inclusions and TiN inclusions are considered, comparing the results in terms of the Dang Van criterion, for different orientations and volume fractions.

2. Problem formulation

In order to study the effect of inclusions on fatigue life, a characteristic rolling stress history has to be evaluated first. Some results from a previous macroscopic study (Cerullo, 2013), have been used here. In (Cerullo, 2013) two different pressure distributions, a static Hertzian normal pressure distribution p_H or an elastohydrodynamic contact pressure distribution p_{ehl}, have been used to model the contact between the roller and the inner race of a roller bearing (Fig. 1). The Hertzian distribution has a peak value of 1 GPa and the EHL distribution is scaled so that it gives the same external load on

the roller. No separate solution for the elastohydrodynamic pressure distribution has been carried out here to obtain p_{ehl}. This pressure distribution is taken from results of Jacobson and Hamrock (Jacobson and Hamrock, 1984), scaled to obtain the wanted load on the roller. Thus, the EHL load applied is considered useful for a parametric study, illustrating the differences between typical p_H loads and typical p_{ehl} loads.

As the Hertzian pressure distribution considered does not include any shear load for a frictionless model, results are here compared with the results for the case of elastohydrodynamic pressure distribution p_{ehl} in absence of shear load. The shapes used for p_{ehl} are indicated in Fig. 1 together with the Hertzian pressure distribution. It is noted that these p_{ehl} shapes, according to (Jacobson and Hamrock, 1984), have a sharp peak at the end of the contact region. Further comparisons are made to investigate also the case where the elastohydrodynamic pressure distribution loads the surface of the inner race and acts together with a shear load p_t, assumed here to be $p_t \simeq 0.1\ p_{ehl}$ just to get an indication of the importance of such shear loads. Therefore three different load cases are analyzed: 1) p_H 2) p_{ehl} and 3) $p_{ehl}+p_t$. Fatigue is then studied by means of the Dang Van multiaxial criterion (Dang Van, 1992) and the point M is determined, where the maximum Dang Van damage factor is reached for the macroscopic stress. The macroscopic stress history in the point M is recorded and this stress history is here subsequently applied to the unit cell with periodic boundary conditions (Fig. 2). The macroscopic stresses found in (Cerullo, 2013) are applied to the representative volume element (RVE) assuming that they are constant along the edges. Also the unit cell is assumed to be so small relative to the bearing geometry that the use of periodic boundary conditions gives a good approximation.

The unit cell is considered to be made of an AISI 52100 bearing steel matrix, in which an inclusion is embedded. Two different types of inclusions are studied here, an Al_2O_3 inclusion and a TiN inclusion. The first type of inclusion is usually found in spherical or ellipsoidal shape (Hashimoto et al., 2011) and here it has been modeled with a circular shape (Fig. 3), as a 2D plane strain calculation is carried out. The second inclusion type, made of TiN, is found in cubic shape, and it is here modeled as a square shaped inclusion (Fig. 3). A small round off at the square corners of the inclusion is introduced to prevent an excessive stress concentration. The values of $E_i/E_m = 1.8523$ and $E_i/E_m = 1.5095$ have been used as ratios between the inclusion and the matrix Young's modulii, for alumina and titanium nitride, respectively. The Poisson's ratio ν_i is taken to be 0.25 for alumina and 0.192

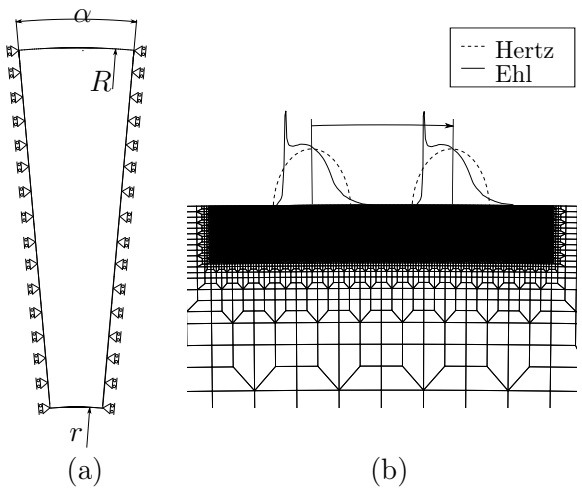

Figure 1: Geometry used in (Cerullo, 2013) to model the contact between the roller and the inner race: $r = 100\ mm$, $R_s = 200\ mm$, $t_k = 19\ mm$, $\alpha = 5°$. On the right, a detail of the mesh used.

for titanium nitride. The matrix has a Young's Modulus $E_m = 210\ GPa$ and a Poisson's ratio $\nu_m = 0.3$.

Different volume fractions have been considered for both types of inclusions. For TiN also the influence of the orientation of the inclusion relative to the surface of the inner ring has been studied. The orientation of the inclusion is specified by the angle ϕ between the axis x_i of the inclusion coordinate system and the axis x_m of the global coordinate system (Fig. 4). The axis x_m is parallel to the tangent of the inner race surface in the nearest contact point, and it is oriented in the rolling direction.

Periodic boundary conditions on the unit cell in Fig. 5 are applied, as described in (Tvergaard, 2012). Along the left and right edges of the cell the BC's are:

$$\begin{array}{rcl} u^1(\xi_1) - u^1_A = u^1(\xi_2) - u^1_B & , & u^2(\xi_1) - u^2_A = u^2(\xi_2) - u^2_B \\ T^1(\xi_1) = -T^1(\xi_2) & , & T^2(\xi_1) = -T^2(\xi_2) \end{array} \tag{1}$$

where ξ_1 and ξ_2 are length coordinates in Fig. 5. Along the top and the bottom of the unit cell the BC's are

$$\begin{array}{rcl} u^1(\eta_1) - u^1_A = u^1(\eta_2) - u^1_D & , & u^2(\eta_1) - u^2_A = u^2(\eta_2) - u^2_D \\ T^1(\eta_1) = -T^1(\eta_2) & , & T^2(\eta_1) = -T^2(\eta_2) \end{array} \tag{2}$$

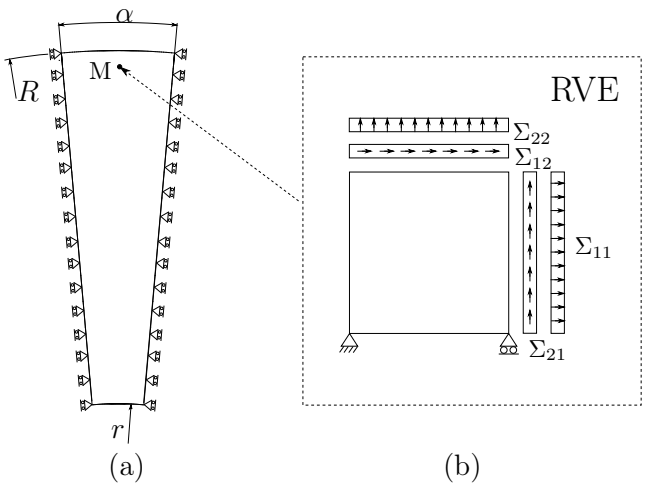

Figure 2: (a) The macroscopic stress history in the point M where the maximum Dang Van damage factor is found (Cerullo, 2013) is applied as boundary condition on the cell model (b).

where η_1 and η_2 are defined in Fig. 5. The displacements of the four corner nodes are denoted u^i_A, u^i_B, u^i_C and u^i_D. In order to prevent rigid body motion, the two displacements u^i_A are chosen equal to zero, and also $u^2_B = 0$. Finally, periodicity requires that $u^i_C = u^i_D + u^i_B$, and therefore only the three displacements u^1_B, u^1_C and u^2_C are free to be prescribed.

Equations (1)-(2) are approximately satisfied using a standard penalty method

$$\begin{aligned} T^i(\xi_2) &= k\big(u^i(\xi_2) - u^i(\xi_1) - u^i_B + u^i_A\big) = -T^i(\xi_1) \\ T^i(\eta_2) &= k\big(u^i(\eta_2) - u^i(\eta_1) - u^i_D + u^i_A\big) = -T^i(\eta_1) \end{aligned} \tag{3}$$

where the stiffness k is chosen large enough to get a good approximation.

In order to apply the macroscopic stress history to the RVE, a superposition method has been used here to relate the macroscopic stresses to the three unknown displacements:

$$\begin{cases} \lambda_{11}\, u^1_B + \lambda_{12}\, u^1_C + \lambda_{13}\, u^2_C = \Sigma_{11} \\ \lambda_{21}\, u^1_B + \lambda_{22}\, u^1_C + \lambda_{23}\, u^2_C = \Sigma_{22} \\ \lambda_{31}\, u^1_B + \lambda_{32}\, u^1_C + \lambda_{33}\, u^2_C = \Sigma_{12} \end{cases} \tag{4}$$

The relation between the stresses and the three displacements is assumed to be linear.

The coefficients λ_{ij} have been evaluated by imposing alternatively a small value for one of the three independent variables, e.g. $0.001\,l$, and at the same time a null value for the other two. For each of the three cases, the macroscopic stresses Σ_{11}, Σ_{22} and Σ_{12} are calculated by integrating the traction vectors along the edges. The unknowns in Eq. (4) reduce to only three and therefore a column vector in the matrix of the coefficients can be evaluated for each case, calculating the coefficient λ_{ij} as the ratio of the macro stress component and the non zero displacement imposed. After three calculations, all the coefficients λ_{ij} are known, and it is possible to solve the system (4). For each time step the three displacements corresponding to the macroscopic stress component are thus calculated from Eq. (4) and these displacements are imposed in the finite element problem.

2.1. Numerical method

In terms of the displacement components u_i on the base vectors the strain tensor is given by

$$\varepsilon_{ij} = \frac{1}{2}\Big(u_{i,j} + u_{j,i}\Big) \tag{5}$$

where $()_{,j}$ denotes partial differentiation. The equilibrium equations, written in terms of the stress tensor σ_{ij} and the strain tensor ε_{ij}, are obtained by the use of the principle of virtual work:

$$\int_V \sigma_{ij}\delta\varepsilon_{ij}dV = \int_S T_i\delta u_i dS \tag{6}$$

where V and S are the volume and surface of the region analyzed, and T_i are the specified surface tractions. The displacement fields are approximated in terms of 8–noded isoparametric elements.

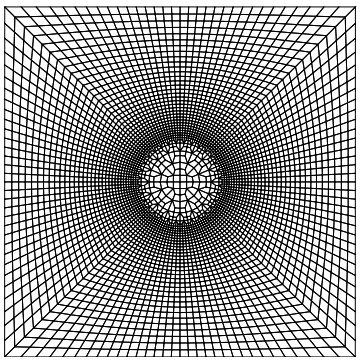

(a)

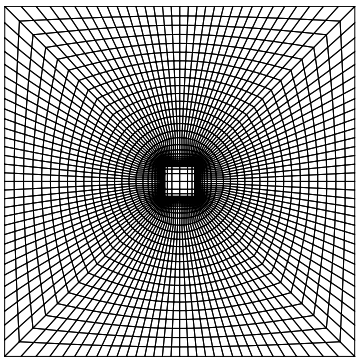

(b)

Figure 3: Example of the different meshes used to model the RVE. (a) Model for Al_2O_3 , with volume fraction $V_f = 0.01$ (b) Model for TiN, with $V_f = 0.001$.

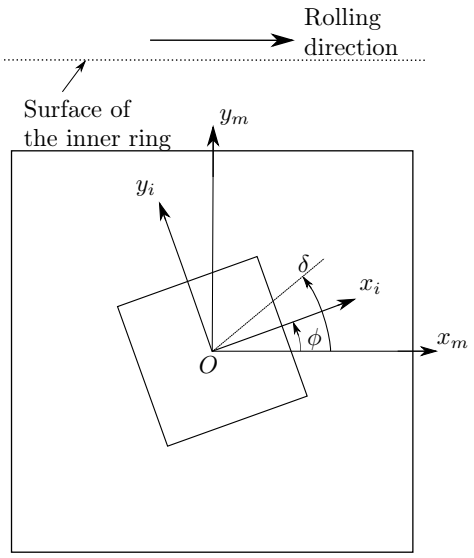

Figure 4: Orientation of the RVE with respect to the contact point on the inner race surface. The angle δ will be used to specify the point where the maximum damage factor is reached. The angle ϕ only applies to the study of TiN inclusions and defines the orientation of the inclusion with respect to the rolling direction.

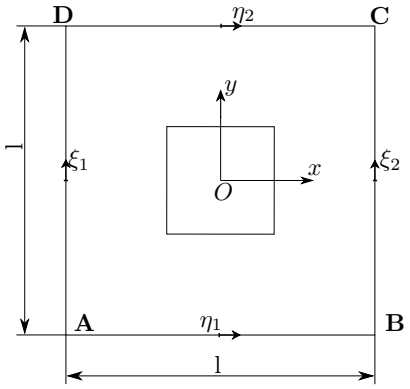

Figure 5: Coordinates for the unit cell analyzed.

3. The Dang Van criterion

A brief introduction to the basis of the fatigue criterion used is given here (see further details in Dang Van (1992) or Cerullo (2013)). The Dang Van criterion is a stress based multiaxial fatigue criterion stating that fatigue is avoided if the following inequality is satisfied throughout the stress history:

$$\tau_{max}(t) + \alpha_{DV}\sigma_H(t) \leq \tau_w \tag{7}$$

Here

$$\alpha_{DV} = 3\left(\frac{\tau_w}{\sigma_w} - \frac{1}{2}\right) \tag{8}$$

is a constant that depends on the fatigue limit in pure torsion, τ_w, and the fatigue limit in pure bending, σ_w. The instantaneous hydrostatic component of the stress tensor is $\sigma_H(t)$ and $\tau_{max}(t)$ is the instantaneous value of the Tresca-like shear stress

$$\tau_{max}(t) = \frac{\hat{s}_I(t) - \hat{s}_{III}(t)}{2} \tag{9}$$

The stress deviator is

$$s_{ij}(t) = \sigma_{ij}(t) - \delta_{ij}\sigma_H(t) \tag{10}$$

and for each material point a constant tensor, s^m_{ij}, is calculated as that particular s^*_{ij} that solves the minmax problem

$$\min_{s^*_{ij}} \max_t [(s_{ij}(t) - s^*_{ij})(s_{ij}(t) - s^*_{ij})] \tag{11}$$

The shifted deviator tensor is then defined as

$$\hat{s}_{ij}(t) = s_{ij}(t) - s^m_{ij} \tag{12}$$

The principal values of the shifted tensor appear in Eq. (9). The problem in Eq. (11) is solved iteratively using a move limit approach (see further details in Cerullo (2013)). The minimization process in Eq. (11) accounts for the independence of fatigue initiation in shear on the mean shear stress, that is well known in literature (see also De Simone et al. (2006); Suresh (2006)).

The Dang Van proposal is equivalent to request, in the $\sigma_H(t)$ - $\tau_{max}(t)$ plane, that all the representative points of the stress state, fall below the

line intersecting the $\tau_{max}(t)$ axis in τ_w with a negative slope of α. If all of the points fulfill this requirement, the criterion predicts a safe life for the component (see Fig. 6).

In order to overcome the over-optimistic prediction under compressive hydrostatic stress, a modified safe locus has been suggested in De Simone et al. (2006). The safe locus is thus identified in two segments, one with a null slope and the other one with the negative slope equal to α (Fig. 6). For $\sigma_H(t) \geq \sigma_A$ the safe region is identical to the original Dang Van region, while for smaller values of $\sigma_H(t)$, the cut-off with the flat curve replaces the Dang Van limit curve by a curve more on the safe side. The values of $\sigma_A = \sigma_w/3$ and of $\tau_A = \sigma_w/2$ proposed in De Simone et al. (2006), on the basis of experimental results obtained on high-strength steel smooth specimens, are also used here. If the ratio of the fatigue limits, τ_w/σ_w, was equal to 0.5, the value α_{DV} in Eq.(7) would be zero, which is far from reality, as steels usually show ratios between 0.57 and 0.8 Suresh (2006).

Only the modified safe locus will be used in the present studies, with $\tau_w = 360\ MPa$ Lai et al. (2012) and a ratio $\tau_w/\sigma_w = 1/\sqrt{3} \approx 0.577$. With this assumption the value of the constant α_{DV} used in the calculations is approximately 0.232.

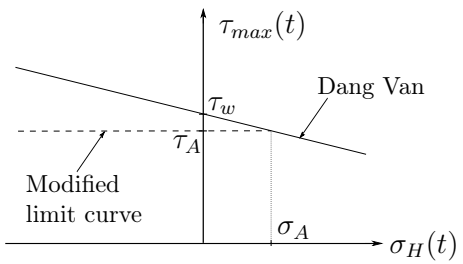

Figure 6: The Dang Van safe locus: the dashed line represents the alternative limit curve, for $\sigma_H(t) < \sigma_A$, here assumed equal to $\sigma_w/3$, as proposed in De Simone et al. (2006).

For a material point undergoing time dependent stress variation, $\sigma_{ij}(t)$, resulting in the stress dependent functions $\sigma_H(t)$ and $\tau_{max}(t)$ in Eq.(7), the ratio between $\tau_{max}(t)$ and the corresponding limit value of τ_{max} at the corresponding value of $\sigma_H(t)$ is here used to define the damage factor $n(t)$ at time t. Points on the limit curve, then, result in a unit damage factor while points inside the safe region have a damage factor smaller than one. An

instantaneous damage factor is defined as

$$n(t) = \begin{cases} \dfrac{\tau_{max}(t)}{\tau_w - \alpha_{DV}\,\sigma_H(t)} & \text{if } \sigma_H > \sigma_A \\ \\ \dfrac{\tau_{max}(t)}{\tau_A} & \text{if } \sigma_H \leq \sigma_A \end{cases} \tag{13}$$

The damage factor n in a material point, is here defined as the maximum value reached by $n(t)$ over the stress history

$$n = \max_t n(t) \tag{14}$$

In the following, it will be assumed that failure would not occur inside the inclusion, but only in the matrix. For this reason, the Dang Van damage factor is only computed and plotted for the matrix.

4. Results

4.1. Volume fraction

Two different macroscopic stress histories, resulting from either the Hertz or the EHL contact pressure distributions in absence of shear load have been applied to the unit cell, for both Al_2O_3 and TiN inclusions (Fig. 7).

Results are shown in Fig. 8, as function of the volume fraction V_f. For the TiN inclusion, results are also presented as function of the orientation of the inclusion with respect to the inner race surface. As the analyses carried out are 2D plane strain conditions, volume fractions have been calculated as the ratio between the area of the inclusion, cylinder for Al_2O_3 and square for TiN, to the area of the cell.

For both the stress histories, regardless of the inclusion type and the volume fraction, the maximum Dang Van damage factor reached in the cell, is always higher than that found in a homogeneous material (macroscopic study) subjected to the same stress history (Cerullo, 2013) ($n_{max} = 0.78$ for EHL and $n_{max} = 0.81$ for Hertz, respectively). In (Cerullo, 2013) in fact it was found that for the load analyzed the maximum damage factor in a homogeneous material subjected to the same macroscopic stress histories was always smaller than the limit value 1, thus indicating a safe life for the component according to the cited criterion. The maximum damage factor is

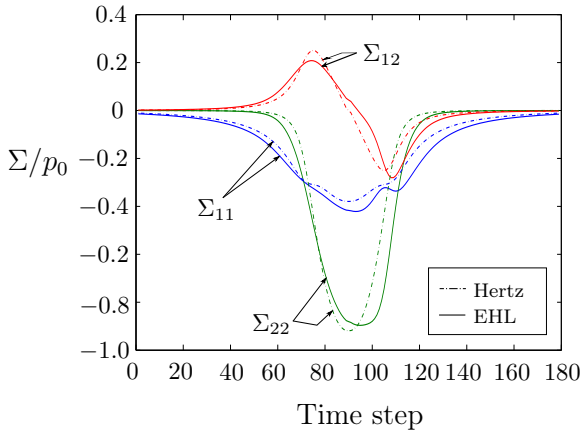

Figure 7: Macroscopic stress histories used in the calculations.

here, in some cases, bigger than one, due to the stress concentrations around the particles with higher Young's modulus. But is should be noticed that the values of σ_w and τ_w used in these computations are experimental values that refer to the macroscopic stress state. Corresponding experimental values referring to stresses on the micro-scale would have to be higher. Therefore, it is possible that the cases analyzed here are still in the safe range, even though some of the n-values found in Fig.8 exceed unity. We note that if a smaller maximum n-value, n_{max}, is chosen for a design, e.g. to have a better safety factor, the maximum load carried by the bearing will have to be reduced, or the bearing will have to be improved. All the curves in Fig. 8 show a decreasing trend as function of the volume fraction, such that a safer life corresponds to a bigger inclusion. This prediction may be a result of the inclusions reinforcing the unit cell, so that a larger inclusion reduces the stress peaks in the matrix.

For both Hertz and EHL stress histories in Fig. 7, the curve referring to the Al_2O_3 in the following figures is in most of the cases above the curves for TiN. This is due to the larger difference in Young's moduli for the Al_2O_3 . The shape of the inclusion, and in particular the stress concentration at the TiN corners, is therefore found to be less important than the stress concentration resulting from different material properties between matrix and inclusion. However, differences are rather small. The rounding radius used here is equal to $\gamma\, l_{cub}$, where $\gamma = 0.15$ and l_{cub} is the half width of the inclusion.

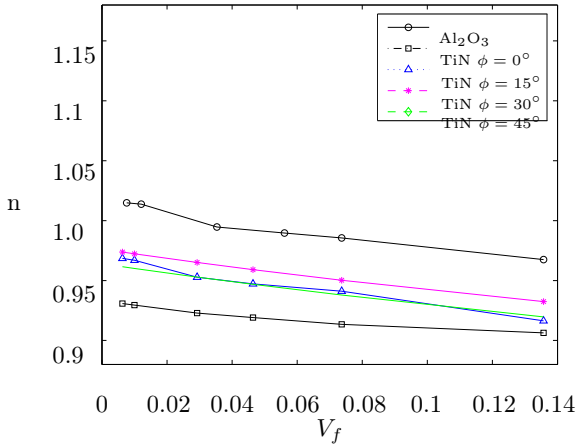

(a)

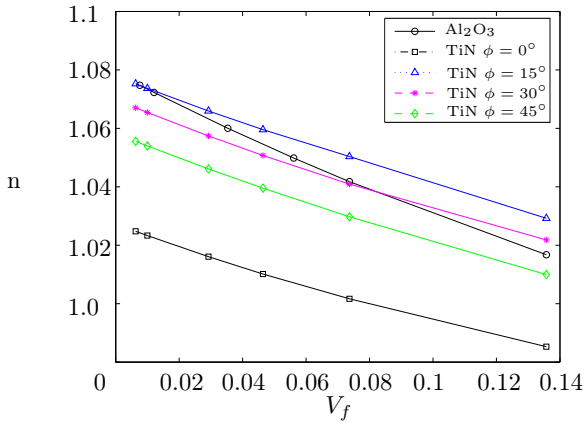

(b)

Figure 8: Maximum Dang Van damage factor reached in the matrix, for different inclusions, as function of volume fraction. The load histories applied to the cell result from (a) Hertz contact pressure and (b) EHL contact pressure on the inner race in absence of shear load (See Fig. 7).

Results for other values of γ, for some cases, and for the Hertz load history, are presented in Table 1. As the value of γ decreases, the maximum damage

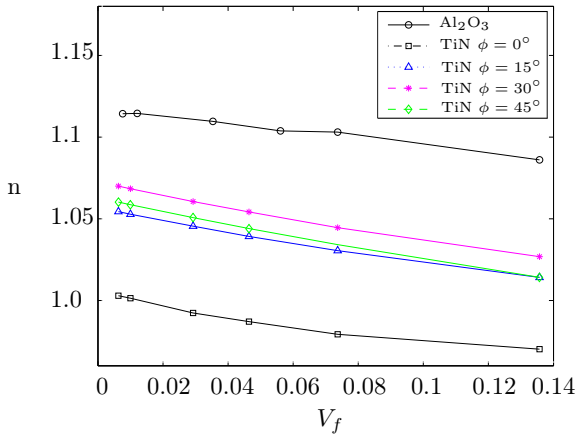

Figure 9: Maximum Dang Van damage factor reached in the matrix, for different inclusions, as function of volume fraction. The load history is generated by EHL pressure distribution acting on the inner race, with the shear load.

factor increases, since a more severe stress concentration is introduced. The value of 0.15 has been chosen as a compromise between the need of a small rounding radius, ideally zero, and a mesh not too distorted in the region close to the radius. It is noted that a sharp corner of the inclusion would result in a stress singularity, as has been analyzed by Tvergaard and Hutchinson (Tvergaard and Hutchinson, 1988) for the case of a ceramic with different grain properties.

A mesh convergence investigation was carried out for both Al_2O_3 and TiN inclusions, for 2 different volume fractions, $V_{f1} = 0.007$ and $V_{f2} = 0.073$, and for a Hertz stress history. The TiN inclusion was investigated for two different angles, $\phi = 0°$ and $\phi = 30°$. The number of elements along the interface N_{int} between the matrix and the inclusion was doubled from 64 to 128 and, accordingly, the number of elements increased from 4972 to 9964 in the case of Al_2O_3 and from 3768 to 11768 for the TiN. It is noted that the element aspect ratio at the interface is kept fixed, so the increased number of elements around the particle also gives smaller elements in the radial direction. Results, listed in Table 2, show that there is little mesh

dependence, and that the discretization used in the analysis, with 64 elements along the interface and a much smaller number of elements, gives sufficient accuracy. In fact the percentage difference is of the order of 0.5%.

Table 1: Maximum Dang Van damage factor reached in the matrix, for different sizes of the rounding radius and two different orientations of a TiN inclusion. Results are shown for the Hertz stress history, corresponding to Fig. 7. $V_{f1} = 0.0063$, $V_{f2} = 0.0292$.

	0°		30°	
γ	V_{f1}	V_{f2}	V_{f1}	V_{f2}
0.20	0.9299	0.9221	0.9703	0.9618
0.15	0.9308	0.9228	0.9737	0.9651
0.10	0.9324	0.9245	0.9779	0.9692
0.05	0.9338	0.9259	0.9815	0.9727

Table 2: Mesh convergence analysis results in terms of the maximum Dang Van damage factor reached in the matrix. Hertzian stress history of Fig. 7 was here used. $V_{f1} = 0.007$, $V_{f2} = 0.073$. N_{int} represents the number of elements along the interface between the matrix and the inclusion.

	Al_2O_3		TiN ($\phi = 0^\circ$)		TiN ($\phi = 30^\circ$)	
N_{int}	64	128	64	128	64	128
V_{f1}	1.0137	1.0077	0.9294	0.9200	0.9723	0.9561
V_{f2}	0.9896	0.9875	0.9191	0.9225	0.9590	0.9581

For a TiN inclusion, the damage factor for ϕ between 15° and 30° degrees is in most cases higher than for other orientations. This is always true for the EHL load history (Fig. 8b) and is true for most of the volume fractions under the Hertz load history (Fig. 8a). Apparently this particular orientation is the most dangerous for this kind of inclusion.

In (Cerullo, 2013) it was found that a Hertz stress history results in a higher Dang Van damage factor than the EHL distribution. In the present study, instead, all the curves from Hertz load history in Fig. 8a fall below the corresponding curves for EHL history in Fig. 8b.

To investigate the effect of the shear load, the results for the case of the EHL load history with the shear load p_t are shown in Fig. 9. It is noted that

the curves in Fig. 9 are similar to the corresponding curves for EHL without shear of Fig. 8b. In some cases, as the alumina and the titanium nitride for $\phi = 30°$ and $\phi = 45°$, the shear load increases the maximum damage factor, while the opposite happens for the other curves. The orientations $\phi = 15°$ and $\phi = 30°$ are still the most dangerous, though the one for $\phi = 45°$ is here comparable. Differences between the corresponding curves for the case that incorporates or neglects the shear are rather small, with the exception of the alumina. Thus, accounting for a shear load due to EHL has only a small effect.

4.2. Distribution of the damage factor in the cell

In Fig. 10 the contour plot for the Dang Van maximum damage factor is shown, for an alumina inclusion with $V_f = 0.012$, for two different stress histories. In Fig. 10a it is seen that the Hertzian load history results in a completely symmetric distribution, with small zones of high damage factor located at the inclusion–matrix interface, at the intersection with the two axes of symmetry. The highest damage factor is reached at $\delta = \pm 11.8°$, in a region almost parallel to the rolling direction. The same values are reached in the symmetric lower half part of the cell. In fig 10b, which refers to an EHL stress history in absence of shear load, the symmetry of the contour is lost. The maximum damage factor is still located at the interface with the inclusion, but it is reached at an angle of $\delta = 84.9°$. The areas of high damage factor are still close to the interface, but they are a bit rotated and located in a band approximately oriented at 45° to the overall rolling direction, see Fig. 10b. This result seems to indicate that in this direction, failure is more likely to occur.

Rather small differences in the damage factor distribution have been found for EHL stress history with or without shear load and therefore in the following figures we will refer to the case which includes the shear. Furthermore, as failure is assumed to happen in the matrix rather than in the inclusion, contour plots are only presented for the matrix. Analyses for different values of the volume fraction V_f show distributions of the damage factor n around the particles similar to those shown in Fig. 10. In Fig. 11 the results for a TiN inclusion with $V_f = 0.01$ and $\phi = 0°$ are shown. As for alumina, the zone of highest damage factor is found at the interface between the inclusion and the matrix, or very close to it. For the Hertzian stress history the highest Dang Van damage factor is reached in the zones that start from the four corners of the inclusion (Fig. 11a), while for the EHL stress

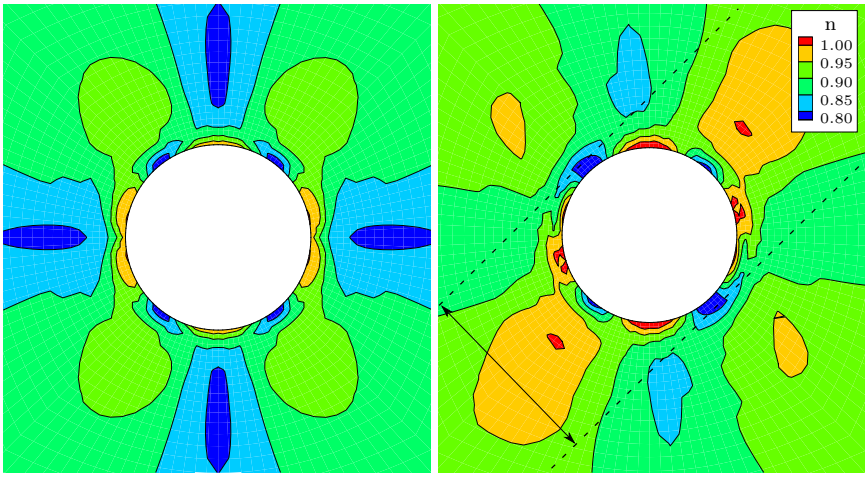

(a) (b)

Figure 10: Maximum Dang Van damage factor distribution in the matrix (a) Hertz (b) EHL without shear load. $V_f = 0.012$. A zoom at center of cell.

history it is reached close to the rounding radius of the inclusion. However differences between the highest n and the sourrounding zones, for both cases, are small, thus indicating that stress concentration dominates. If the RVE is subjected to the EHL load history, a zone with high damage factor is found in a band approximately oriented at 45°, as already seen for the alumina.

As the angle ϕ that defines the orientation of the inclusion increases, for Hertzian stress history, the max n is reached at the interface with the inclusion, at all 4 corners (Fig. 12). For the EHL stress history, instead, only the corners in the first and third quadrant have very high values of n. These peaks are however highly localized and zones of high Dang Van damage factor are still found close to the other two corners.

The maximum von Mises stress, for the alumina, is reached, in the case of Hertzian stress history, at the time step 90 in Fig. 7, i.e. when the roller is exactly above the inclusion and $\Sigma_{12} = 0$. For the EHL stress history without shear load, instead, the maximum von Mises stress is reached at a time which depends on the inclusion size but which is always very close to time step 108 in Fig. 7, i.e. when the macroscopic shear stress is close to its negative maximum. Analogous considerations can be made for the titanium nitride inclusion.

In the case of a stress history that accounts for the shear load on the inner

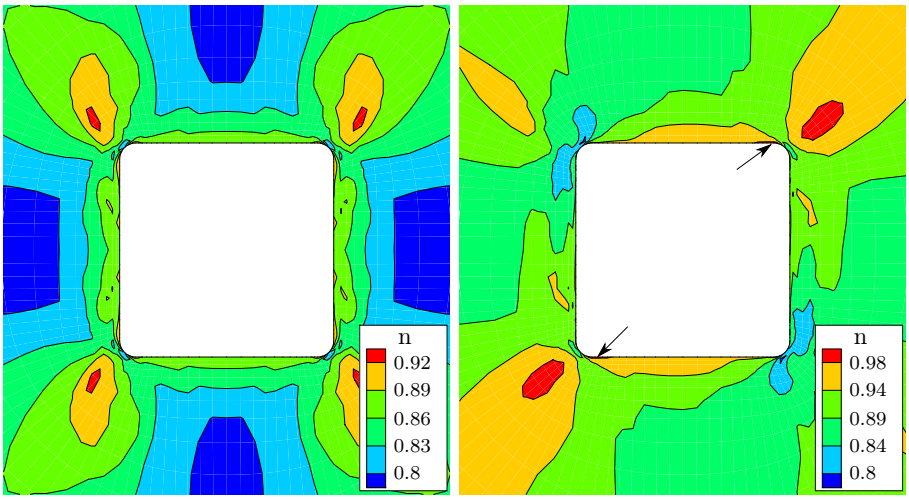

(a) (b)

Figure 11: Dang Van maximum damage factor for a TiN inclusion for (a) Hertz and (b) EHL stress history with shear load. $\phi = 0°$, $V_f = 0.01$. In (b) arrows indicate zones where the highest values of n are reached. A zoom at center of cell.

race, results are similar to those found in absence of shear load. The maximum von Mises stress is reached typically at time step 109 in Fig. 7, both for alumina inclusions and for titanium nitride inclusions. Small variations are due to different orientations of the inclusions. The maximum von Mises stress ranges, for alumina, are between $0.24\,\sigma_y$ and $0.40\,\sigma_y$, depending on the volume fraction and on the stress history applied; for TiN, the effective stress range from $0.32\,\sigma_y$ to $0.33\,\sigma_y$. The value used here for σ_y is 1960 MPa (Hashimoto et al., 2011).

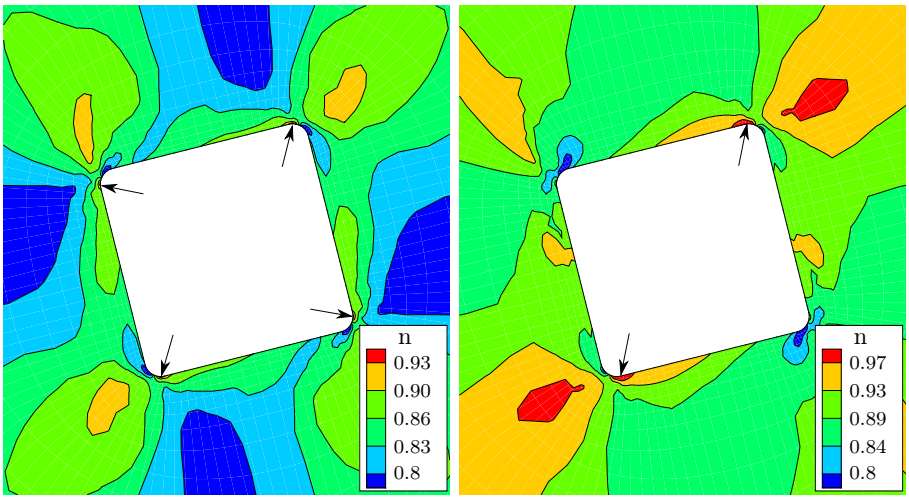

(a) (b)

Figure 12: Dang Van maximum damage factor for a TiN inclusion for (a) Hertz and (b) EHL stress history with shear load. $\phi = 15°$, $V_f = 0.01$. Arrows indicate zones where the highest values of n are reached. A zoom at center of cell.

5. Conclusion

Several experimental investigations (Evans, 2012, 2013; Grabulov et al., 2010; Greco et al., 2013; Sadeghi, 2009) have shown that failure in rolling contact fatigue tends to initiate below the surface, at inclusions, e.g. as so-called butterfly fracture. Here we have used a micromechanical approach to estimate the locations around inclusions that will be most critical for the initiation of fatigue failure, and the loads at which fatigue will initiate. As the wind turbine roller bearings considered will be subjected to a very high number of cycles ($> 10^{11}$), we use a multiaxial fatigue criterion to ensure that the stress cycles in the structural alloy around the inclusion do not exceed the fatigue limit. The Dang Van criterion is a well established method for ensuring that a componenent will avoid fatigue failure if the stress variations stay within the safe locus. The peak values found for the damage factor n also indicate the locations in the material where failure is most likely to initiate. Thus, the present analyses are used to determine where micro–cracks are expected to form, and this information will be used in a subsequent paper to investigate, in a finite element analysis, micro–cracks propagation under rolling contact fatigue.

The Dang Van criterion is here applied on a micro level to a material subject to different rolling contact stress histories, resulting from a simple Hertzian load or from an EHL pressure distribution acting on the surface of the inner race of a bearing. A 2D plane strain finite element analysis is carried out, where either Al_2O_3 inclusions or TiN inclusions are embedded in an AISI 52100 bearing steel matrix. A unit cell model containing a single inclusion is subjected to a macroscopic stress history earlier calculated (Cerullo, 2013). Different volume fractions have been investigated and, for the TiN inclusions, the orientation of the inclusion relative to the inner race of the bearing has also been studied. Results show that, regardless of the specific stress history investigated, the highest damage factor is always reached at the interface between the inclusion and the matrix or in a region very close to it, so these are the locations where the first formation of micro–cracks would be expected, if too high load is applied to the bearing. Moreover, for the EHL stress history, zones of high maximum damage factor are reached in a band oriented approximately at 45° to the overall rolling direction. For the TiN inclusion, these regions of high damage factor still remain, but also isolated peaks are found at corners.

The elastic stress distribution around particles will show a singularity

if the inclusion has a sharp corner, as has been shown in detailed analyses by Tvergaard and Hutchinson (1988). Thus, cyclic plasticity could not be avoided if particles have completely sharp corners. In the present analyses it has been assumed that the TiN particles have rounded corners.

For a given V_f a higher maximum damage factor is practically always reached in the matrix with an alumina inclusion rather than with a titanium nitride inclusion. This is as expected, since the alumina has a higher E_i/E_m ratio than that of the titanium nitride, and the elastic stress concentrations around the inclusions are entirely driven by the mismatch of elastic properties.

References

Alley, E. S. and Neu, R. W. (2010), "Microstructure-sensitive modeling of rolling contact fatigue", International Journal of Fatigue Vol. 32, pp. 841–850.

Bernasconi, A. and Filippini, M. and Foletti, S. and Vaudo, D. (2006), "Multiaxial fatigue of a railway wheel steel under non–proportional loading", Int J Fatigue, Vol. 28, pp. 663–672.

Cerullo, M. (2013), "Application of Dang Van criterion to rolling contact fatigue in wind turbine roller bearings under elastohydrodynamic lubrication conditions", P I Mech eng C-J Mec, Prepublished December 20th 2013, DOI 10.1177/0954406213516946.

Ciavarella, M. and Monno, F. and Demelio, G. (2006), "On the Dang Van fatigue limitin rolling contact fatigue", Int J Fatigue Vol. 28, pp. 852–863.

Ciavarella, M. and Monno, F. (2010), "A comparison of multiaxial fatigue criteria as applied to rolling contact fatigue", Tribology International, Vol. 43, pp. 2139–2144.

Dang Van, K. (1971), "Sur la résistance à la fatigue des métaux", Thèse de Doctorat ès Sciences. Paris: Scientifique et Technologique l'Armement.

Desimone, H. and Bernasconi, A. and Beretta, S. (2006), On the application of Dang Van criterion to rolling contact fatigue, Wear, Vol. 260, pp. 568–571.

Evans, M. -H. (2012), "White structure flaking (WSF) in wind turbine gearbox bearings: effects of 'butterflies' and white etching cracks (WEC)", Journal of Materials Science and Technology, Vol. 28, pp. 3–22.

Evans, M. -H., Richardson, A. D. and Wang, L. Wood, R. J. K. (2013), "Serial sectioning investigation of butterfly and white etching crack (WEC) formation in wind turbine gearbox bearings", Wear of Material, Vol. 302, Issue 1-2, pp. 1573-1582.

Grabulov, A., Petrov, R. and Zandbergen, H. W. (2010), "ESBD investigation of the crack initiation and TEM/FIB analysis of the microstructural changes around the cracks formed under Rolling Contact Fatigue", International Journal of Fatigue, Vol. 32, pp. 576–583.

Greco, A., Sheng, S., Keller, J. and Erdemir, A. (2013), "Material wear and Fatigue in Wind Turbine Systems", Wear, Vol. 302, Issues 1-2, pp. 1583-1591.

Hashimoto, K., Fujimatsu, T., Tsunekage, N., Hiraoka, K., Kida, K. and Costa Santos, E. (2011), "Study of rolling contact fatigue of bearing steels in relation to various oxide inclusions", Materials and Design, Vol. 32, pp. 1605–1611.

Hiraoka, K., Nagao, M. and Isomoto, T. (2006), "Study on Flaking Process in Bearings by White Etching Area Generation", Journal of ASTM International, Vol. 3, Issue 5.

Ioannides, E. and Harris,T. A. (1985), "A new fatigue life model for rolling bearings", ASME J Tribol Vol. 107, pp. 367–377.

ISO, 1989. Rolling bearings - Dynamic load ratings and rating life. Draft International Standard ISO/DIS 281, ISO, Geneva, Switzerland.

Jacobson, B. O. and Hamrock, B. J. (1984), "Non-Newtonian Fluid Model Incorporated Into Elastohydrodynamic Lubrication of Rectangular Contacts", Journal of Tribology, Vol. 106, pp. 275–282.

Kabo, E. (2002), "Material defects in rolling contact fatigue – influence of overloads and defects clusters", Int. Journal of fatigue Vol. 24, pp. 887–894.

Kotzalas, M. N. and Doll, G. L. (2010), "Tribological advancements for reliable wind turbine performance", Philosophical Transactions of the Royal Society A, Vol. 368, pp. 4829–4850.

Kuo, Chang-Hung (2007), "Stress disturbances caused by the inhomogeneity in an elastic half-space subjected to contact loading", International Journal of Solids and Structures, Vol. 44, pp. 860–873.

Lai, J., Lund, T., Rydén, K., Gabelli, A. and Strandell, I. (2012), "The fatigue limit of bearing steels – Part I: A pragmatic approach to predict very high cycle fatigue strength", Int. Journal of Fatigue, Vol. 37, pp. 166–167.

Lundberg, G. and Palmgren,A. (1947), "Dynamic capacity of rolling bearings", Acta Polytechnica, Mech. Eng, Series 1:3.

Melander, A. (1997), "A finite element study of short cracks with different inlcusion types under rolling contact fatigue load", Int. J. Fatigue, Vol. 19, pp. 13–24.

Murakami, Y. (2002), "Metal Fatigue: Effects of Small defects and Nonmetallic Inclusions", Elsevier, Oxford.

Reiter, T., Dvorak, G. J. and Tvergaard, V. (1997), "Micromechanical models for graded composite materials", Journal of the Mechanics and Physics of Solids, Vol. 45, Issue 8, pp. 1281–1302.

Sadeghi, F., Jalalahmadi, B., Slack, T. S., Raje, N. and Arakere, N. K. (2009), "A Review of Rolling Contact Fatigue", Journal of Tribology, Vol. 131, Issue 4, 041403-1.

Slack, T., Raje, N., Sadeghi, F., Doll, G. and Hoeprich, M. R. (2007), "EHL Modeling for Nonhomogeneous Materials: The Effect of Material Inclusions", Journal of Tribology, Vol. 129, pp. 256–273.

Slack, T. and Sadeghi, F. (2010), "Explicit finite element modeling of subsurface initiated spalling in rolling contacts", Tribology International, Vol. 43, pp. 1693–1702.

Stiénon, A., Fazekas, A., Buffière, J.-Y. (2009), "A new methodology based on X-ray micro-tomography to estimate stress concentrations around inclusions in high strength steels", Material Science and Engineering A, Vol. 513, pp. 513–514.

Suresh, S. (2006), "Fatigue of materials", Cambridge University Press.

Tallian, T. E. (1992a), “Simplified Contact Fatigue Life Prediction Model–Part I: Review of Published Models”, ASME J Tribol, Vol. 114, pp. 207–213.

Tallian, T. E. (1992b), “Simplified Contact Fatigue Life Prediction Model–Part II: New Model”, ASME J Tribol, Vol. 114, pp. 214–222.

Tvergaard, V. and Hutchinson, J. W. (1988), ”Microcracking in Ceramics Induced by Thermal Expansion or Elastic Anisotropy“, J Am Ceram Soc, Vol. 71, Issue 3, pp. 157–166.

Tvergaard, V. (1990), ”Material failure by void growth to coalescence“, Advances in applied mechanics, Vol. 27, pp. 83–151.

Tvergaard, V. (1991), ”Micromechanical modeling of creep-rupture“, Journal of Applied Mathematics and Mechanics, Vol. 71, Issue 4, pp. T23–T32.

Tvergaard, V. and Pedersen, T.O. (2000), ”Fatigue crack evolution in a metal reinforced by short fibres“, Archives of Mechanics Vol. 52 No 4-5, pp. 799–815.

Tvergaard, V. (2012), ”Effect of stress-state and spacing on voids in a shear-field“, International Journal of Solids and Structures, Vol. 49, Issue 22, pp. 3047–3054.

Weinzapfel, N. and Sadeghi, F. (2013), ”Numerical modeling of sub-surface initiated spalling in rolling contacts“, Tribology International, Vol. 59, pp. 210–221.

Publication [P4]

Sub-surface fatigue crack growth at alumina inclusions in AISI 52100 roller bearings

Available online at www.sciencedirect.com

ScienceDirect

Procedia Engineering 74 (2014) 333 – 338

Procedia Engineering

www.elsevier.com/locate/procedia

XV11 International Colloquim on Mechanical Fatigue of Metals (ICMFM17)

Sub-surface fatigue crack growth at alumina inclusions in AISI 52100 roller bearings

Michele Cerullo*

Technical University of Denmark, Department of Mechanical Engineering Nils Koppels Alle, 2100 Lyngby - Denmark

Abstract

Sub-surface fatigue crack growth at non metallic inclusions is studied in AISI 52100 bearing steel under typical rolling contact loads. A first 2D plane strain finite element analysis is carried out to compute the stress history in the innner race at a characteristic depth, where the Dang Van damage factor is highest. Subsequently the stress history is imposed as boundary conditions in a periodic unit cell model, where an alumina inclusion is embedded in a AISI 52100 matrix. Cracks are assumed to grow radially from the inclusion under cyclic loading. The growth is predicted by means of irreversible fatigue cohesive elements. Different orientations of the cracks and different matrix-inclusion bonding conditions are analyzed and compared.

Selection and peer-review under responsibility of the Politecnico di Milano, Dipartimento di Meccanica
Keywords: Rolling contact fatigue; AISI 52100; Inclusions; Wind Turbine; Cohesive Element

1. Introduction

It is well known that fatigue failure and mechanisms may vary a lot according to the stress level applied and that a dual step S–N curve characteristic may appear in the ultra long life regime [1–5]. At stress levels close or higher than the conventional fatigue limit, in fact, failure is more likely to be expected close to the surface of the material, while at a stress level below the fatigue limit, fatigue failure usually occurs at small internal defects. The latter mechanism becomes dominant in the very high cycle fatigue (VHCF), that is to say for a number of cycles bigger than 10^{11}, while a coexistence of surface and subsurface failures is present in the range between 10^6–10^9 cycles [2–6].

Subsurface failure is usually dominated by crack initiation, which is strongly influenced by the features and the defects in the microstructure [6]. Inclusions or pores may act as stress concentration sites, and cracks may nucleate around these defects and then propagate to the surface. Sometimes microstructural changes are observed around inclusions, where a fine granular area, known as fish-eye, may develop for low stress amplitudes [3,4,7–9].

Traditional approaches against rolling contact fatigue (RCF) consist in designing with respect to a maximum Hertzian pressure [10], or by means of multiaxial fatigue criteria, as the Dang Van criterion [11], which has been widely used for decades [12]. Though these approaches may be more practical, they somehow neglect the complexity of the VHCF mechanisms. Service life in the VHCF regime is in fact strongly influenced by the presence of small inclusions, and therefore other design criteria have been proposed, as calculations based on the stress intensity factor (SIF) [13] or by means of the Murakami's method [14].

The study of fatigue failure in the high and very high cycle regime is of extreme importance in those applications, as for example wind turbine roller bearings, where any failures of the mechanism reflect in down-time costs which

*Corresponding author. Tel.: +45 45254278; fax: +45 45931475; mcer@mek.dtu.dk.

Selection and peer-review under responsibility of the Politecnico di Milano, Dipartimento di Meccanica
doi:10.1016/j.proeng.2014.06.274

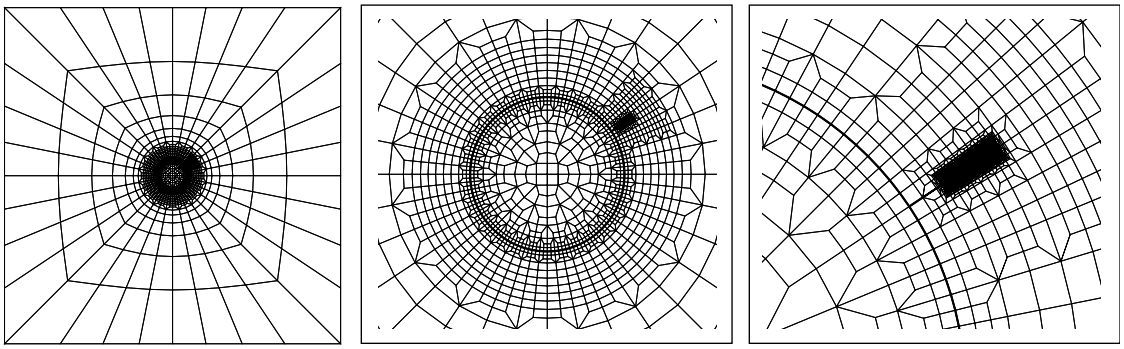

(a) (b) (c)

Fig. 1: Mesh used for the calculations at full scale (a) and at different levels of detail (b)-(c). In (c) the mesh around the crack is shown. $\theta = 30°$

.

have to be minimized [15,16]. For these mechanical systems, in fact, a service life as long as 20 years, equivalent to more than 10^{11} cycles, is expected [17], but failure sometimes occurs long before this design life.

In this work rolling contact fatigue at an interior Al_2O_3 inclusion in a AISI 52100 roller bearing is investigated. The study assumes that a small crack has already nucleated in the matrix, close to the inclusion, and therefore the crack initiation process and time are neglected. The focus is here on the influence of the inclusion depth and on the angle of the crack relative to the rolling surface. The characteristic rolling contact stress history is computed in a previous work [18] and is applied here as periodic boundary conditions. The fatigue crack growth is modelled by irreversible cohesive elements [19] and the results are compared in terms of number of cycles.

2. Problem formulation

In [18] a plane strain finite element model of a bearing ring in contact with a roller was investigated, substituing the roller with the equivalent Hertzian load, and a characteristic rolling contact stress history was recorded, at the depth of maximum Dang Van damage factor.

The macroscopic stress history $\Sigma_{ij}(t)$ is here imposed as periodic boundary condition to a unit cell of AISI 52100, in which a circular inclusion of Al_2O_3 is embedded. A straight initial crack starting from the inclusion-matrix interface is present in the matrix, at a fixed angle for each calculation. Fatigue crack growth is modelled by means of cohesive elements alligned along a straight path. Thus, the crack is assumed to grow without kinking.

In order to decrease the computational expense, the stress history, initially recorded in [18] using 179 points. It has been found that an interpolation using only 12 points gives sufficient accuracy. Between each time steps, a number of 200 increments has been used for the calculations.

The cohesive elements are described by the Roe-Siegmund irreversable constituive law [19] that models the fatigue crack growth incorporating a damage parameter, D, in the traction–separation law. When this parameter, that initially in the undamaged element is set to zero, reaches the limit value of one, the cohesive element has failed in that integration point. A penalty method is here used to ensure that the periodic boundary conditions are respected (see [20] for details). A detail of the mesh used in the finite element computations is shown in Fig. 1.

According to the the Roe-Siegmund model the traction separation law is given by:

$$\begin{aligned} T_n &= \sigma_{max,0} e \exp\Big(-\tfrac{\Delta u_n}{\delta_0}\Big)\Big\{\tfrac{\Delta u_n}{\delta_0}\exp\Big(-\tfrac{\Delta u_t^2}{\delta_0^2}\Big) + (1.0-q)\tfrac{\Delta u_n}{\delta_0}\Big[1.0-\exp\Big(-\tfrac{\Delta u_t^2}{\delta_0^2}\Big)\Big]\Big\} \\ T_t &= 2\sigma_{max,0} e q \tfrac{\Delta u_t}{\delta_0}\Big(1.0+\tfrac{\Delta u_n}{\delta_0}\Big)\exp\Big(-\tfrac{\Delta u_n}{\delta_0}\Big)\exp\Big(-\tfrac{\Delta u_t^2}{\delta_0^2}\Big) \end{aligned} \tag{1}$$

while the current cohesive strenghts are defined as

$$\begin{aligned} \sigma_{max} &= \sigma_{max,0}(1-D) \\ \tau_{max} &= \tau_{max,0}(1-D) \end{aligned} \tag{2}$$

The damage rate constitutive law is

$$\dot{D}_c = \frac{|\Delta\dot{\overline{u}}|}{\delta_\Sigma}\Big[\frac{\overline{T}}{\sigma_{max}} - C_f\Big]H(\Delta\overline{u} - \delta_0) \qquad \dot{D}_c \geq 0 \tag{3}$$

where $\overline{T}$ is the effective traction and $\Delta\overline{u}$ the accumulated separation (see [19]). A value of $\delta_\Sigma = 4\,\delta_0$ was choosen for this study. The parameter C_f represents the ratio between the cohesive endurance limit and the initial undamaged cohesive normal strenght:

$$C_f = \frac{\sigma_f}{\sigma_{max,0}}, \;\; C_f \in [0, 1] \tag{4}$$

Once an element has failed ($D = 1$), it still retains some strenght in compression, if $\Delta u_n < 0$, such that overlap is penalized

$$T_{n,compr} = \alpha\sigma_{max,0} e \exp\Big(-\frac{\Delta u_n}{\delta_0}\Big)\frac{\Delta u_n}{\delta_0} \quad , T_t = 0 \quad if \;\; \Delta u_n < 0, \;\; D = 1 \tag{5}$$

The penalty factor α was choosen to be $\alpha = 10$. No friction term was here introduced in the equations that describe the contact condition, see Eq.(5).

The periodic cell has a lenght of $l = 200\,\mu m$, while the radius of the inclusion is $R = 0.05\,l$, which is a typical value for Al_2O_3 in these steels [14]. Though the actual shape of the inclusion in the reality can be also different, e.g. ellipsoidal, it was here modelled as perfect circular.

The crack is assumed to have an initial lenght a_0 and to be inclined at an angle θ with respect to the rolling direction. One initial crack lenght, $a_0 \approx 1.5\,\mu m$ was considerd, while the angle θ that defines the angular position of the crack with respect to rolling direction is varied between 0° and 120°. The maximum allowed crack length is $a_0 \approx 2.97\,\mu m$: if the crack reaches this lenght, the computations are automatically stopped. Three different cases are considered, "CRC", "INT" and "POR". The first two assume an inclusion in the matrix, while the latter assumes a pore. The CRC case reflects the case of a crack in the matrix that is perfectly bonded to the inclusion. The two crack tips are here both in the matrix. The INT case models the case where the matrix–inclusion interface is flexible and therefore cohesive elements are used here along the interface, though they are not allowed to fail. The crack in this case has a crack tip in the matrix and a crack tip on the inclusion. The value of $E_i/E_m = 1.852$ has been used as ratio between the inclusion and the matrix Young's modulii, while the Poisson's ratio of the alumina, ν_i, is taken to be 0.25. The matrix has a Young's Modulus $E_m = 210\,GPa$ and a Poisson's ratio $\nu_m = 0.3$. The material behaviour in both the inclusion and the matrix is modelled as linear elastic.

3. Results

3.1. Test case

A test case with a cracked panel subjected to $R = \sigma_{min}/\sigma_{max} = 0$, $\sigma_{max} = 100\;MPa$ is first studied, in order to evaluate the Siegmund's model parameters δ_0, σ_{max0} and C_f. The parameter q was set equal to 0.429, so that the maximum normal and shear stresses are the same. Furthermore, the fatigue limit C_f was set equal to 0.005. This choice is justified on one hand by the need to reduce the set of parameters to be varied in the test case computations. Fixing the value of C_f in fact, δ_0 and σ_{max0} were the only two others parameters to be fitted. The value of C_f choosen, which appears small, is justified in the prospective of modeling the VHCF regime, where even small values of the stress imposed, below the conventional fatigue limit, may cause failure. Though these preliminaries computations were set to fall into the low cycle regime, this seemed the best choice. Furthermore is worth to notice that the test case was carried out assuming long–crack theory even though the subsequent case assumed cracks in the order of a micron.

A Paris law with $C = 11 \cdot 10^{-10}$ and $m = 4.05$ was fitted with the set of parameters $\delta_0 = 0.5\;\mu m$, $\sigma_{max0} = 21000\;MPa$ and $C_f = 0.005$, see Fig. 2. The resulting crack growth rate is in the order of $10^{-6}\;m/cycle$, with an initial $\Delta K_I \approx 5.63\;MPam^{0.5}$ ($DK_{th} = 5\;MPam^{0.5}$). This crack growth rate is at least 3 order of magnitude higher than what expected for this material for cracks in vacuum [21], but it was here chosen to have a qualitative understanding of the crack propagation under rolling contact, rather than trying to simulate the exact number of cycles to failure which is,

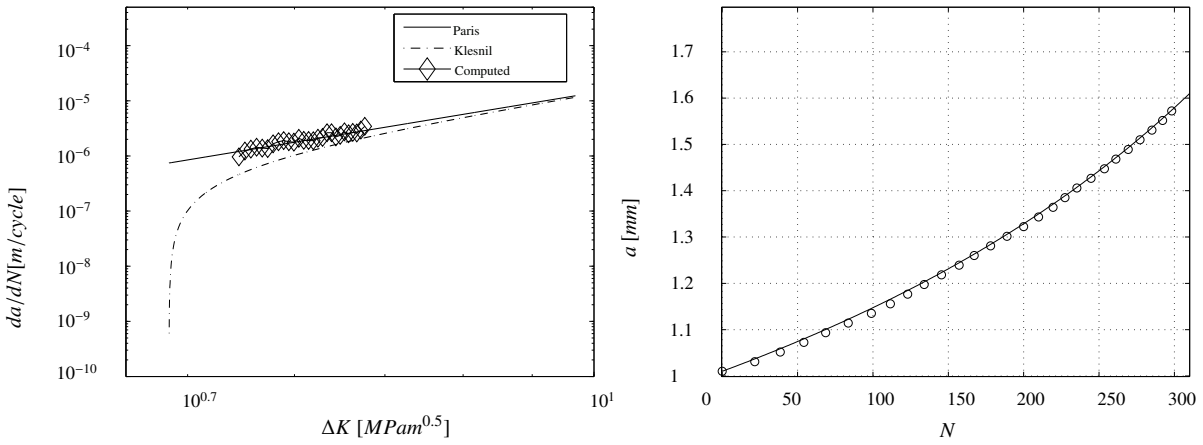

(a) (b)

Fig. 2: (a) Fatigue crack growth rate versus the stress intensity range for the test case and (b) corresponding crack lenght – cycles curve.

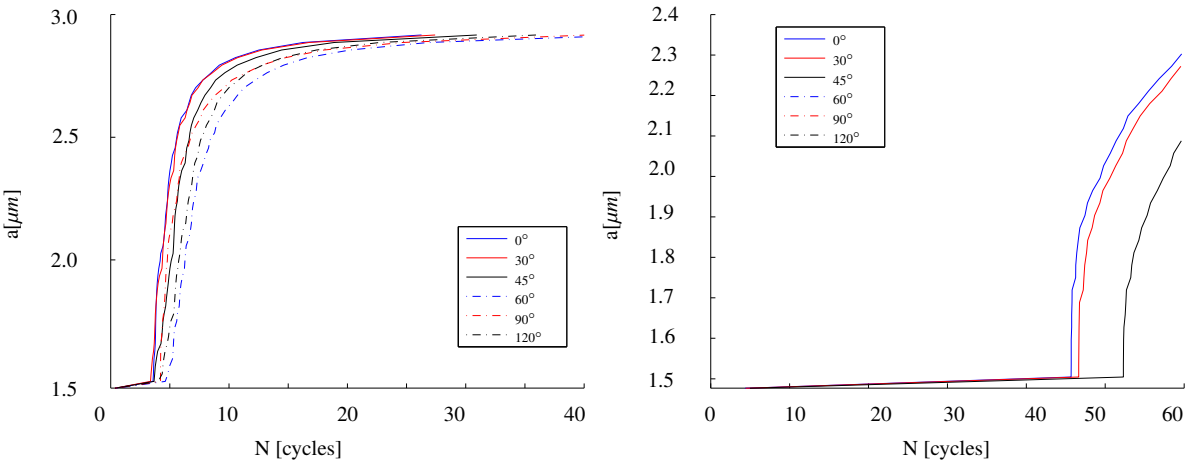

(a) (b)

Fig. 3: Crack lenght evolution for "CRC" case, assuming (a) $\delta_0 = 0.05\ \mu m$ and (b) $\delta_0 = 0.5\ \mu m$. In (b) only cracks with angles between 0° and 45° propagated within 60 cycles.

on the other hand, practically unfeasible in the giga cycle regime. The parameters for the cohesive law were thus used in the following calculations to study crack propagation in the inclusion–matrix unit cell.

3.2. Rolling contact results

Results in terms of crack lenght and number of cycles applied are shown in Figs. 3-4. From Fig. 3 ("CRC")is clear that a to a smaller value of $\delta_0 = 0.5\ \mu m$, i.e. a stiffer cohesive traction-separation law, corresponds a quicker propagation of the crack, regardless of the angle. The cracks with angles between 0° and 30° have the fastest propagation (Fig.3a), though differences with other angles are small. This seems to be confirmed also in Fig. 3b, where only angles smaller than 45° propagated within 60 cycles. Figures 4a-b, that refer to cases INT and POR, respectively, show the same trend related to the angle of the crack: the crack growth is slightly slower than the case CRC, and only the crack oriented at 90° seems to propagate considerably slower. All the results showed "S" shaped curves and further investigations are being carried out. The author believes that this may be due to the small size of the region where the cohesive elements are placed.

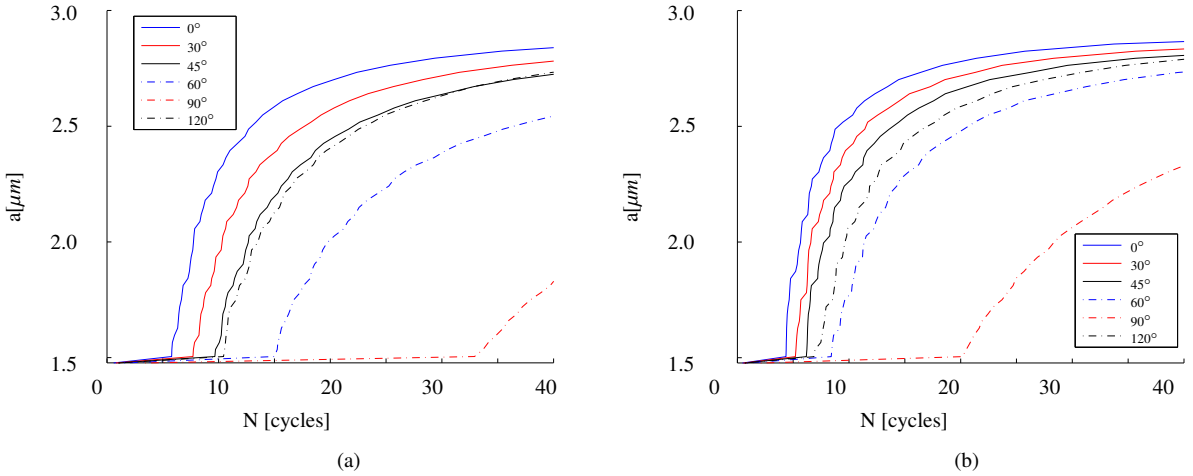

Fig. 4: Crack lenght evolution for (a) “INT” and (b) “POR” cases. $\delta_0 = 0.5\ \mu m$.

4. Conclusions

Fatigue crack growth under a typical rolling contact stress history has been investigated in this work, for different crack angles, for different inclusion-matrix conditions and for the case of a pore. Results show that crack angles between 0° and 45° propagate faster, but further investigations are suggested.

Acknowledgements

The work is supported by the Strategic Research Center ”REWIND - Knowledge based engineering for improved reliability of critical wind turbine components”, Danish Research Council for Strategic Research, grant no. 10-093966.

References

[1] Y. Murakami, T. Nomoto, T. Ueda. Factors influencing the mechanism of superlong fatigue failure in steels. Fatigue Fract. Eng. Mater Struc 22 (1999) 581–590.
[2] S. Nishijima, K. Kanazawa. Stepwise S–N curve and fish-eye failure in gigacycle fatigue. Fatigue Fract. Eng. Mater Struc 22 (1999) 601–607.
[3] K. Shiozawa, L. Lu, S. Ishihara. S–N characteristics and subsurface crack initiation behaviour in ultra-long life fatigue of a high carbon-chromium bearing steel. Fatigue Fract. Eng. Mater Struc 24 (2001) 781–790.
[4] K. Shiozawa, Y. Morii, S. Nishino, L. Lu. Subsurface crack initiation and propagation mechanism in high-strength steel in a very high cycle regime, Int. Journal of Fatigue 28 (2006) 1521–1532.
[5] T. Sakai, M. Takeda, K. Shiozawa et al.. Experimental evidence of duplex S–N characteristics in wide life region for high strength steels, in: Fatigue 99, Vol. I. (edited by X.R. Wu and Z.G. Wang). Higher Education Press, pp. 573–578.
[6] K. S. Chan. Roles of microstructure in fatigue crack initiation, Int. Journal of Fatigue 32 (2010) 1428–1447.
[7] M. -H. Evans, White structure flaking (WSF) in wind turbine gearbox bearings: effects of ’butterflies’ and white etching cracks (WEC). Journal of Materials Science and Technology 28 (2012) 3–22.
[8] M. -H. Evans, A. D. Richardson, L. Wang, R. J. K. Wood, Serial sectioning investigation of butterfly and white etching crack (WEC) formation in wind turbine gearbox bearings (2013) http://dx.doi.org/10.1016/j.wear.2012.12.031.
[9] A. Grabulov, R. Petrov, H. W. Zandbergen. ESBD investigation of the crack initiation and TEM/FIB analysis of the microstructural changes around the cracks formed under Rolling Contact Fatigue. International Journal of Fatigue 32 (2010) 576–583.
[10] T.A. Harris, M.N. Kotzalas. Rolling bearing analysis, Boca Raton (FL) CRC Press; 2007.
[11] K. Dang Van, G. Cailletaud, J.F. Flavenot et al..Criterion for high cycle fatigue failure under multiaxial loading, in: Biaxial and Multiaxial fatigue. Mechanical Engineering Publications, London: pp 459–478, 1989.
[12] S. Foletti, S. Beretta, M. G. Tarantino. Multiaxial fatigue criteria versus experiments for small crack under rolling contact fatigue, Int. Journal of Fatigue 58 (2014) 181–182.
[13] L. Hua, S. Deng, X. Han, S. Huang. Effect of material defects on crack initiation under rolling contact fatigue in a bearing ring, Tribology International 66 (2013) 315–323.

[14] Murakami Y. Metal Fatigue: Effects of Small defects and Nonmetallic Inclusions. Elsevier, Oxford, 2002 pp.5–8.
[15] Spinato F, Tavner PJ, van Bussel GJW, Koutoulakos E, Reliability of wind turbine subassemblies. IET Renew Power Gener 2009; vol 3 4: 387?401.
[16] Yang M, Chengbing H, Xinxin F. Institutions Function and Failure Statistic and Analysis of Wind Turbine. Physics Procedia 2012; 24:25?30.
[17] Ragheb A, Ragheb M. Wind turbine gearboxes technologies, Proceedings of the 1st International Nuclear and Reneawble Energy Conference, Amman, Jordan, 21-24 March 2010.
[18] M. Cerullo, Application of Dang Van criterion to rolling contact fatigue in wind turbine roller bearings under elastohydrodynamic lubrication conditions, P I Mech eng C-J Mec Prepublished December 20th 2013, DOI 10.1177/0954406213516946
[19] K. L. Roe, T. Siegmund. An irreversible cohesive zone model for interface fatigue crack growth simulation, Engineering fracture mechanics 70 (2003) 70:209–232.
[20] V. Tvergaard. Effect of stress-state and spacing on voids in a shear-field. International Journal of Solids and Structures, vol 49, no. 22, pp. 3047-3054.
[21] S. Stanzl-Tschegg, B. Schonbauer. Near-treshold fatigue crack propagation and internal cracks in steel, Procedia Engineering 2 (2010) 1547–1555.
[22] M. Cerullo, V. Tvergaard. Micromechanical study of the effect of inclusions on fatigue failure in a roller bearing. Paper sumbitted.

DTU Mechanical Engineering
Section of Solid Mechanics
Technical University of Denmark

Nils Koppels Allé, Bld. 404
DK- 2800 Kgs. Lyngby
Denmark
Phone (+45) 4525 4250
Fax (+45) 4593 1475
www.mek.dtu.dk
ISBN: 978-87-7475-390-2

DCAMM
Danish Center for Applied Mathematics and Mechanics

Nils Koppels Allé, Bld. 404
DK-2800 Kgs. Lyngby
Denmark
Phone (+45) 4525 4250
Fax (+45) 4593 1475
www.dcamm.dk
ISSN: 0903-1685